

Michael David John Cole

**Global gyrokinetic and fluid hybrid simulations of tokamaks and stellarators**

**IPP 12/14  
Juli, 2016**

# Global gyrokinetic and fluid hybrid simulations of tokamaks and stellarators

I n a u g u r a l d i s s e r t a t i o n

zur

Erlangung des akademischen Grades eines  
Doktors der Naturwissenschaften (Dr. rer. nat.)

der

Mathematisch-Naturwissenschaftlichen Fakultät

der

Ernst-Moritz-Arndt-Universität Greifswald

vorgelegt von

Michael David John Cole

geboren am 15.04.1990

in Bristol, Vereinigtes Königreich

Greifswald, 06.01.2016

Dekan: Prof. Dr. Werner Weitschies

1. Gutachter: Prof. Dr. Per Helander

2. Gutachter: Prof. Dr. Matthew Hole

Tag der Promotion: 15. Juni 2016

In loving memory of Professor George Herbert Avery Cole.

1928 - 2011



# Abstract

Achieving commercial production of electricity by magnetic confinement fusion requires improvements in energy and particle confinement. In order to better understand and optimise confinement, numerical simulations of plasma phenomena are useful. One particularly challenging regime is that in which long wavelength MHD phenomena interact with kinetic phenomena. In such a regime, global electromagnetic gyrokinetic simulations are necessary.

In this regime, computational requirements have been excessive for Eulerian methods, while Particle-in-Cell (PIC) methods have been particularly badly affected by the ‘cancellation problem’, a numerical problem resulting from the structure of the electromagnetic gyrokinetic equations. A number of researchers have been working on mitigating this problem with some significant successes.

Another alternative to mitigating the problem is to move to a hybrid system of fluid and gyrokinetic equations. At the expense of reducing the physical content of the numerical model, particularly electron kinetic physics, it is possible in this way to perform global electromagnetic PIC simulations retaining ion gyrokinetic effects but eliminating the cancellation problem.

The focus of this work has been the implementation of two such hybrid models into the gyrokinetic code EUTERPE. The two models treat electrons and the entire bulk plasma respectively as a fluid. Both models are additionally capable of considering the self-consistent interaction of an energetic ion species, described gyrokinetically, with the perturbed fields.

These two models have been successfully benchmarked in linear growth rate and frequency against other codes for a Toroidal Alfvén Eigenmode (TAE) case in both the linear and non-linear regimes. The  $m = 1$  internal kink mode, which is particularly challenging in terms of the fully gyrokinetic cancellation problem, has also been successfully benchmarked using the hybrid models with the MHD eigenvalue code CKA.

Non-linear simulations in this TAE case have been performed confirming the analytical prediction of a quadratic relationship between the linear growth rate of the TAE and the saturated amplitude of the TAE for a range of moderate values of the linear growth rate. At higher linear growth rate, a slower scaling of saturated amplitude with linear growth rate is observed. This analysis has been extended to include the non-linear wave-wave coupling between multiple TAE modes. It has been shown that wave-wave coupling results in a significant reduction in the saturated amplitude.

It has been demonstrated that both plasma elongation and ion kinetic effects can exert a stabilising influence on the internal kink mode. A population of energetic particles can also exert a stabilising influence at low normalised pressure. At high normalised fast particle pressure the stabilised kink mode has been shown to give way to the  $m = 1$  EPM, which has been simulated both linearly and non-linearly (the ‘fishbone’ mode).

The first self-consistent simulations of global modes in the magnetic geometry of the optimised stellarator Wendelstein 7-X have been performed both linearly and non-

linearly. Limitations have been encountered in performing simulations in 3D geometry. A hypothesis for the cause of these problems is outlined and ideas for mitigation are briefly described.

In addition to the hybrid model simulations, some of the first utilisations of a new scheme for mitigating the cancellation problem in the fully gyrokinetic regime have been carried out in the framework of this thesis. This scheme, which was developed separately, is concisely described in this work. The new scheme has been benchmarked with existing gyrokinetic and hybrid results.

The linear Wendelstein 7-X simulations and linear and single mode non-linear TAE simulations have been repeated with the new model. It is shown that bulk plasma kinetics can suppress the growth rate of global modes in Wendelstein 7-X. The results of fully gyrokinetic TAE simulations, the first to have been performed to our knowledge, are shown to be in close agreement with those results obtained using hybrid models.

In the TAE case, the hybrid models are an order of magnitude less computationally demanding than the new gyrokinetic scheme, which is in turn at least an order of magnitude less computationally demanding than the previous gyrokinetic scheme.

# Contents

<b>1</b>	<b>Introduction</b>	<b>1</b>
1.1	The energy problem . . . . .	1
1.2	Nuclear fusion . . . . .	2
1.2.1	Inertial confinement fusion . . . . .	3
1.2.2	Magnetic confinement fusion . . . . .	3
1.2.3	Toroidal devices . . . . .	5
1.2.4	Contemporary experiments . . . . .	6
1.3	Energetic particle physics . . . . .	8
1.3.1	Alfvén waves . . . . .	8
1.3.2	Principal drive and damping mechanisms . . . . .	9
1.3.3	Non-linear saturation mechanisms . . . . .	13
1.3.4	Fast particles in optimised stellarators . . . . .	14
1.4	Other global modes . . . . .	14
1.5	Review of numerical modelling efforts . . . . .	15
1.6	Status of EUTERPE . . . . .	17
1.7	The contribution of this thesis . . . . .	18
1.8	Outline . . . . .	19
<b>2</b>	<b>Model equations</b>	<b>21</b>
2.1	Gyrokinetics . . . . .	21
2.1.1	Kinetic system of equations . . . . .	23
2.1.2	Gyrokinetics by variational methods . . . . .	24
2.1.3	$v_{\parallel}$ formulation . . . . .	29
2.1.4	$p_{\parallel}$ formulation . . . . .	31
2.1.5	Mixed variables formulation . . . . .	31
2.2	Fluid and fluid-hybrid models . . . . .	33
2.2.1	Continuity equation from gyrokinetics . . . . .	33
2.2.2	Ideal Ohm's law and advective pressure closure . . . . .	35
2.2.3	Reduced MHD bulk plasma, gyrokinetic fast ion model . . . . .	36
2.2.4	Recovery of reduced ideal MHD . . . . .	36
2.2.5	Comparison with perturbative code CKA-EUTERPE . . . . .	37
2.2.6	Non-ideal closures . . . . .	38



<b>3</b>	<b>Numerical implementation</b>	<b>40</b>
3.1	EUTERPE code overview . . . . .	40
3.1.1	Gyrokinetic solver . . . . .	42
3.1.2	Distribution functions . . . . .	44
3.1.3	Gyrokinetic field equations . . . . .	44
3.2	Finite Larmor radius . . . . .	46
3.3	Coordinates . . . . .	47
3.4	Normalisation . . . . .	48
3.5	Fourier filtering . . . . .	49
3.6	Phase factor transformation . . . . .	49
3.7	Plasma equilibrium . . . . .	50
3.8	Cancellation problem and mitigation . . . . .	51
3.8.1	Adjustable control variate scheme . . . . .	53
3.8.2	Mixed variables scheme . . . . .	55
3.9	Hybrid models . . . . .	57
3.9.1	Numerical scheme . . . . .	58
3.10	Diagnostics . . . . .	60
<b>4</b>	<b>Linear simulations</b>	<b>62</b>
4.1	ITPA TAE benchmark . . . . .	63
4.2	Convergence studies and computational requirements . . . . .	67
4.3	TAE-continuum interaction . . . . .	70
4.4	TAE elongation study . . . . .	73
4.5	Internal kink mode . . . . .	75
4.5.1	In a screw pinch . . . . .	75
4.5.2	In a tokamak . . . . .	76
4.6	Linear m=1 EPM . . . . .	79
4.7	Global mode in Wendelstein 7-X . . . . .	81
4.7.1	Limits to stellarator simulations . . . . .	83
<b>5</b>	<b>Non-linear simulations</b>	<b>86</b>
5.1	Toroidal Alfvén Eigenmode . . . . .	87
5.1.1	Non-linear ITPA TAE benchmark case . . . . .	87
5.1.2	Non-linear wave-wave interaction . . . . .	95
5.2	Fishbone instability . . . . .	98
5.3	Non-linear stellarator . . . . .	100
<b>6</b>	<b>Conclusions</b>	<b>103</b>
6.1	Key results . . . . .	103
6.2	Outlook . . . . .	105

# Chapter 1

## Introduction

### 1.1 The energy problem

Energy must be expended to sustain and facilitate human life. Electrical energy is convenient because it can be cost efficiently transmitted over long distances and used in a variety of important processes. These include transduction to mechanical work, thermal heating, and visible light.

The principal disadvantage of electrical energy is that it cannot be stored at a cost efficiency, or weight or volume density, that is competitive with other forms. The superior storage characteristics of liquid hydrocarbon fuels in particular, such as oil and gas, has led to their widespread use as vehicle fuel.

The production of energy by burning hydrocarbon fuels also produces greenhouse gases. Emission of greenhouse gases has been predicted by numerical modelling to raise the average temperature of the earth [1]. The resultant temperature may be further from the optimal for human purposes than the current temperature. Even if it is not, any change implies some cost of adaptation. It is therefore desirable to substitute these fuels by fuels that do not produce greenhouse gasses.

Any such substitution implies costs, which must be weighed against the benefits in terms of reduced emissions. It is therefore important to minimise the cost of any such alternative. Currently there are three broad categories of such alternatives that have been pursued on an industrial scale.

- ‘Renewable’ energy sources produce electrical energy using radiation from the sun (solar PV, solar thermal, wind), energy from the earth’s core (geothermal), or from astronomical gravitational potential energy (tidal). The most cost effective such systems are solar thermal and wind, although the cost of PV has been dropping exponentially in recent years. Both ultimately take advantage of energy produced by nuclear fusion in the sun. Both however are intermittent, and therefore require storage on a scale much greater than has so far been attempted. The development and commercialisation of cost efficient, dense means of energy storage is an important area of active research.
- ‘Biofuels’ are synthetic hydrocarbons produced by natural processes using radiation from the sun. These directly substitute mined hydrocarbon fuels. Biofuels

can be regarded as a form of solar power that does not suffer from the intermittency problem. However, production is both land and manpower intensive and therefore costly.

- Nuclear fission produces electricity by accelerating energetically favourable nuclear reactions in naturally occurring ores. It does not require large scale energy storage and is both land and manpower efficient. However, it produces long lasting dangerous waste, the practicality of safe disposal of which remains a matter of discussion.

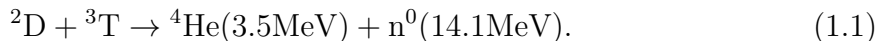
Nuclear fusion promises the possibility of an electricity source not limited by fuel, with no intrinsic carbon emissions, no additional storage requirements, and which does not produce waste that remains dangerous for longer than a single human lifetime. The building of a working reactor capable of net energy production, and the design of the most cost efficient possible commercial reactor, is an actively investigated open question in research, and the motivation for this work.

## 1.2 Nuclear fusion

Nuclear fusion is the process by which two atomic nuclei are combined to produce a new nucleus of greater atomic mass. We are particularly concerned with fusion reactions for which the products have a more negative binding energy than the fuels, releasing kinetic energy which may be used to produce electricity.

Although such reactions are energetically favourable, the Coulomb repulsion between electrically charged nuclei results in a high energy barrier which nuclei must first overcome. The probability of even the most favourable fusion reactions occurring at room temperature is so low that there is no known means of useful energy production in such conditions.

The fusion reaction with the largest reaction cross-section is Deuterium-Tritium process, the peak cross-section of which occurs with a fuel particle thermal energy of order 10 keV. At such temperatures, the Deuterium-Tritium fuel is a fully ionised plasma. The Deuterium-Tritium reaction is as follows,



The optimum temperature arises because the probability of two fuel particles colliding decreases with temperature while the probability of such a collision resulting in a successful fusion reaction increases. Quantum mechanical effects are important in calculating the reaction cross-section, which is significantly increased by tunnelling.

Heating particles to the high temperatures required for optimal fusion cross-sections immediately presents the problem of containing highly energetic particles within a reactor vessel of reasonable size. A number of possible solutions to this problem have been proposed. These are divided broadly into two categories, inertial confinement and magnetic confinement methods.

### 1.2.1 Inertial confinement fusion

The first example of a fusion reactor known to humans is the sun. The sun is an inertial confinement fusion device, in which high pressure in the core is produced by the strong gravitational forces resulting from its very large mass. However gravitational confinement fusion in the sun has an extremely low power density, on the order of  $1 \text{ W/m}^3$ , compared with order of  $100,000 \text{ W/m}^3$  for a gas turbine. Imitating the sun is therefore unlikely to be a fruitful approach.

Inertial confinement is also the method used to produce the first man-made fusion device and the first man-made fusion device with a net energy output. A thermonuclear bomb uses a chemical explosive to initiate a fission device which in turn compresses a small core of fusion fuel to sufficiently high pressure that significant fusion can occur. This fuel is usually Deuterium-Tritium but may also be Deuterium-Deuterium. It had been proposed that a pulsed commercial powerplant could be produced by detonating a series of thermonuclear bombs in a large cavern of water, but this is unlikely to be cost effective.

Alternatively, pulsed inertial confinement fusion is attempted by using lasers to compress a fuel pellet. To be viable, this method requires high efficiency lasers coupled with pellets that can be produced economically. Substantial effort and progress in this regard is taking place at research laboratories such as the National Ignition Facility (NIF) in the United States [2].

### 1.2.2 Magnetic confinement fusion

Since the inception of the field of fusion research for the purpose of electrical energy production, magnetic confinement devices have generally been considered the most promising. At the simplest level, magnetic confinement fusion devices employ magnetic fields, usually generated by electromagnetic field coils, such that outward motion of charged plasma particles is minimised.

In the presence of a magnetic field,  $\vec{B}$ , charged particles are free to move along the field lines. The speed at which they do so is called the parallel velocity,  $v_{\parallel} = \vec{b} \cdot \vec{v}$ , where  $\vec{b} = \vec{B}/B$  is the unit vector in the direction of the magnetic field and  $B$  is the magnitude of the magnetic field. In the direction perpendicular to the magnetic field,  $v_{\perp}$ , however, charged particle motion is opposed by the Lorentz force,

$$F = q\vec{v} \times \vec{B}, \quad (1.2)$$

where  $q$  is the particle charge [3].

Charged particles therefore stream along the field lines in a helical motion with a radius called the Larmor radius,  $\rho$ , given by the equation,

$$\rho = \frac{mv_{\perp}}{qB}, \quad (1.3)$$

where  $m$  is the particle mass.

Since the Lorentz force is perpendicular to the change in velocity of the charged particles, it does no work on the particles. The kinetic energy of the perpendicular

motion of the charged particles is therefore conserved in a constant magnetic field. It may therefore be useful to express this perpendicular motion in terms of a quantity called the magnetic moment,  $\mu = mv_{\perp}^2/2B$ . In terms of the magnetic moment, the Larmor radius is  $\rho = \frac{2\mu}{qv_{\perp}}$ .

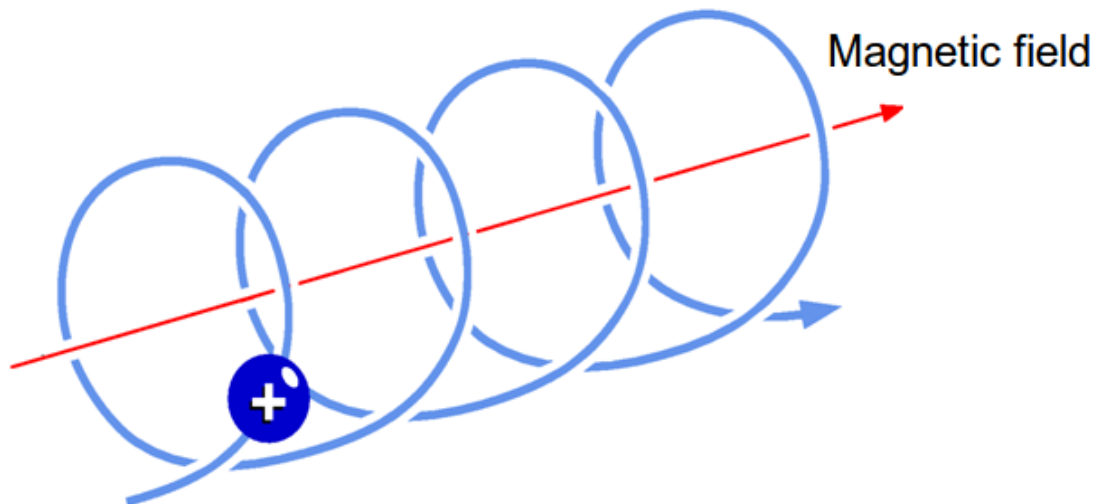


Figure 1.1: The motion of a single particle in a magnetised plasma: helical motion along the field lines.

The magnetic moment is adiabatically invariant, meaning that it is constant provided that variation in the magnetic field  $\vec{B}$  is insignificant within one gyroradius  $\rho$ , i.e.  $\rho/L_B \ll 1$ , where  $L_B$  is the characteristic length scale of magnetic field variation.

This property can be exploited to develop a simple magnetic confinement scheme for charged particles, the magnetic mirror. In the magnetic field a linear magnetic field with higher field strength at the extremities confines the plasma. Particles can stream freely within, but as the magnetic moment is conserved and the magnetic field does no work on the charged particles, the total kinetic energy of the particles must be constant,

$$\frac{d}{dt} \left( \frac{1}{2}mv_{\parallel}^2 + \frac{1}{2}mv_{\perp}^2 \right) = 0. \quad (1.4)$$

This equation requires that as the magnetic field strength increases the parallel velocity must decrease. Particles can therefore be reflected by sufficiently strong fields. In this way particles may be confined along as well as across field lines.

However, the mirror effect only confines particles within a certain range of ratio of parallel to perpendicular velocities, or pitch angles. Particles with pitch angles within the ‘loss cone’ are merely slowed and not reflected at the ends of the device. Since collisions will tend to equilibrate the plasma over time, these end losses lead to rapid loss of particles from the entire plasma.

One solution to this end loss problem is to adopt a toroidal geometry, such that particles can stream along the field lines indefinitely without being lost. So far, the most successful magnetic confinement devices use a toroidal magnetic geometry.

### 1.2.3 Toroidal devices

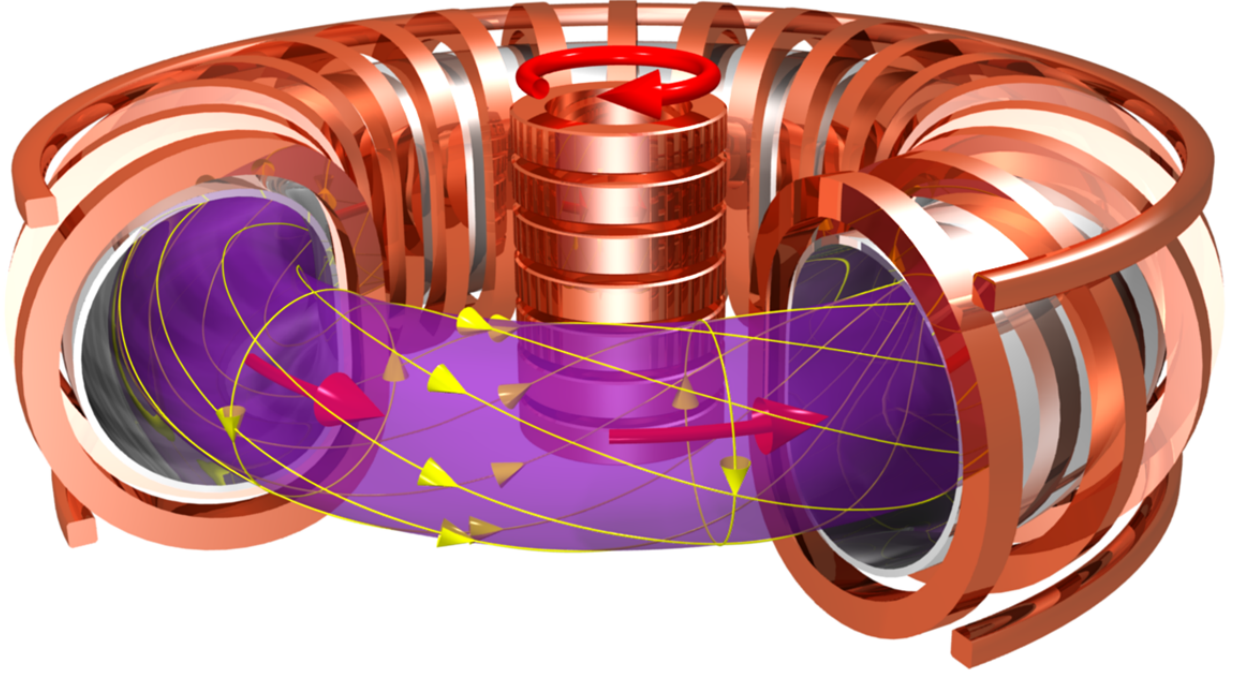


Figure 1.2: A schematic of a tokamak: a toroidal field generated by the toroidal field coils confines the plasma radially. A toroidal current is then induced within the plasma, generating a poloidal magnetic field which counteracts the  $\nabla B$  drift.

Although toroidal geometries eliminate end losses, they introduce a new inhomogeneity of the magnetic field because the magnetic field strength is higher on the inside of the torus than the outside. This results in a particle drift perpendicular to the magnetic field and the gradient of the inhomogeneity in the magnetic field strength, which also contributes to particle and energy transport,

$$\vec{v}_d = \frac{mv_{\perp}^2}{2qB} \frac{\vec{B} \times \nabla \vec{B}}{B^2} + \frac{mv_{\parallel}^2}{qB} \frac{\vec{B} \times \nabla_{\perp} \vec{B}}{B^2}, \quad (1.5)$$

where the second term is valid in the limit of small normalised plasma pressure,  $\beta$ ,

$$\beta = \frac{2\mu_0 P}{B^2} \ll 1. \quad (1.6)$$

Physically, one can picture the drift arising because the Larmor radius is smaller where the magnetic field strength is higher. The particle therefore moves further on the low  $B$  side of its orbit than on the high  $B$  side of its orbit.

As the direction of this drift is dependent on the particle charge, it results in a separation of ions and electrons. This charge separation generates an electric field, which in turn causes further ‘E cross B’ drift radially out of the plasma,

$$\vec{v}_E = \frac{\vec{E} \times \vec{B}}{B^2}. \quad (1.7)$$

Device	$n_e(10^{19}\text{m}^{-3})$	$T(\text{keV})$	$V(\text{m}^3)$	$B(\text{T})$	$J_{tor}(\text{MA})$	$Q$
ASDEX [4]	10	1	13	3.1	2	-
JET [5]	4	20	80	3.6	4	0.65
ITER [6]	10	8	830	5.3	15	10
EU-DEMO [7]	8	13	?	5.25	20	?
W7-AS [8]	10	1	1	2.5	$\sim 0$	-
LHD [9]	1	5	30	2.9	$\sim 0$	-
W7-X [10]	18	5	30	3	$\sim 0$	-
Helias [11, 12]	30	15	1570	5	$\sim 0$	$\infty$

Table 1.1: Typical key parameters for four current and future tokamaks and four current and future stellarators. As the plasma volume increases, extrapolated and predicted  $Q$  factors are sufficient for a demonstration electricity-producing reactor. Note that W7-X is yet to be operated with peak parameters and ITER, EU-DEMO, and Helias are yet to be built. The EU-DEMO and Helias designs have not been finalised. Optimised stellarators have some residual toroidal plasma current on the order of 10 kA.

The particle losses caused by this drift are significant, so it is necessary to counteract the  $v_d$  field inhomogeneity drift in order to prevent it occurring.

By applying a poloidal field, the magnetic field lines shift poloidally with each turn around the torus. This is characterised by the safety factor,  $q(r)$ , which is defined at each point in minor radius in terms of the ratio of the product of the major radius and the toroidal magnetic field strength to the product of the minor radius and the poloidal magnetic field strength,

$$q(r) = \frac{rB_t}{RB_p}. \quad (1.8)$$

As charged particles will follow the now helically twisted field lines, the radial position of those particles will oscillate. The  $\nabla B$  drift therefore averages to zero over time.

The means by which this safety factor profile is generated distinguishes the two leading toroidal magnetic confinement concepts, the tokamak and the stellarator. In a tokamak, this poloidal field is generated by running a current toroidally through the plasma. This approach, however, has drawbacks, such as the current's ability to drive MHD instabilities and the restriction of the device to pulsed operation. In a stellarator, this poloidal field is generated by the shaping of the magnetic field coils; the toroidal current can be minimised to prevent current-driven instabilities and permit inherently steady state operation, while retaining a safety factor profile.

### 1.2.4 Contemporary experiments

Since the first fusion experiments in the 1950s, newly constructed devices have been approaching more closely the parameters required for self-sustaining fusion that produces an excess of electrical power. One important quantity is the fusion energy gain

factor,  $Q$ . The  $Q$  value is the ratio of power produced to external heating,

$$Q = \frac{P_{fus}}{P_{heat}} = \frac{P_{fus}}{P_I + P_{NBI} + P_{RF}}, \quad (1.9)$$

where the quantities in the denominator account for the various heating methods.  $P_I$  is the Ohmic heating, i.e. heating due to resistive dissipation of the toroidal plasma current.  $P_{NBI}$  is heating due to the injection of neutral particles, which become ionised in the plasma.  $P_{RF}$  is the radio frequency heating.

In steady state operation, heating due to fusion and external heating must equal the heat flux out of the device. In order to produce useful power, the fusion power output must be at least equal to the external heating power, i.e.  $Q > 1$ . In practice, a somewhat higher  $Q$  value is needed to account for the inefficiency of conversion of fusion power to electricity, and of recirculation of this power to the heating systems.

If the plasma is fully self-heating, we no longer require external heating. In this case, the denominator drops to zero and  $Q = \infty$ . The device is then said to have reached ignition. To maximise  $Q$ , we require a large  $P_f$  and a low rate of loss of energy from the device. The rate at which energy leaves the device can be parameterised by a characteristic time scale,  $\tau_E$ , known as the energy confinement time.

In table 1.1, we compare parameters for the current and projected large fusion experiments. With current devices, plasma conditions have been achieved which correspond to those required for a net production of energy. In the JT-60U tokamak a shot has been performed, without tritium fuel, which from the measurements one can extrapolate 25% more power than was needed to heat the device would have been produced if tritium fuel had been present.

The confinement of heat within the device is therefore no longer a fundamental barrier to the demonstration of fusion energy, although improvements in confinement remain very important as they can lead to increased device efficiency and therefore reduced electricity cost. Further improvements in this respect will be important, and perhaps necessary, for commercialisation.

One fundamental problem is how to engineer a device to survive under high neutron bombardment over a long period of operation. Another is how to confine fast particles so that the alpha particles deposit their energy within the plasma volume, heating the plasma, and not on the walls, which could be damaged if too much energy is deposited in too small an area. In the next section we discuss this second issue in greater detail.

A third fundamental outstanding problem is how to prevent or mitigate Edge Localised Modes (ELMs) and disruptions, present in tokamaks. These current and pressure-driven instabilities have the potential to damage the device by causing large fluxes in areas of the first wall either directly or by the generation of runaway electrons. One promising approach to solving this problem is the stellarator, which produces a helical magnetic geometry without a toroidal current. In this case disruptions, as current-driven instabilities, are not present, and ELMs are substantially smaller. However, stellarator configurations pose greater problems than tokamaks for fast particle confinement, which will also be considered in this work.

A final issue is how the plasma can be made self-heating. In the Deuterium-Tritium reaction, 20% of the fusion power produced is contained in the kinetic energy of the



$\alpha$ -particles and 80% in the neutrons. Since the plasma is almost transparent to neutrons, the  $\alpha$ -particles must be contained in the plasma long enough to thermalise and deposit their energy by collisions.

Since the  $\alpha$ -particles have considerably higher average velocity than the background plasma, they exhibit different confinement properties, and it is not necessarily the case that a device that effectively contains D-T fuel will also effectively confine fusion  $\alpha$ -particles.

$\alpha$ -particle confinement also has other implications. The possibility of large numbers of alpha particles being deposited in a short time or in a small area on the first wall of a device also risks damaging the device.

This thesis will concern especially physics relevant to the control of energetic particles and instabilities that may influence energetic particle distribution.

## 1.3 Energetic particle physics

In this section, some more detailed physics relevant to energetic, or fast, particle behaviour in a magnetic confinement fusion device will be considered. A “fast” particle is one that is considerably more energetic than the thermal energy of the bulk plasma. In thermodynamic equilibrium, the bulk plasma will consist of particles with a Maxwellian distribution of energies. Since highly energetic particles will be produced by fusion reactions, and by heating systems such as NBI and RF heating, the distribution of particles in a certain range of energies higher than the thermal energy will diverge from a Maxwellian. It is this population with which fast particle physics concerns itself.

One topic of key interest is the interaction of fast particles with Alfvén waves, which exist in a frequency range such that they can interact resonantly. This can greatly amplify fast particle transport above that expected without considering the response of the thermal plasma to the fast particles. In a stellarator, there is the further complication that trapped particles are imperfectly confined even in a completely stable, collisionless plasma.

### 1.3.1 Alfvén waves

Alfvén waves are low frequency MHD waves, in which ions oscillate in response to the restoring force of magnetic tension. In this work, we will be particularly concerned with the shear Alfvén wave. The shear Alfvén wave is a low frequency transverse electromagnetic wave that propagates along the magnetic field. It has the dispersion relation,

$$\omega = v_A^2 k_{\parallel}^2, \quad (1.10)$$

where  $\omega$  is the wave frequency,  $k_{\parallel}$  is the parallel wavenumber, and

$$v_A = \frac{B}{\sqrt{\mu_0 m_i n}} \quad (1.11)$$

is the Alfvén velocity, with  $B$  the magnetic field strength,  $\mu_0$  is the permeability of free space,  $m_i$  is the ion mass and  $n$  is the plasma density [13]. This dispersion relation will be reproduced in the context of reduced ideal MHD later in this thesis.

In a toroidal device with a helical field, there is a restriction on the allowed parallel wave number,  $k_{\parallel}$ ,

$$k_{\parallel}(r) = \left( n - \frac{m}{q(r)} \right) / R, \quad (1.12)$$

where  $m$  and  $n$  are poloidal and toroidal mode numbers respectively and  $R$  is the major radius. This condition depends upon the location in minor radius because the helicity of the magnetic field changes in general, given by the safety factor profile.

Furthermore, the plasma density generally will tend to decrease between the magnetic axis and the edge. The Alfvén velocity will therefore increase. The magnetic field strength,  $B$ , can also be a function of radius.

Since both  $k_{\parallel}$  and  $v_A$  are functions of the minor radius, the mode frequency is also a function of the minor radius. The changing mode frequency across the device means that radially extended modes will become decorrelated. This is known as continuum damping, and generally means that Alfvénic modes are stable. Alfvén eigenmodes that are subject to continuum damping are known as ‘continuum modes’, and may give rise to unstable modes if subject to strong external drive.

By analogy to Bragg reflection in optical media, however, periodic modulations breaking a symmetry of the magnetic geometry create gaps in the continuous Alfvén spectra, in which radially extended modes can exist without being subject to continuum damping. In gaps created by toroidicity breaking the cylindrical symmetry of the system, these modes are called Toroidal Alfvén Eigenmodes (TAEs) [14, 15].

Toroidicity is not the only such periodic modulation, giving rise to gaps. In shaped tokamaks, gaps associated with ellipticity, reversed shear, and noncircularity can also house radially extended Alfvén eigenmodes. In stellarators, the Alfvén continuum is yet more complex, giving rise to gaps associated with e.g. helicity. Alfvénic physics in stellarators is thus far incompletely understood.

Continuum modes strongly driven by energetic particles are referred to as Energetic Particle Modes (EPMs). These typically occur when the energetic particle pressure is comparable to the bulk plasma pressure, and will also be considered in the course of this work.

### 1.3.2 Principal drive and damping mechanisms

Alfvén eigenmodes are generally stable in the absence of an energetic particle population. When a species of energetic particles is present, it is possible that they can resonate with the phase velocity of the shear Alfvén wave,  $v_{\parallel} \sim v_A$ . Energy can then be transferred from particles to the mode by a mechanism called Inverse Landau damping. In this way wave-particle resonant interaction can drive marginally stable modes unstable. These unstable modes in turn can cause redistribution of fast particles out of the device.

Landau damping (as inverse Landau damping) is a fundamentally kinetic process, due to the existence of gradients in the distribution function. In a simple illustrative picture it can be described as follows. Particles moving with the same velocity as the phase velocity of the wave (i.e.  $v_A$ ) experience the wave as stationary in their frame of reference. As such, they do not interact. Particles with slightly lower velocity than the

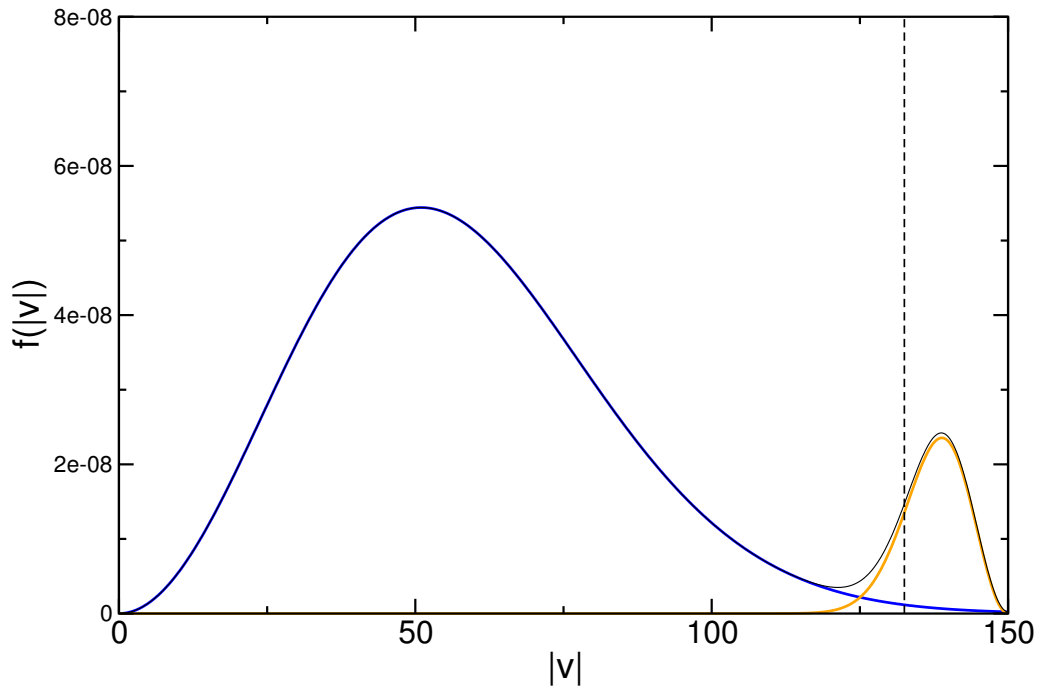


Figure 1.3: A sketch depicting inverse Landau damping due to a ‘bump on tail’ energetic particle population. A negative gradient in the velocity distribution of the thermal ions (blue) can coincide with a strong positive gradient in the velocity distribution of the energetic ions (orange) in the vicinity of a wave phase velocity indicated by the dashed black line.

wave are accelerated by the wave, damping it, while those with slightly higher velocity are slowed by the wave, driving it.

If there are more particles with a lower velocity than the phase velocity of the wave than particles with a higher velocity than the wave, the wave is damped on net by its interaction with the particles; this is often the case for a thermal plasma, hence the term Landau *damping*. Inverse Landau damping occurs when there is a positive gradient in the velocity of the particle distribution function. In a fluid treatment the distribution function is replaced by average macroscopic quantities, and Landau damping is therefore not present in the fluid description.

In figure 1.3, an illustrative ‘bump-on-tail’ distribution function is plotted in which a fast particle population provides a positive gradient in particle number around the resonant position. This is a particularly simple illustrative case in which inverse Landau damping would be present.

Energetic particle populations in fusion devices often have monotonically decreasing distribution functions in energy, however. Even in this case, however, waves can be driven by inverse Landau damping. Consider for instance the toroidal angular momentum, given by,

$$P_\varphi = mRv_\varphi - ZeRA_\varphi. \quad (1.13)$$

This function decreases with  $R$ , so  $\partial P_\varphi / \partial R < 0$ . For a monotonically decreasing distribution function in radius,  $\partial f / \partial R < 0$ , so that  $\partial f / \partial P_\varphi > 0$ . The wave can be

driven as the distribution function increases monotonically with  $P_\varphi$  [14].

In the absence of energetic particle drive, Alfvén eigenmodes are generally stable because of the damping effects of the bulk plasma. The principal damping mechanism is due to interaction with the continuum. Continuum damping is generally proportional to the gradients of the Alfvén velocity,

$$\gamma \sim - \left| \frac{dv_A}{dr} \right|, \quad (1.14)$$

that is, the damping is proportional to the rate at which the mode becomes decorrelated by the variation in the SAW’s rate of propagation across the minor radius. The presence of marginally stable global modes is principally due to the absence of continuum damping in so-called continuum gaps, where the gradient is locally zero.

Through the position of these gaps in the frequency spectrum, continuum damping places a strong limitation on the range of frequency of possible unstable modes and their peak radial positions. A mode that is centred inside the continuum at its mode frequency is unlikely to be unstable. Continuum damping can also act on gap modes, however, if the radial spread of the mode permits them to interact with the continuum far from the radial peak. Even in this case, continuum damping is generally greater than other forms of damping by the bulk plasma.

In figure 1.4, we depict residual continuum interaction with a gap mode. In this example continuum there is a gap below the minimum of the  $m = 2$  harmonic, which can house an AE that is not subject to continuum interaction. However, if the AE is sufficiently radially extended it can encounter the continuum and interact with it via the  $m = 1$  harmonic. The significance of this continuum damping depends on the structure of the mode and the strength of the coupling. Numerical tools treating such continua must be able to calculate the effect of such continuum interaction.

In addition to continuum damping, the presence of which depends upon the nature of the continuum and therefore the particular equilibrium under consideration, there are also bulk plasma dissipation mechanisms that are always present, although often not dominant. These include ion Landau damping, and electron collisional damping. These all depend on the properties of the thermal electrons and ions. Moreover other forms of damping may sometimes be present, depending on particular circumstances, such as radiative damping. The features of these additional forms of damping will now be briefly summarised.

The mechanism behind thermal ion Landau damping has already been hinted at. Since the thermal velocity of the bulk ions is much lower than the phase velocity of the Alfvén wave, a Maxwellian background plasma will have a negative gradient in its velocity around the resonance position, and therefore the wave will be subject to Landau damping.

However, the population of particles with sufficiently high velocity to resonate with the wave will be correspondingly very small. In the case of a TAE, significant thermal ion Landau damping is made possible by the modification of the resonance condition by the magnetic field curvature, which greatly increases the proportion of thermal particles that can interact. The resonance condition  $v_{\parallel} = v_A$  is supplemented by an additional resonance at  $v_{\parallel} = v_A/3$  [16, 17, 18].

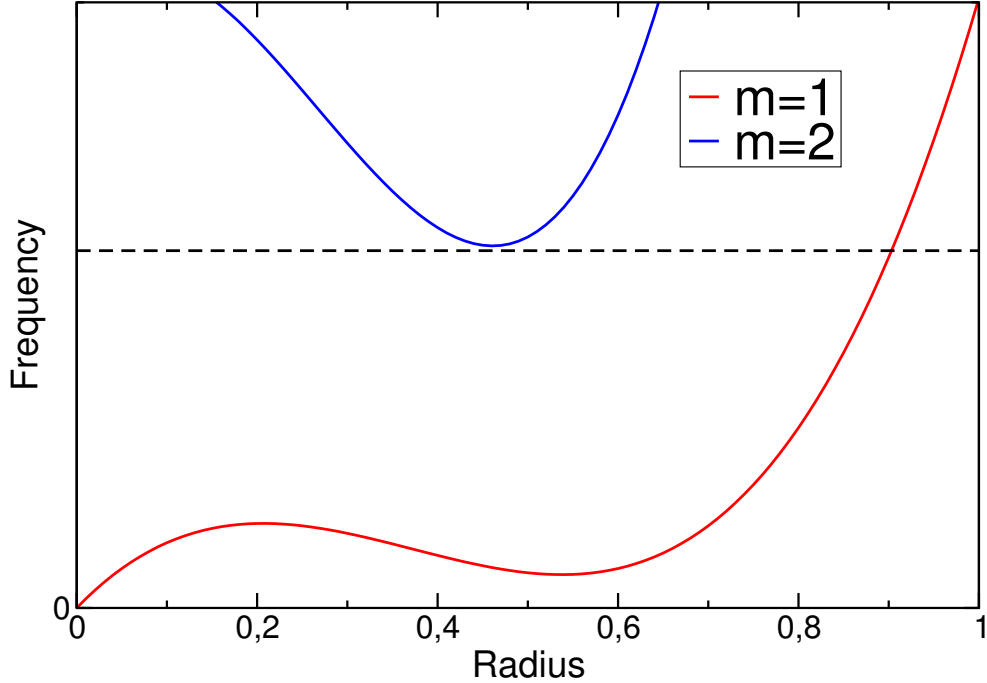


Figure 1.4: Sketch diagram of an artificial continuum, demonstrating peripheral continuum interaction. Continua are plotted for two poloidal harmonics. A gap mode can exist where the frequency gradient and thus continuum damping for the  $m = 2$  mode drops to zero, at radial position  $r = 0.45$ . If this mode is sufficiently radially extended, however, it can interact with the continuum via the  $m = 1$  harmonic near the edge.

Thermal ion Landau damping can be significant in a burning plasma. The strength of Landau damping and inverse Landau damping naturally depends upon the energy gradient in the particle distribution function. In projected demonstration reactors, the total fast particle pressure is expected to be comparable to the thermal plasma pressure, due to the much higher temperature of the relatively lower density fast particle population. In current experiments, the thermal plasma pressure is much higher than the fast particle pressure, such that thermal ion Landau damping is a relatively much stronger effect than it will be in a reactor.

Radiative damping occurs due to mode conversion from the TAE to a Kinetic Alfvén Wave through the effect of finite Larmor radius and resistivity [19]. Treating radiative damping therefore requires the consideration of kinetic and non-ideal effects, and, as the mode structure is modified, it requires a non-perturbative treatment, in which the mode structure can evolve over time.

Electron collisional damping is another mechanism predicted by analytical theory [20, 21]. The electron thermal velocity is larger than the ion thermal velocity by approximately the square root of the mass ratio, which is typically much larger than the Alfvén velocity. Resonant electrons are therefore deeply trapped, which may be expected to strongly suppress this route for damping. However, where the electron-ion collision frequency,  $\nu_{ei}$ , is comparable to the mode frequency, collisional damping

of trapped electrons can become significant. Numerically it has been problematic to consider electron collisional damping in detail due to the challenges of gyrokinetic simulation of electrons.

### 1.3.3 Non-linear saturation mechanisms

Eigenmode growth is determined by the linear physics. Such perturbations do not however typically come to dominate the equilibrium magnetic field structure. An important quantity of merit is the magnitude of the perturbation as a proportion of the equilibrium magnetic field,  $\epsilon_\Delta = \delta B/B_0$ . Non-linear terms are those which are second order or greater in the perturbed quantities. As the magnitude of the perturbation grows, non-linear terms can come to dominate the linear terms. Non-linear terms therefore control whether, and at what level, an eigenmode will saturate. Experimental  $\delta B/B_0$  inferred from plasma displacement in TFTR have been estimated at  $\mathcal{O}(10^{-3})$ . In this work we will therefore retain non-linear terms only to the lowest order.

There are two principal mechanisms for non-linear mode saturation. First, redistribution of fast particles may lead to local flattening of the profiles driving the mode. As inverse Landau damping drops to zero, the mode ceases to grow. Second, non-linear coupling of the unstable mode to other, stable modes may provide a sink for the mode to lose energy that would otherwise contribute to its growth [14].

In general predicting the quantitative behaviour of a system of coupled, non-linearly interacting modes driven and damped by common thermal and fast particle profiles, which are in turn affected by the collective behaviour of all the coupled modes, is beyond the scope of analytical theory and must be addressed numerically. Analytical models, such as the Berk-Breizman model [22, 23], are nonetheless very effective at predicting many of the qualitative features observed in experiment.

In the Berk-Breizman model a simple bump-on-tail fast particle population is posited driving a single mode, and parametrises the system's behaviour in terms of the linear growth rate of the mode,  $\gamma_L$ , the background damping rate,  $\gamma_d$ , the bounce frequency of resonant particles,  $\omega_b$ , and the collisionality of the system,  $\nu$  [24, 25, 26]. It predicts the formation of phase space holes and clumps, which are observed numerically [27], and frequency chirping which is observed experimentally [28, 29, 30, 31, 32].

Numerical simulation suggests that, with reactor-relevant parameters, bulk plasma non-linearity contributes to saturation and can reduce the saturation amplitude within an order of magnitude. These effects can be important in improving quantitative agreement with experimental measurements. The behaviour of the bulk plasma does not however determine the saturation [33].

Although numerical simulation is now able to accurately match experimental saturation levels given a parametrised damping level [33], it tends to underpredict transport of fast ions. Quantitative agreement with experiment can be reached assuming an order of magnitude higher  $\delta B/B_0$  than the observed [34, 35]. How to bridge the gap between numerical predictions and experimental observation remains an matter of on-going investigation.

### 1.3.4 Fast particles in optimised stellarators

Particles are not confined in general in a non-axisymmetric toroidal magnetic field, such as that of a stellarator, even in a collisionless regime without anomalous transport. In particular, there can be a finite radial drift of trapped particles between bounce points. In order to minimise trapped particle losses, the magnetic geometry can be optimised. For instance, the geometry can be optimised to minimise geodesic curvature of the field lines. In the limit of zero geodesic curvature, called an isodynamic plasma, trapped particle orbits do not drift radially out of the plasma [36].

A more practical choice of optimisation is quasi-isodynamicity. In a quasi-isodynamic configuration, trapped particles have non-zero drifts but these average to zero when integrated over time. Although a perfectly quasi-isodynamic configuration cannot be produced, a very close approximation can be achieved in practice.

Wendelstein 7-X is a quasi-isodynamic stellarator [37], and therefore should exhibit considerably lower fast particle transport than previous, unoptimised stellarators. However, because perfect quasi-isodynamicity cannot be achieved, the fast particle loss fraction is still expected to be greater than in a comparable tokamak device. This is of particular relevance to energetic particles, which have larger orbits than thermal particles and lower collisionality.

Toroidal Alfvén Eigenmodes are well known to exist in tokamak experiments [38]. They can also exist in stellarators and have been observed experimentally in the modular stellarator W7-AS [39, 40, 41] and the heliotron Large Helical Device (LHD) [42]. Such modes are anticipated to be present in the optimised stellarator Wendelstein 7-X, which began operation during the writing of this thesis, and in any reactor based on the quasi-isodynamic stellarator concept.

Furthermore, a wide array of other gap modes can exist in stellarators, including Global Alfvén Eigenmodes (GAEs) and Beta-induced Alfvén Eigenmodes (BAEs) which are also present in tokamaks, and Mirror-induced Alfvén Eigenmodes (MAEs) and Helical Alfvén Eigenmodes (HAEs) which are not.

## 1.4 Other global modes

Alfvén eigenmodes are some of the most practically important and theoretically interesting global modes known to exist in magnetic confinement fusion devices. Moreover, they are known to be present in both tokamaks and stellarators. They are not, however, the only global modes with relevance for fusion applications.

Other global modes may be driven by bulk plasma pressure gradients (e.g. interchange modes), bulk plasma current gradients (e.g. the internal kink mode), or energetic particles (e.g. the fishbone instability, which is closely related to the internal kink). Bulk plasma gradient-driven modes can usually be treated in a fluid model, but kinetic effects can modify stability limits. Energetic-particle driven non-Alfvénic global modes are typically driven by inverse Landau damping, like Alfvénic modes, and therefore require a kinetic treatment at least of energetic particles.

The internal kink mode is an ideal MHD mode which is driven by a bulk plasma current gradient. In a toroidal geometry, it also requires a bulk plasma pressure gra-

dient to be unstable. The instability is present at flux surfaces with integer  $q$ , and is generally greater at lower  $q$  surfaces. Since optimised stellarators can have negligible plasma current, they are typically designed such that internal kink modes are stable. In tokamaks, however, kink stability can limit the operational parameters of a device. In particular, where the plasma current is highest in the core  $q$  can be driven close to or below 1, giving rise to an internal kink instability or to related  $m = 1$  kink-like phenomena such as the Sawtooth cycle [43].

The sawtooth cycle is a generic tokamak phenomenon characterised by cyclical rises followed by sudden crashes in the core density and temperature. It is believed that drops in resistivity associated with rises in temperature increase the core plasma current such that the core plasma passes through, or close to, the  $q = 1$  internal kink stability boundary, which then redistributes plasma causing a sudden reduction in temperature and density. Kinetic effects can be of interest in kink physics within some parameter regimes. For instance, an energetic particle population has been shown to stabilise the Sawtooth cycle [44], which may be important in future large devices such as ITER. They are also responsible for driving fishbone modes in tokamaks, which have attracted some interest.

Ballooning modes are driven by bulk plasma pressure gradients. Since current-driven instabilities are often absent in stellarators, in these cases pressure-driven instabilities limit accessible operational regimes. In the Large Helical Device (LHD) stellarator in Japan, it has been observed that the plasma is stable at much higher core  $\beta$  values than predicted by ideal MHD theory [45]. This may be explicable by kinetic effects that could be captured by global 3D gyrokinetic simulations. Although ballooning modes may also be treated in the local limit, only a few local codes are capable of treating stellarator geometries.

## 1.5 Review of numerical modelling efforts

Analytical investigation has been able to identify many of the important drive and damping mechanisms, and device design considerations, discussed above. However, the analytical approach is generally not able to produce precise quantitative estimates of the relative strength of different drive and damping mechanisms, saturated perturbation levels, particle redistribution resulting from those perturbations, or fluxes of energy and particles resulting from these mechanisms. This is principally due to approximations that must be made in the magnetic geometry, choice of distribution function, and choice of mode numbers. In the case of optimised stellarators the difficulty is still greater, as the magnetic geometry is generally designed numerically and may be very complicated.

Generally more physically complete models are more limited in other respects as to the realism with which they can model fast particle physics. Such limitations include limitation to few or even a single mode, neglect of non-linearity, and restriction to simplified geometry. This is due to their greater computational expense, lower level of maturity, and/or unresolved numerical problems.

Highly detailed simulations have been performed with the gyrofluid code GYRO [46],



considering non-linearly the effects of turbulence interacting with TAEs in the local limit. These simulations in the flux-tube limit, however, do not take account of the effect of the global radial extent of TAEs, such as interaction with the continuum far from the resonant position, and neglect important non-linear effects such as the flattening of fast particle profiles. For this reason, most on-going work is performed using global codes.

Simulations closest to experiment have been performed with perturbative codes such as HAGIS, which couples a fixed MHD mode structure with a non-linear kinetic fast particle model [47, 48, 49]. Gyrokinetically, the code eigenvalue code LIGKA [50] is perhaps the most advanced, although its numerical approach limits it strictly to the linear regime. Current efforts seek to couple a mode structure calculated with LIGKA to the non-linear fast particle kinetic model of HAGIS, which may in due course become weakly non-perturbative by iteration of the LIGKA mode structure with updated profiles calculated by HAGIS.

Other perturbative codes include CKA-EUTERPE, CASTOR-K, NOVA-K, CAS3D-K, AE3D-K and VENUS [51, 52, 53, 54, 55, 56]. All of these codes couple a fixed mode structure calculated by MHD models of varying complexity and completeness with a gyrokinetic model for power transfer from fast particles. All have been used to investigate fast particle physics.

Non-perturbative hybrid codes include HMGC, MEGA and M3D [57, 58, 59]. These codes solve the same equations as those above, except that the perturbed mode structure responds self-consistently to the fast particles. An intermediate model treats the electrons as a fluid, while both the bulk and fast ions are modelled gyrokinetically, an approach that has been used by the codes GEM and GTC [60, 61].

Fully gyrokinetic models include eigenvalue codes such as LIGKA, discussed previously, and the similar KIN2DEM [62]. Fully gyrokinetic initial value codes also exist, including the Particle-In-Cell (PIC) codes NEMORB [63, 64, 65], GYGLES [66, 67, 68], and EUTERPE [69, 70]. These three related codes treat respectively axisymmetric (NEMORB and GYGLES) and arbitrary 3D geometries (EUTERPE). EUTERPE is therefore particularly suited to investigating stellarator physics. These fully gyrokinetic initial value codes can perform fully non-linear simulations; so far non-linear simulations of the global tearing mode have been published [71]. In addition to the PIC codes, the Eulerian code GKW has also been successful in simulating the tearing mode in the linear regime [72], and on-going work is also considering this mode in the non-linear regime [73].

There are advantages to having a range of such models at one's disposal. Practically, it is advantageous to use the least expensive model capable of treating a particular problem. More complex models can be used for verification purposes. It is also of interest to compare a single case with varying physical mechanisms considered. In this way, causality can be demonstrated in a particular physical effect.

## 1.6 Status of EUTERPE

Much of the work of this thesis will concern the gyrokinetic code EUTERPE mentioned above. EUTERPE is in principle the most physically complete code currently existing for the investigation of the physics of global modes in magnetic confinement fusion devices, capable of treating the thermal plasma and energetic species fully gyrokinetically, with self-consistent interaction of all species, into the non-linear regime in arbitrary 3D geometry.

EUTERPE has already been used to address a number of physical problems. Published results unrelated to this thesis include simulation of the linear electrostatic and electromagnetic Ion Temperature Gradient (ITG) instability in stellarators Wendelstein 7-X and Large Helical Device (LHD) [74].

Collisional physics has also been treated by the addition of the pitch-angle collision operator [75]. The collisional version of EUTERPE has been used to investigate neoclassical transport in Wendelstein 7-X and the stellarator TJ-II [76]. In the latter case numerical predictions from theory have been directly compared with experimental measurements [77].

Global mode work includes a contribution to a benchmark of frequency and growth rate of a Toroidal Alfvén Eigenmode in the linear regime. It has been used for theoretical investigation of the tearing mode in the linear and non-linear regimes [78], in the course of which work it has been benchmarked with a gyrofluid code in the non-linear regime [79]. The similar code GYGLES has been used to treat the kinetic physics of the internal kink mode in a screw pinch [67] among others, including the Toroidal Alfvén Eigenmode and related Energetic Particle Modes, including continuum effects [66, 68].

In some regimes, however, fully gyrokinetic electromagnetic simulations of global modes remain challenging, owing to a particularly severe numerical issue called the cancellation problem. This problem will be discussed in greater detail in section 3.8. One motivation for the development of reduced models has been to avoid this cancellation problem, even at the expense of lesser physical completeness.

Contemporaneously, a method for substantially mitigating this cancellation problem has been developed by Mishchenko and coworkers [80, 81]. Published proof-of-principle cases of successful gyrokinetic simulations that were not previously practical include TAEs in the ‘MHD limit’ ( $k_{\perp}\rho_i \rightarrow 0$ ) in a tokamak, and the electromagnetic ITG in a stellarator. So far EUTERPE and GYGLES are only codes in which this method has been fully implemented. It is discussed in section 3.8.2.

One existing reduced model is CKA-EUTERPE [51], a perturbative hybrid code package similar to NOVA-K, CAS3D-K, AE3D-K and VENUS. In CKA-EUTERPE, the reduced ideal MHD eigenvalue code CKA produces a fixed mode structure which is then passed to EUTERPE to calculate the power transfer of another species, which may be energetic particles, or thermal electrons or ions.

Although this code package naturally sacrifices some physical content, it is very numerically robust and avoids the cancellation problem, and has been successfully used not only for benchmarks and proof-of-principle cases, but for the reproduction of experimental shots in Wendelstein 7-AS [51] and for physics predictions for Wendelstein 7-X and the proposed optimised stellarator reactor HELIAS, using realistic distribution

functions [82].

## 1.7 The contribution of this thesis

In this thesis there are three principal original contributions. First, self-consistent fluid-kinetic hybrid models for the gyrokinetic code EUTERPE have been implemented, where either the entire bulk plasma or the electrons are treated as a fluid, with other species treated gyrokinetically. The theoretical model and numerical implementation of these models, called FLU-EUTERPE, is described.

The code is shown to successfully reproduce the results of more complete and computationally demanding full gyrokinetic models in appropriate limits. It is shown that the model permits simulations in regimes previously inaccessible to gyrokinetic PIC codes, such as electromagnetic modes, like the internal kink, in the MHD ( $k_{\perp}\rho_i \rightarrow 0$ ) limit [83]. These cases are considered with and without gyrokinetic bulk ions. It is demonstrated that the bulk ion kinetic effects are sometimes qualitatively important in determining Alfvén mode structure and growth rate. It is further demonstrated that the fluid-electron hybrid model does not fully reproduce the full gyrokinetic results where electron kinetic effects are important or where the chosen fluid closures break down, for instance where there is a significant finite parallel electric field [84].

Second, self-consistent gyrokinetic global non-linear simulations of toroidal Alfvén eigenmodes have been performed using both the hybrid models and a fully gyrokinetic model. The hybrid model results lie in close agreement with those obtained using other similar codes. The fully gyrokinetic results qualitatively validate the hybrid results in this regime, although quantitative agreement is not obtained due to the absence of ad-hoc damping mechanisms in the gyrokinetic model. Fully nonlinear gyrokinetic global simulations of TAEs have not previously been published [85]. In considering the trend of saturated perturbed magnetic field amplitude versus linear growth rate, a quadratic relation predicted by analytical theory is observed within a certain range of values, transitioning to a linear relation at higher linear growth rate.

The hybrid model has additionally been used to examine gyrokinetic non-linear wave-wave interaction through the bulk ions in a moderately realistic tokamak case for the first time, and it has been shown that coupling between TAEs and coupling between TAEs and the zonal mode reduce the saturated amplitude of the field perturbation. Mode coupling is shown to be important in determining the physics of even a relatively simple system.

Finally, electromagnetic global modes have been simulated self-consistently and gyrokinetically for the first time in the magnetic geometry of the optimised stellarator Wendelstein 7-X [84], and a successful verification has been performed in the magnetic geometry of the heliotron LHD. A set of non-linear runs in the optimised stellarator geometry have been performed with varying linear growth rate, yielding results that are not inconsistent with previous numerical and analytic predictions in the very high saturated perturbation amplitude limit.

In combination, these results demonstrate that both the fluid hybrid and fully gyrokinetic models in the numerical tool EUTERPE can be used for physical inves-

tigations into the interaction of global modes with fast particles, with sufficient completeness that predictions of energy and particle transport should be possible. The importance of gyrokinetic effects in the modelling of bulk ions has also been demonstrated. The reduced models have limitations which have been partially mapped and justified.

## 1.8 Outline

This thesis describes the development and exploitation of a code that solves the gyrokinetic equation for one or more particle species in a magnetised plasma, sometimes in combination with other equations providing a fluid description of one or more species in that plasma.

In this, the first chapter, the topic, motivation and structure of the dissertation have been introduced. The practical justification for interest in magnetic confinement fusion has been outlined. The basic physics of the confinement of a plasma optimised for sustaining fusion have been described. More detail has been given of physics relevant to fast particle interaction with Alfvén eigenmodes, and fast particle behaviour in optimised stellarators.

In the second chapter, the model equations will be developed, resulting in a gyrokinetic system of equations from which reduced fluid equations will be derived. Both systems of equations will be solved by the numerical code EUTERPE. The three key formulations of the gyrokinetic equations used in this work will be derived and the differences between them described; all are in principle physically identical but have different properties for numerical implementation. The fluid model, and its assumptions and extensibility, will be discussed.

In the third chapter, the numerical implementation of these equations in the code EUTERPE will be described. The magnetic geometry will be discussed along with the numerical scheme used to solve the coupled systems of equations. Particular treatment will be given of the cancellation problem, which has motivated much of the recent theoretical development of the numerical structure of the code, including the inclusion of reduced hybrid models.

In the fourth and fifth chapters, results obtained using the EUTERPE gyrokinetic and fluid-hybrid numerical models will be presented along with physical interpretation. The main cases considered will be as follows: an idealised Toroidal Alfvén Eigenmode benchmark case, called the ITPA TAE case, designed to allow investigation of the basic physics underlying the TAE in a tokamak in a way that permits good comparison between various codes; cases in which the internal kink mode is unstable in both screw pinch and tokamak geometry; and finally a case in which a global mode is driven unstable by fast particles in realistic Wendelstein 7-X stellarator geometry.

In chapter four these cases will be considered linearly and in chapter five the cases will be considered again this time with non-linear physics included. In all cases non-linear physics will enter only the gyrokinetic equations. Non-linear physics can be further restricted to just the wave-particle non-linear interaction, which as discussed in section 1.3.3 is usually dominant. Using the fluid-electron hybrid model, bulk ion

non-linear interaction will additionally be considered.

In the sixth chapter the thesis is concluded, with an extended summary of key results and discussion of the current status of the code, followed by a brief exposition of planned future work.

# Chapter 2

## Model equations

We consider the non-relativistic dynamics of a fully ionised plasma in the presence of an electromagnetic field, described by  $N$  coupled Lorentz equations for  $N$  particles,  $n$ :

$$m_n \frac{d\vec{v}_n}{dt} = q_n \left( -\nabla\phi(\vec{r}) + \vec{v} \times \left( \nabla \times \vec{A}(\vec{r}) \right) \right) \quad (2.1)$$

where  $m_n$  is the particle mass,  $\vec{v}_n$  is the particle velocity,  $q_n$  is the particle charge, and  $\phi$  and  $\vec{A}$  are respectively the electrostatic and magnetic potentials, given by the equations,

$$\phi(\vec{r}) = \frac{1}{4\pi\epsilon_0} \sum_n \frac{q_n}{|\vec{r} - \vec{r}_n|} \quad (2.2)$$

and

$$\vec{A}(\vec{r}) = \frac{\mu_0}{4\pi} \sum_n \frac{q_n v_n}{|\vec{r} - \vec{r}_n|}. \quad (2.3)$$

Since  $N$  in a viable fusion device will be greater than  $1 \times 10^{22}$ , this system of equations is intractable in practice. It is therefore necessary to solve reduced systems of equations. In this work, two approaches will be used. The first and most complete is the gyrokinetic approach, in which the microscopic behaviour of individual particles is considered statistically, with appropriate asymptotic expansion taken to isolate the most relevant timescale. In the second, the fluid approach, the plasma is described by averaged macroscopic parameters. Since the fluid picture is a limiting case of the (gyro)kinetic picture, the fluid equations will be derived from the gyrokinetic equations.

### 2.1 Gyrokinetics

The gyrokinetic description of a plasma is an asymptotic case of the kinetic description. In the kinetic description, a distribution function is posited,  $f(\vec{x}, \vec{v}, t)$ , describing the expected number of particles occupying any given position  $\vec{x}$  and velocity  $\vec{v}$  at time  $t$ . It follows, then, that integrating over all velocity space gives the particle density at a given position,

$$\int f(\vec{x}, \vec{v}, t) d^3v = n(\vec{x}, t), \quad (2.4)$$

where  $n$  is the physical density, while integrating over all position and velocity space gives the total number of particles in the system,  $N$ ,

$$\int f(\vec{x}, \vec{v}, t) d^3x d^3v = N. \quad (2.5)$$

In order to obtain an equation for the distribution function,  $f(\vec{x}, \vec{v}, t)$ , we need to impose some constraint on the system determined by the physics. In this case, the distribution function must obey a continuity equation, as in non-relativistic dynamics the particle number within phase space must be conserved.

The most general such equation neglecting correlations is the Maxwell-Boltzmann equation,

$$\frac{\partial f}{\partial t} + \dot{\vec{R}} \cdot \nabla f + \frac{q_s}{m_s} (-\nabla\phi + \vec{v} \times \nabla \times \vec{A}) \cdot \frac{\partial f}{\partial \vec{v}} = C(f(\vec{x}, \vec{v}, t)) + S(\vec{x}, \vec{v}, t) \quad (2.6)$$

where  $S$  is a source term and  $C$  is a collision operator. In this work, sources and sinks will be neglected. In the gyrokinetic description, collisions will also be neglected. The assumption of a collisionless plasma is justified in a high temperature fully ionised plasma, such as in the core of a magnetic confinement fusion device, as the collision cross-section scales with temperature as  $\nu \sim T^{-3/2}$ . A simple model for resistivity, which may model collisional effects, will be considered in the fluid description. This will be considered as an ad-hoc contribution and not be derived from the gyrokinetic equations.

With the source and sink terms set to zero, we obtain the Vlasov kinetic equation, which is the foundation of our derivation,

$$\frac{\partial f}{\partial t} + \dot{\vec{R}} \cdot \nabla f + \frac{q_s}{m_s} (-\nabla\phi + \vec{v} \times \nabla \times \vec{A}) \cdot \frac{\partial f}{\partial \vec{v}} = 0. \quad (2.7)$$

The Vlasov kinetic equation must be solved for the distribution function in six phase space coordinates (three space and three velocity) and time. Since it is often not necessary to resolve plasma behaviour on timescales shorter than the gyrofrequency, however, the equation can be simplified by decoupling the gyromotion, moving to a coordinate system in which the gyroangle is constant given some asymptotic expansion. This is the essence of gyrokinetics.

Mathematically, then, we can say that gyrokinetics is valid in the parameter regime,

$$\frac{\omega}{\Omega_c} \sim \epsilon_\omega, \quad (2.8)$$

where  $\omega$  is the characteristic frequency of the physical phenomenon of interest,  $\Omega_c$  is the gyrotron frequency, and  $\epsilon \ll 1$  is a small parameter. This ordering expresses that the phenomenon of interest takes place on a much longer time scale than the gyromotion.

It is also necessary that the characteristic scale length of the gradients is greater than the gyroradius; otherwise, the particle dynamics vary significantly within the course of its gyromotion, and it is no longer valid to consider the guiding centre motion separately to the gyromotion,

$$\frac{\rho}{L_{B,T,n}} \sim \epsilon_{B,T,n}, \quad (2.9)$$

where  $L_{B,T,n}$  are the background magnetic, temperature and density scale lengths. As a corollary, the fluctuating fields must have a small amplitude relative to the background fields, as otherwise the fluctuations could result in significantly differing dynamics over the course of a gyro-orbit,

$$\frac{e\delta\phi}{T} \sim \epsilon_\delta. \quad (2.10)$$

The gradients of the fluctuations may, however, be of the same order as the background gradients.

In the following section we will describe the derivation of the gyrokinetic equations that are solved in the course of this work. Traditionally, gyrokinetic equations have been derived by performing a perturbation expansion in a small parameter and averaging over the fast gyromotion [86].

Here, however, equations will be derived by performing a transformation from particle to gyrocentre phase space coordinates in which the motion of the gyrocentres does not depend upon the gyroangle. This procedure decouples the fast gyromotion from the slower reduced gyrocentre motion [87].

This approach has the advantage of producing equations that automatically conserve energy and momentum to the desired order. In this work, however, an additional significance is the ease with which the method can be used to derive systems of equations in coordinate systems which have very different numerical properties. These will be derived and detailed.

### 2.1.1 Kinetic system of equations

We start with the Vlasov equation in its general form,

$$\frac{\partial f}{\partial t} + \dot{Z}^i(\phi, A_{\parallel}) \frac{\partial f}{\partial Z^i} = 0, \quad (2.11)$$

where  $Z^i$  are general phase space co-ordinates.

Since the equations of motion,  $\dot{Z}^i(\phi, A_{\parallel})$ , depend in general upon the perturbed potentials, equations for these potentials are also necessary. The dynamics of electromagnetic potentials are determined by Maxwell's equations. For the perturbed magnetic potential, we take Ampère's law, neglecting the displacement current and the perpendicular component of the perturbed magnetic potential,  $A_{\perp}$ , which is always neglected in this work,

$$\nabla \times \vec{B} = \mu_0 \vec{J}, \quad (2.12)$$

which in terms of perturbed quantities is,

$$\mu_0 (J_{\parallel 1i} + J_{\parallel 1e}) = -\nabla_{\perp}^2 A_{\parallel}. \quad (2.13)$$

This equation relates the magnetic potential to the parallel current, which can be calculated from moments of the distribution function.

We work here in the Coulomb gauge, i.e.  $\nabla \cdot \vec{A} = 0$ . The approximation  $A \sim A_{\parallel}$  that has been made here is justifiable when considering modes, such as the Toroidal Alfvén eigenmode, and the kink mode, where the parallel length scale is much greater



than the perpendicular length scale,  $k_{\perp} \ll k_{\parallel}$ . Where  $\beta \sim \mathcal{O}(1)$ , however, the effect of compressional magnetic field perturbations must be taken into account. Such gyrokinetic equations have been derived, for instance in [87], but are not considered in this work. In the jargon of this thesis, systems in which this approximation  $A_{\parallel} \ll A_{\perp}$  is made are referred to as reduced systems. This applies to both the gyrokinetic and the fluid equations.

An equation is also needed for the perturbed electrostatic potential. In a quasi-neutral plasma, where we are concerned with length scales longer than the Debye length,

$$\lambda_D = \left( \epsilon k_b T / \sum_s n_{0s} e_s^2 \right)^{1/2}, \quad (2.14)$$

the total ion and electron densities are approximately the same,

$$n_{1i} - n_{1e} = 0, \quad (2.15)$$

which in the gyrocentre coordinates will give rise to a contribution in terms of  $\phi$  due to the gyrokinetic polarisation density. This choice of equation is equivalent to assuming that the contribution to the perturbed electrostatic potential due to the finite Debye length is small relative to the contribution due to the polarisation density, which is generally satisfied for plasmas in magnetic confinement fusion devices.

In the above equations the densities and currents are physical quantities, defined as moments of the distribution function. The density moment is,

$$n_s = \int f_s(\vec{x}, \vec{v}) d^3v \quad (2.16)$$

where  $n_0$  is the total density, and the parallel current moment is,

$$j_{\parallel s} = q_s \int v_{\parallel} f_s(\vec{x}, \vec{v}) d^3v. \quad (2.17)$$

Here  $f(\vec{x}, \vec{v})$  is the physical distribution function. Its form however changes depending on specific coordinate system chosen; care must therefore be taken to convert these equations into whatever final coordinate system is chosen for the Vlasov equation.

### 2.1.2 Gyrokinetics by variational methods

Having established the system of kinetic equations to be solved, we now proceed to gyrokinetics. The goal is to derive the Vlasov-Maxwell equations such that the fast gyromotion is decoupled from the dynamics occurring on the slower timescale of the background field fluctuations. The method is to arrive at a Lagrangian for a charged particle in fluctuating electromagnetic fields, such that the magnetic moment is a constant of the motion,  $\dot{\mu} = 0$ . This corresponds to no dependence of the dynamics on the gyroangle in our chosen coordinate system. From this Lagrangian, gyrokinetic equations of motion and gyrokinetic Ampère's law and Poisson equation (quasi-neutrality) can then be derived [87].

To do so we will begin with the Lagrangian for a charged particle in a static, or background, electromagnetic field. By Lie transformation methods [88], we can shift this Lagrangian into a coordinate system where the magnetic moment is constant, introducing the first gyrokinetic ordering parameter  $\epsilon_B$ . This is called the guiding centre coordinate system. From this could be derived the gyrokinetic Vlasov-Maxwell equations for test particles subject to prescribed static fields, but we are interested in phenomena that depend upon electromagnetic field fluctuations.

The coordinate transformation is defined as follows,

$$F(Z) = T\bar{F}(Z) = \bar{F}(TZ) = \bar{F}(\bar{Z}), \quad Z^n = (\vec{R}, v_{\parallel}, \mu, \theta), \quad \bar{Z}^n = (\vec{R}, \bar{v}_{\parallel}, \bar{\mu}, \bar{\theta}), \quad (2.18)$$

where  $Z$  and  $F$  are the initial coordinate system and scalar field respectively, and  $\bar{Z}$  and  $\bar{F}$  the transformed coordinate system and scalar field.

When field fluctuations are added to the guiding centre Lagrangian, however, the condition  $\dot{\mu} = 0$  is broken. To recover it, a second coordinate transformation is required based on the second gyrokinetic ordering parameter,  $\epsilon_{\delta}$ , to bring the Lagrangian into a coordinate system such that the magnetic moment is once again constant. This, final, system is called the gyrocentre coordinate system.

Together, this shift from particle to guiding centre (gc) coordinates and then to gyrocentre (gy) coordinations is called the ‘two-step derivation’. It is now an established method that has been detailed for non-linear gyrokinetics including parallel magnetic field perturbations in a recent review paper [87]. Here a brief description of the method and derivation in the appropriate limits for our code will be presented.

We start, then, with a Lagrangian for a charged particle in the presence of static electric and magnetic fields. This unperturbed extended Lagrangian,  $\hat{\Gamma}$ , is as follows,

$$\hat{\Gamma} = \left( \frac{e}{c} \vec{A}_0 + \vec{p} \right) \cdot d\vec{R} - w dt - \mathcal{H} d\tau \equiv \Gamma_i(Z) dZ^i - \mathcal{H} d\tau \quad (2.19)$$

where  $\Gamma_i$  is the symplectic one-form and  $\tau$  is the Hamiltonian orbit parameter.

The unperturbed extended phase space Hamiltonian,  $\mathcal{H}(Z)$ , is defined and related to the standard time-dependent Hamiltonian,  $H(\vec{R}, t)$ , as follows,

$$\mathcal{H}(Z) = \frac{|p|^2}{2m} + e\phi_0 - w \equiv H(\vec{R}, t) - w. \quad (2.20)$$

It can be shown [87] that the Euler-Lagrange equations can then be expressed in a form that gives the particle dynamics required to solve the kinetic Vlasov equation,

$$\frac{dZ^i}{d\tau} = J^{i\eta} \frac{\partial \mathcal{H}}{\partial Z^{\eta}} = \{Z^i, \mathcal{H}\}, \quad (2.21)$$

from which the standard relations for the evolution of the test particle position, velocity, and field energy could be derived in the full kinetic description. Since we are not concerned with kinetic test particle simulations in this work, these equations will not be written explicitly, and we will proceed to gyrokinetics in the presence of static background fields.

To do so, we perform a coordinate transformation of the type described in equation 2.18 such that the unperturbed Lagrangian becomes,

$$\Gamma_{gc} = \frac{e}{c\epsilon_B} \vec{A}_0^* \cdot d\vec{X} + \epsilon_B \mu \left( \frac{mc}{e} \right) d\theta - w dt, \quad (2.22)$$

and the Hamiltonian becomes,

$$\mathcal{H}_{gc} = \frac{p_{\parallel}^2}{2m} + \mu B_0 - w = H_{gc} - w, \quad (2.23)$$

where we have introduced the gyrokinetic ordering for the first time:  $\epsilon_B$  expresses the requirement that the variation of the background magnetic field,  $B_0 = \nabla \times \vec{A}_0$ , be small on the length scale of the gyroradius. Here the extended background magnetic potential is given by the equation,

$$\vec{A}_0^* \equiv \vec{A}_0 + \epsilon_B \left( \frac{c}{e} \right) p_{\parallel} \vec{b} + \mathcal{O}(\epsilon_B^2). \quad (2.24)$$

This coordinate system is called the guiding centre coordinate system; in the absence of electromagnetic field perturbations, it is equivalent to the gyrocentre coordinate system, in which the gyrotron timescale is decoupled from the timescale of the electromagnetic field fluctuations. For simplicity, the  $\epsilon_B$  terms will be dropped from now on.

Since we are interested in modes originating from the time-dependent fluctuation of the electromagnetic fields, we must consider an extended Lagrangian which includes perturbed electrostatic fields and, at least, perpendicular magnetic field perturbations. Introducing the notation for this new Lagrangian,

$$\Gamma_{gc} = \Gamma_{0gc} + \epsilon_{\delta} \Gamma_{1gc}, \quad (2.25)$$

and Hamiltonian,

$$\mathcal{H}_{gc} = \mathcal{H}_{0gc} + \epsilon_{\delta} \mathcal{H}_{1gc}, \quad (2.26)$$

we define the perturbed part of the Lagrangian as

$$\Gamma_{1gc} = \frac{e}{c} \vec{A}_{1\parallel}(\vec{X} + \vec{\rho}, t) \cdot d(\vec{X} + \vec{\rho}) \quad (2.27)$$

$$= \frac{e}{c} \vec{A}_{1\parallel gc}(\vec{X}, t; \mu, \zeta) \cdot d(\vec{X} + \vec{\rho}), \quad (2.28)$$

in the particle and guiding centre coordinates, for which the corresponding perturbed part of the Hamiltonian is,

$$H_{1gc} = e\phi_1(\vec{X} + \vec{\rho}, t) \quad (2.29)$$

$$= e\phi_{1gc}(\vec{X}, t; \mu, \zeta), \quad (2.30)$$

where we have introduced the perturbed guiding centre electrostatic and magnetic potentials,  $\phi_{1gc}$  and  $A_{1\parallel gc}$ , for the first time.

Note additionally that another ordering assumption has also entered for the first time:  $\epsilon_{\delta}$  expresses the requirement that the perturbation amplitudes be small relative to

the background fields. Both small parameter assumptions of gyrokinetics are therefore now present in our system of equations.

In this coordinate system, however, the magnetic moment is no longer a constant of the motion; the fast gyromotion is therefore no longer decoupled from drift motion on the slow timescale of the field fluctuations. A second coordinate transform of the Lagrangian is therefore required such that the contribution to the evolution of the magnetic moment due to the field fluctuations is also constant of the motion. This coordinate system will be called gyrocentre coordinates.

Performing the coordinate transform, we need to obtain the Hamiltonian from which we can derive the gyrokinetic equations of motion. The perturbed Lagrangian in the new system of coordinates is,

$$\bar{\Gamma} = \bar{\Gamma}_0 + \bar{\Gamma}_1 = \left[ \frac{e}{c} \left( \vec{A}_0 + \epsilon_\delta \vec{A}_{1\parallel gy} \right) + p_{\parallel} \vec{b}_0 \right] \cdot d\vec{X} + \frac{mc}{e} \bar{\mu} d\bar{\theta} - \bar{w} dt, \quad (2.31)$$

where the gyrocentre perturbed magnetic potential is,

$$\vec{A}_{1\parallel gy} = \alpha \left\langle \vec{A}_{1\parallel gc} \right\rangle \vec{b}. \quad (2.32)$$

Here  $\alpha$  is a Boolean parameter which represents our choice of transformed gyrocentre coordinate system. The gyroaverage is defined as,

$$\langle a \rangle = \int \frac{d\theta}{2\pi} a(\vec{R} + \vec{\rho}) \quad (2.33)$$

where  $a$  is a general function,  $\theta$  is the gyroangle,  $\vec{R}$  is the guiding centre position, and  $\rho$  is the gyroradius of the particle. Physically, the gyroaverage can be considered as an integral of  $z$  over the ring swept out by the gyromotion of the particle, normalised to circumference of the ring.

The corresponding Hamiltonian acquires terms at both the first and second orders in terms of  $\epsilon_\delta$ ,

$$\bar{H} = \bar{H}_0 + \epsilon_\delta \bar{H}_1 + \epsilon_\delta^2 \bar{H}_2, \quad (2.34)$$

where the first order Hamiltonian contribution is given by,

$$\bar{H}_1 \equiv e \langle \psi_{gc} \rangle = e \langle \phi_{gc} \rangle - \frac{ev_{\parallel}}{c} (1 - \alpha) \langle A_{1\parallel gc} \rangle, \quad (2.35)$$

and  $\psi_{gc}$  is the guiding centre perturbation potential.

The first order Hamiltonian is sufficient for a linear description. For a rigorously self-consistent non-linear description, or to derive the Ampère and Poisson equations by variation methods, the second order contribution to the Hamiltonian must also be considered [87]. Historically these non-linear terms have not been considered by EUTERPE or related codes, and the field equations have been derived by pullback transformation of the distribution function. In the future, however, it is planned to expand the code treatment to account for the non-linear corrections at second order. Their absence is not believed to qualitatively affect the results and will not be considered in this work. Current and future publications contain explicit equations with these contributions included [87].

The Jacobian is,

$$\mathcal{J} = m^2 B_{\parallel}^* \equiv m^2 \left( B_{0\parallel}^* + \epsilon_{\delta} \left( \alpha \left\langle \vec{A}_{1\parallel gc} \right\rangle \right) \right). \quad (2.36)$$

The parameter  $B_{\parallel}^*$  is given by,

$$B_{\parallel}^* = \vec{b} \cdot \vec{B}_{\parallel}^* \quad (2.37)$$

where

$$\vec{B}_{\parallel}^* = \vec{b}_0 \cdot \nabla \times \left( \vec{A}_0^* + \epsilon_{\delta} A_{1gy}^* \right). \quad (2.38)$$

It is clear, then, that there is more than one set of coordinates which satisfies the constraint  $\dot{\mu} = 0$ . Writing the equations of motion in the new gyrocentre coordinate system in terms of the Hamiltonian, it can be seen that there is an explicit dependence both on the term gyrocentre perturbed parallel magnetic potential  $A_{1\parallel gy}$  and the Hamiltonian  $\bar{H}$ , into which information on the choice of coordinate system is encoded,

$$\dot{\vec{X}} = \frac{c\vec{b}}{eB_{\parallel}} \times \left( \bar{\nabla} \bar{H} + \epsilon_{\delta} \frac{e}{c} \frac{\partial \vec{A}_{1\parallel gy}}{\partial t} \right) + \frac{\partial \bar{H}}{\partial \bar{v}_{\parallel}} \frac{\vec{B}^*}{B_{\parallel}^*}, \quad (2.39)$$

$$\dot{v}_{\parallel} = -\frac{\vec{B}^*}{B_{\parallel}^*} \cdot \left( \bar{\nabla} \bar{H} + \epsilon_{\delta} \frac{e}{c} \frac{\partial \vec{A}_{1\parallel gy}}{\partial t} \right), \quad (2.40)$$

From these expressions the equations of motion in each coordinate system can be calculated.

In this work, three sets of coordinates will be used. These are called the symplectic, or  $v_{\parallel}$ , coordinates, in which  $\alpha = 1$ ; the canonical momentum, or  $p_{\parallel}$  formulation, in which  $\alpha = 0$ ; and a third system, combining the properties of both, referred to as the mixed-variable coordinates, in which two components of  $A_{\parallel}$  are posited, one being treated in the manner of the symplectic formulation and the other in the manner of the canonical momentum formulation.

In terms of the Lagrangian,  $\alpha = 0$  corresponds to a time-independent symplectic part, with all fluctuating field quantities contained in the Hamiltonian part. Conversely  $\alpha = 1$  creates a time dependence in the symplectic part of the Lagrangian, but eliminates the so-called electron skin terms in Ampères law, which are numerically unfavourable for reasons that will be discussed in detail later. In the mixed variables formulation, part of the perturbed magnetic potential is considered in each part of the Lagrangian, meaning that the symplectic part is time-dependent in general but the magnitude of the time dependent terms can be controlled.

The definition of the gyrocentre parallel momentum also depends upon the choice of coordinate system, as follows,

$$\bar{p}_{\parallel} = p_{\parallel} + \epsilon_{\delta} \frac{e}{c} (A_{1\parallel gc} - \alpha A_{1\parallel gc}), \quad \bar{v}_{\parallel} = \frac{\bar{p}_{\parallel}}{m}. \quad (2.41)$$

From this equation it follows that in the symplectic formulation the gyrocentre parallel momentum is the same as the canonical momentum in the symplectic formulation

where  $\alpha = 1$ , and otherwise not. This is an especially important property as velocity moments of the distribution function are numerically more simple to implement.

In the following subsections the Vlasov-Maxwell equations will be presented in each of these coordinate systems. For more complete mathematical details on the derivation, see [87, 80, 81].

Maxwell's equations can also be derived directly by variational methods. In this work, however, we will derive the quasineutrality equation and Ampère's law by substituting the transformed distribution function equation into the moment equations for the two relations in particle coordinates. In particle coordinates, the gyrocentre distribution function is given by,

$$F = \bar{F} + \epsilon_\delta \{S_1, \bar{F}\} + \epsilon_\delta \frac{e}{c} A_{1\parallel gc} \vec{b} \cdot \{\vec{X} + \vec{\rho}, \bar{F}\}, \quad (2.42)$$

where  $S_1$  arises from the Lie transform from the guiding centre to the gyrocentre coordinate system, and is given by the expression,

$$S_1 = \frac{e}{\Omega_0} \tilde{\Psi}_{gc}. \quad (2.43)$$

This equation therefore also depends upon the choice of final gyrocentre coordinate system. The quantity  $\tilde{\Psi}_{gc} = \int^\theta \tilde{\psi}_{gc} d\theta$  is calculated using

$$\tilde{\psi}_{gc} = \psi_{gc} - \langle \psi_{gc} \rangle, \quad (2.44)$$

i.e. it represents the fluctuation in the gyrocentre perturbed potential after subtracting the gyroaveraged quantity.

Finally it is possible by similar methods to prove that this resulting system of equations satisfies the requirement of energy conservation. This will not be done here. Numerically energy conservation depends both upon the properties of the model equations and of the numerical scheme.

In this derivation the equations have been formulated in cgs units. In what follows, EUTERPE units will be used.

### 2.1.3 $v_{\parallel}$ formulation

The most natural choice of dynamical variables is to express the particle's position and parallel velocity,  $v_{\parallel}$ , in terms of the parallel velocity in particle coordinates. This is called the  $v_{\parallel}$ -formulation or symplectic formulation. In this case, we the coordinate selection parameter to be one,  $\alpha = 1$ .

In this formulation the equations of motion are as follows,

$$\vec{R} = v_{\parallel} \vec{b}^* + \frac{1}{q_s \tilde{B}_{\parallel}^*} \vec{b} \times \left[ \mu \nabla B + q_s \left( \nabla \langle \phi \rangle + \frac{\partial \langle A_{\parallel} \rangle}{\partial t} \vec{b} \right) \right], \quad (2.45)$$

$$\dot{v}_{\parallel} = -\frac{1}{m_s} \vec{b}^* \cdot \mu \nabla B - \frac{q_s}{m_s} \left( \vec{b}^* \cdot \nabla \langle \phi \rangle + \frac{\partial \langle A_{\parallel} \rangle}{\partial t} \right) \quad (2.46)$$

$$\dot{\mu} = 0, \quad \dot{\theta} = \omega_c, \quad (2.47)$$

where

$$\vec{B} = \vec{B} + \nabla \times A_{\parallel} \vec{b}. \quad (2.48)$$

In this formulation alone, the distribution function solved for is the physical distribution function, from which moments can be directly calculated following the equations in the previous section.

In the delta-f formalism, where  $f = F_0 + f_1$  with Maxwellian  $F_0$ , the quasi-neutrality equation and Ampère's law take the forms,

$$n_{1i} - n_{1e} = -\frac{en_0}{T_i} (\langle \bar{\phi} \rangle_i - \phi) - \frac{en_0}{T_e} (\langle \bar{\phi} \rangle_e - \phi) \quad (2.49)$$

and

$$\mu_0 (j_{\parallel 1i} + j_{\parallel 1e}) = -\nabla_{\perp}^2 A_{\parallel}. \quad (2.50)$$

The barred quantities are given by the equations,

$$\langle \bar{\phi} \rangle = \frac{1}{n_0} \int \mathcal{J} d^6 Z F_{0s} \langle \phi \rangle \delta(\vec{R} + \vec{\rho} - \vec{x}) \quad (2.51)$$

and

$$\langle \bar{A}_{\parallel} \rangle = \frac{1}{n_0} \int \mathcal{J} d^6 Z F_{0s} \langle A_{\parallel} \rangle \delta(\vec{R} + \vec{\rho} - \vec{x}) \quad (2.52)$$

with  $F_{0s}$  taken to be Maxwellian and where  $d^6 Z = d\vec{R} dv_{\parallel} d\mu d\theta$ .

Note that here the equations of motion contain perturbed quantities, such that the Vlasov equation in terms of  $f = F_0 + f_1$  is non-linear. The equation can also be linearised, yielding,

$$\frac{\partial f_1}{\partial t} + \dot{\vec{R}}^{(0)} \cdot \frac{\partial f_1}{\partial \vec{R}} + v_{\parallel}^{(0)} \frac{\partial f_1}{\partial v_{\parallel}} = -\dot{\vec{R}}^{(1)} \cdot \frac{\partial F_0}{\partial \vec{R}} - v_{\parallel}^{(1)} \frac{\partial F_0}{\partial v_{\parallel}} \quad (2.53)$$

where  $\dot{\vec{Z}}^{(1)}$  signifies the full equation of motion, while  $\dot{\vec{Z}}^{(0)}$  signifies the equation of motion neglecting perturbed quantities, in terms of  $A_{\parallel}$  and  $\phi$ .

The new terms on the right hand side of the quasi-neutrality equation correspond to the gyrokinetic polarisation density. This full quasi-neutrality equation above is, however, not solved numerically in this work. Instead, either the long-wavelength approximation,

$$-\nabla_{\perp} \cdot \left( \frac{en_0}{T_i} \rho_i^2 \nabla_{\perp} \phi \right) = n_i - n_e, \quad (2.54)$$

or the Padé approximation,

$$(1 - \rho_i^2 \nabla_{\perp}^2)(n_i - n_e) = -\nabla_{\perp} \cdot \left( \frac{en_0}{T_i} \rho_i^2 \nabla_{\perp} \phi \right) \quad (2.55)$$

is employed. The long-wavelength approximation expands the ion gyroaverage in Fourier space to order  $(k_{\perp} \rho_i)^2$ , and neglects finite Larmor radius effects for electrons. This is a valid approximation for  $k_{\perp} \rho < 1$ . The Padé approximation extends the

range of validity of the approximated quasi-neutrality equation and is generally to be preferred.

This formulation is advantageous because the distribution function is automatically in the correct form to be used to calculate physically meaningful moments such as the perturbed density and velocity in terms of particle coordinates.

### 2.1.4 $p_{\parallel}$ formulation

In the  $p_{\parallel}$ -formulation, or canonical momentum or Hamiltonian formulation, we make the choice  $\alpha = 0$ . The equations of motion are as follows,

$$\dot{\vec{R}} = \left( v_{\parallel} - \frac{q}{m} \langle A_{\parallel} \rangle \right) \vec{b}^* + \frac{1}{qB_{\parallel}^*} \vec{b} \times (\mu \nabla B + q \nabla \langle \psi \rangle) \quad (2.56)$$

$$\dot{v}_{\parallel} = -\frac{1}{m} (\mu \nabla B + q \nabla \langle \psi \rangle) \cdot \vec{b}^* \quad (2.57)$$

$$\dot{\mu} = 0, \quad \dot{\theta} = \omega_c. \quad (2.58)$$

Note that the time derivative  $\partial A_{\parallel} / \partial t$  is no longer present here. The choice of variables affects the distribution function, such that moments of the distribution function taken where  $v_{\parallel}$  is not the physical  $v_{\parallel}$  do not necessarily correspond to the physical density, current, or pressure.

Using these moments, we can derive Ampère's law and the quasi-neutrality equation in terms of the symplectic coordinates. These are, respectively,

$$\sum_s \frac{\beta_s}{\rho_s^2} \langle \bar{A}_{\parallel} \rangle_s - \nabla_{\perp}^2 A_{\parallel} = \mu_0 \sum_s \bar{j}_{\parallel s} \quad (2.59)$$

and

$$\bar{n}_{1i} + \frac{en_0}{T_i} (\langle \bar{\phi} \rangle_i - \phi) = \bar{n}_{1e} - \frac{en_0}{T_e} (\langle \bar{\phi} \rangle_e - \phi). \quad (2.60)$$

The Ampères law equation now includes new terms, the skin terms, which are proportional to  $\beta_s / \rho_s^2$ . These skin terms are numerically complicating and in particular give rise to the electromagnetic gyrokinetic cancellation problem. This problem will be discussed in greater detail in section 3.8.

The quasi-neutrality equation in the Hamiltonian formulation given here is the same as that in the  $v_{\parallel}$  formulation. In fact, an additional term enters the magnetisation vector in the symplectic formulation that would not be present here [87]. However, in both formulations the magnetisation vector is neglected in this work. Approximated forms of the quasi-neutrality equation are the same as for the  $v_{\parallel}$ -formulation.

### 2.1.5 Mixed variables formulation

A 'mixed' formulation of the equations of motion will also be used, which combine the numerical properties of both systems of equations. The numerical advantages of this concept will be described in greater detail in section 3.8.2, in which the numerical implementation is discussed.



In the mixed-variables formulation, developed by Mishchenko and co-workers [80, 81], the  $p_{\parallel}$  and  $v_{\parallel}$  formulations are combined to yield the following equations of motion for the position and parallel velocity,

$$\dot{\vec{R}}^{(1)} = \frac{\vec{b}}{B_{\parallel}^*} \times \nabla \langle \phi - v_{\parallel} A_{\parallel}^{(s)} - v_{\parallel} A_{\parallel}^{(h)} \rangle - \frac{q}{m} \langle A_{\parallel}^{(h)} \rangle \vec{b}^* \quad (2.61)$$

$$\dot{v}_{\parallel}^{(1)} = -\frac{q}{m} \left[ \vec{b}^* \cdot \nabla \langle \phi - v_{\parallel} A_{\parallel}^{(h)} \rangle + \frac{\partial}{\partial t} \langle A_{\parallel}^{(s)} \rangle \right] - \frac{\mu}{m} \frac{\vec{b} \times \nabla B}{B_{\parallel}^*} \cdot \nabla \langle A_{\parallel}^{(s)} \rangle, \quad (2.62)$$

The derivation proceeds as before until, arriving at the perturbed guiding-centre phase-space Lagrangian,

$$\gamma = q \vec{A}^* \cdot d\vec{X} + \frac{m}{q} \mu d\theta + q A_{\parallel}^{(s)} \vec{b}_0 \cdot d\vec{x} + q A_{\parallel}^{(h)} \vec{b}_0 \cdot d\vec{X} - \left[ \frac{m v_{\parallel}^2}{2} + \mu B + q \phi \right] dt, \quad (2.63)$$

an arbitrary division of the magnetic potential is made into symplectic and Hamiltonian parts,

$$A_{\parallel} = A_{\parallel}^{(s)} + A_{\parallel}^{(h)}. \quad (2.64)$$

The subsequent coordinate transformation is performed such that  $A_{\parallel}^{(s)}$  enters the symplectic structure and  $A_{\parallel}^{(h)}$  enters the Hamiltonian, yielding the gyrocentre phase-space Lagrangian,

$$\Gamma = q \vec{A}^* \cdot d\vec{X} + \frac{m}{q} \mu d\theta + q \langle A_{\parallel}^{(s)} \rangle \cdot d\vec{X} - \left[ \frac{m v_{\parallel}^2}{2} + \mu B + q \langle \phi - v_{\parallel} A_{\parallel}^{(h)} \rangle \right] dt. \quad (2.65)$$

The perturbed distribution function is related to that in the symplectic formulation by the equation,

$$f_{1s}^m = f_{1s}^s - \frac{q_s \langle A_{\parallel}^{(h)} \rangle}{m_s} \frac{\partial F_{0s}}{\partial v_{\parallel}}, \quad (2.66)$$

which in turn allows us to derive the form of the gyrokinetic Ampère's law and quasineutrality equations. These are as follows,

$$\int \frac{q_i F_{0i}}{T_i} (\phi - \langle \phi \rangle) \delta(\vec{R} + \vec{\rho} - \vec{x}) d^6 Z = \bar{n}_{1i} - \bar{n}_{1e} \quad (2.67)$$

and

$$\left( \frac{\beta_i}{\rho_i^2} + \frac{\beta_e}{\rho_e^2} - \nabla_{\perp}^2 \right) A_{\parallel}^{(h)} - \nabla_{\perp}^2 A_{\parallel}^{(s)} = \mu_0 (\bar{J}_{\parallel 1i} + \bar{J}_{\parallel 1e}). \quad (2.68)$$

The pullback transformation to the symplectic distribution function is also necessary in order to calculate physical moments by integrating over the marker quantities, and will be important in the numerical scheme employed with the mixed variables formulation, discussed in greater detail in section 3.8.2.

Note that the Ampère’s law equation retains the collisionless skin terms of the canonical-momentum formulation, but now they are proportional only to the Hamiltonian component of the perturbed magnetic potential,  $A_{\parallel}^{(h)}$ , not to the total perturbed magnetic potential,  $A_{\parallel}$ . This is key to the numerical utility of the scheme and will be discussed in greater detail in Section 3.8.2. The quasi-neutrality equation is the same as in both the symplectic and canonical momentum formulations; this should not be surprising as it is a combination of both formulations.

## 2.2 Fluid and fluid-hybrid models

In the previous section, macroscopic quantities have already been introduced in the context of the quasi-neutrality equation and Ampère’s law for a gyrokinetic system of questions. In this framework, the gyrokinetic Vlasov equation is first solved to yield a distribution function, and fluid moments are then calculated to in turn calculate macroscopic electromagnetic field fluctuations.

However, it is also possible to take moments at the stage of the Vlasov equation, obtaining moment equations which allow one to solve the complete dynamics on a macroscopic level. As has been discussed in the introduction 1.3.2, depending on the chosen closures this may lead to the neglect of some important physical effects. However, there are phenomena which can be adequately treated by fluid models, and furthermore phenomena for which important gyrokinetic effects do not enter for all plasma species.

In these cases, a considerable advantage in theoretical and computational simplicity can be obtained by considering fluid equations derived consistently from the kinetic formulation, either in isolation or coupled with a gyrokinetic treatment of other species. This particularly so when considering the electrons as a fluid species. The Courant condition imposed by the higher electron thermal velocity is relaxed to that of the ion thermal velocity, while error in calculation of the adiabatic part of the distribution function is dramatically reduced as it is proportional to the square root of the species mass (see section 3.8).

Numerically, this method was pioneered with the GEM code [89, 90] and the GTC code [91]. A derivation based on a small parameter expansion of the gyrokinetic equations was developed in the course of the latter work [91]. Here, we will present a standard derivation of an equation for the evolution of the perturbed electron density from a drift kinetic equation in the symplectic formulation presented in section 2.1.3 by taking a zeroth order moment.

### 2.2.1 Continuity equation from gyrokinetics

The gyrokinetic code EUTERPE, which will be discussed in greater detail in section 3, requires the charge and current of each species at each grid point in order to calculate the potentials needed to solve the gyrokinetic equations. Since the charge on each species is known, this means the density and flow velocity of each species is required. Since the gyrokinetic Vlasov equation will not be solved for the electrons, we require a

fluid equation for the evolution of the perturbed electron density. The perturbed electron flow velocity can be derived from Ampère's law given an appropriate momentum balance equation, which introduces a certain truncation of the physics.

Returning to the gyrokinetic equations from section 2.1.3, we drop the gyroaverages as the electron Larmor radius is considerably smaller than than the ion Larmor radius. This yields the drift-kinetic equation. We then integrate this drift kinetic equation over velocity space to obtain a zeroth order moment equation for the evolution of the perturbed electron density,

$$\int \frac{\partial f_{1s}}{\partial t} dv^3 + \int \dot{\vec{R}} \cdot \frac{\partial f_{1s}}{\partial \vec{R}} dv^3 + \int \dot{v}_{\parallel} \frac{\partial f_{1s}}{\partial v_{\parallel}} dv^3 = - \int \dot{\vec{R}} \cdot \frac{\partial F_{0s}}{\partial \vec{R}} dv^3 - \int \dot{v}_{\parallel} \frac{\partial F_{0s}}{\partial v_{\parallel}} dv^3, \quad (2.69)$$

where  $s = e$ . Note that we have separated the distribution function,  $f_s = F_{0s} + f_{1s}$  into a background,  $F_{0s}$ , and perturbed,  $f_{1s}$ , component, for reasons that will be explained in greater detail in section 3.

We define the first, second, and third velocity moments respectively as,

$$\int f_{s0} d^3 \vec{v} = n_{1s}, \quad (2.70)$$

$$\int f_{s0} v_{\parallel} d^3 \vec{v} = n_0 u_{\parallel 1s}, \quad (2.71)$$

and

$$\int f_{s0} v_{\parallel}^2 d^3 \vec{v} = \frac{1}{m_s} P_{\parallel 1s}, \quad \int f_{s0} v_{\perp}^2 d^3 \vec{v} = \frac{1}{m_s} P_{\perp 1s}. \quad (2.72)$$

These correspond to equations for the perturbed density,  $n_{1s}$ , perturbed parallel flow velocity,  $u_{\parallel 1s}$ , and perturbed pressures,  $P_{1s}$ . As the equations of motion contain terms up to quadratic in velocity, all of these terms will appear in the zeroth moment of the equation kinetic equation. Higher order moments will not appear and we consider them truncated to zero.

After some algebra, we obtain the following continuity equation, retaining pressure anisotropy and all non-linear terms,

$$\begin{aligned} & \frac{\partial n_{1e}}{\partial t} + n_0 \tilde{\vec{B}} \cdot \nabla \left( \frac{u_{\parallel 1e}}{B} \right) + B \vec{v}_E \cdot \nabla \left( \frac{n_{1e}}{B} \right) + \\ & \frac{\vec{B} \times \nabla B}{qB^2} \cdot \nabla \left( \frac{P_{\perp 1e}}{B} \right) + \frac{\vec{B} \times \nabla B}{qB^2} \cdot \nabla \left( \frac{P_{\parallel 1e}}{B} \right) + \frac{\nabla \times \vec{B}}{qB} \cdot \nabla \left( \frac{P_{\parallel 1e}}{B} \right) + \\ & n_{1e} \frac{\vec{B} \times \nabla B}{B^3} \cdot \nabla \phi + n_{1e} \frac{\nabla \times \vec{B}}{B^2} \cdot \nabla \phi + \\ & n_0 \left( \nabla \times A_{\parallel} \vec{b} \right) \cdot \nabla \left( \frac{u_{\parallel 0e}}{B} \right) + B \vec{v}_E \cdot \nabla \left( \frac{n_0}{B} \right) + \\ & n_0 \frac{\vec{B} \times \nabla B}{B^3} \cdot \nabla \phi + n_0 \frac{\nabla \times \vec{B}}{B^2} \cdot \nabla \phi \\ & = 0. \end{aligned} \quad (2.73)$$

In order to make this equation more tractable, we drop non-linear terms and impose pressure isotropy,  $P_{\parallel 1} = P_{\perp 1}$  to yield a linearised electron continuity equation,

$$\begin{aligned}
& \frac{\partial n_{1e}}{\partial t} + n_0 \vec{B} \cdot \nabla \left( \frac{u_{\parallel 1e}}{B} \right) + \\
& \frac{2\vec{B} \times \nabla B}{qB^2} \cdot \nabla \left( \frac{P_{1e}}{B} \right) + \frac{\nabla \times \vec{B}}{qB} \cdot \nabla \left( \frac{P_{1e}}{B} \right) + \\
& n_0 \left( \nabla \times A_{\parallel} \vec{b} \right) \cdot \nabla \left( \frac{u_{\parallel 0e}}{B} \right) + B \vec{v}_E \cdot \nabla \left( \frac{n_0}{B} \right) + \\
& n_0 \frac{\vec{B} \times \nabla B}{B^3} \cdot \nabla \phi + n_0 \frac{\nabla \times \vec{B}}{B^2} \cdot \nabla \phi \\
& = 0
\end{aligned} \tag{2.74}$$

One can see at once, then, that this equation, like the drift-kinetic equation, depends upon the perturbed electrostatic and magnetic potentials. It also depends on the first and second moments of the drift-kinetic equation, the perturbed parallel electron flow and the plasma pressure.

It is a known property of fluid equations that each moment will depend upon the subsequent higher moment, forming an infinite set of coupled equations. Although the physics of the parallel moment balance, given by the first order moment of the drift-kinetic equation, may be important enough to consider in greater detail, this series must eventually be truncated.

### 2.2.2 Ideal Ohm's law and advective pressure closure

The simplest closure for the parallel force balance (Ohm's law) is the ad-hoc ideal MHD condition,

$$E_{\parallel} = -\frac{\partial A_{\parallel}}{\partial t} - \nabla_{\parallel} \phi = 0, \tag{2.75}$$

This corresponds to the perturbed parallel electric field being approximated as zero. This can be a good approximation for many physical phenomena of interest, including the Toroidal Alfvén Eigenmode, ideal internal kink mode, and others. The approximation is generally not valid where resistive effects or electron inertia would be important.

With the pressure, the model is also truncated. The simplest truncation is to disregard the perturbed pressure,

$$P_{\parallel 1} = P_{\perp 1} = 0, \tag{2.76}$$

but this is of course often not sufficient for a good description. One approximation used in many codes is to postulate that the unperturbed pressure is advected with the  $\vec{E} \times \vec{B}$  velocity,

$$\frac{\partial P_{\parallel 1}}{\partial t} = \frac{\partial P_{\perp 1}}{\partial t} = -\vec{v}_E \cdot \nabla P_0. \tag{2.77}$$

which is the ideal MHD pressure equation (entropy conservation) with the assumption of incompressible flow,  $\nabla \cdot \vec{v} = 0$ .

A fusion device will have a negative gradient in pressure from the core to the edge, and in a high  $\beta$  plasma this pressure gradient can be the dominant source of free energy driving instability.

These equations are convenient for easy comparison with other codes, but are none necessarily the best choices and are not physically complete. Alternative closures will be considered in subsection 2.2.6.

### 2.2.3 Reduced MHD bulk plasma, gyrokinetic fast ion model

The above equations are easily applied to produce a further simplified model, in which the entire bulk plasma is treated as a fluid. Considering that a zeroth order moment can also be taken of the corresponding drift kinetic equation for the bulk ions, we obtain a corresponding equation for the evolution of the fluid ion density. This equation differs only in the sign of the charge and the species mass. Adding the two multiplied by the respective species charge, we obtain an equation for the evolution of the total perturbed charge density,

$$\frac{\partial \rho}{\partial t} = \frac{\partial(n_i - n_e)}{\partial t} \quad (2.78)$$

$$= -\vec{B} \cdot \nabla \left( \frac{j_{\parallel 1}}{B} \right) - (\nabla \times A_{\parallel} \vec{b}) \cdot \nabla \left( \frac{j_{\parallel 0}}{B} \right) - \rho_0 \vec{v}_* \cdot \frac{\nabla B}{B} - \frac{\nabla \times \vec{B}}{B^2} \cdot \nabla P_1, \quad (2.79)$$

where

$$\vec{v}_* = 2 \frac{\vec{b} \times \nabla P_1}{n_0 m_e B}. \quad (2.80)$$

Combining with the same closures as previously, we now have a model for the bulk plasma which can be coupled self-consistently with the gyrokinetic fast ion response. In this model, the kinetic effects of the entire thermal plasma are neglected, but the mode structure given by the perturbed fields' response to the thermal plasma will be modified by the kinetic effects of a species of energetic fast ions.

### 2.2.4 Recovery of reduced ideal MHD

The reduced ideal MHD equations can be expressed as a single vorticity equation for the perturbed electrostatic potential. By solving this equation, the reduced ideal MHD mode structure, frequency, and growth rate can be calculated.

Starting with the charge density equation obtained above, we substitute Ampère's law and the quasineutrality equation,

$$-\nabla_{\perp}^2 A_{\parallel} = \mu_0 j_{\parallel 1} \quad -\nabla_{\perp} \frac{m_i n_0}{B^2} \nabla_{\perp} \phi = \rho_1, \quad (2.81)$$

to yield,

$$-\frac{\partial}{\partial t} \nabla_{\perp} \left( \frac{m_i n_0}{B^2} \nabla_{\perp} \phi \right) - \frac{\vec{B}}{\mu_0} \cdot \nabla \left( \frac{\nabla_{\perp}^2 A_{\parallel}}{B} \right) + (\nabla \times A_{\parallel} \vec{b}) \cdot \nabla \left( \frac{j_{\parallel 0}}{B} \right) + \quad (2.82)$$

$$\rho_0 \vec{v}_* \cdot \frac{\nabla B}{B} + \frac{\nabla \times \vec{B}}{B^2} \cdot \nabla P_1 = 0 \quad (2.83)$$

Taking a time derivative of this equation, and substituting the ideal MHD Ohm's law and pressure advection equations,

$$\frac{\partial A_{\parallel}}{\partial t} = -\nabla_{\parallel}\phi \quad \frac{\partial P_{\parallel 1}}{\partial t} = \frac{\partial P_{\perp 1}}{\partial t} = -\vec{v}_E \cdot \nabla P_0, \quad (2.84)$$

we obtain,

$$-\frac{\partial^2}{\partial t^2} \nabla_{\perp} \left( \frac{m_i n_0}{B^2} \nabla_{\perp} \phi \right) + \frac{\vec{B}}{\mu_0} \cdot \nabla \left( \frac{\nabla_{\perp}^2 \nabla_{\parallel} \phi}{B} \right) - \left( \nabla \times \vec{b} \nabla_{\parallel} \phi \right) \cdot \nabla \left( \frac{j_{\parallel 0}}{B} \right) - \quad (2.85)$$

$$\left( \rho_0 \frac{\nabla B}{B} \cdot \frac{\vec{b} \times \nabla (\vec{v}_E \cdot \nabla P_0)}{n_0 m_e B} - \frac{\nabla \times \vec{B}}{B^2} \cdot \nabla (\vec{v}_E \cdot \nabla P_0) \right) = 0. \quad (2.86)$$

With the assumption of zero pressure gradient and zero equilibrium current, which is sufficient to retain the Shear Alfvén wave (SAW), we obtain the following simplified vorticity equation,

$$-\frac{\partial^2}{\partial t^2} \nabla_{\perp} \left( \frac{m_i n_0}{B^2} \nabla_{\perp} \phi \right) + \frac{\vec{B}}{\mu_0} \cdot \nabla \left( \frac{\nabla_{\perp}^2 \nabla_{\parallel} \phi}{B} \right) = 0, \quad (2.87)$$

Making the substitution,

$$\phi(r, t) = \phi_0 e^{i(\vec{k} \cdot \vec{r} - \omega t)}, \quad (2.88)$$

we derive a relation between the mode frequency  $\omega$  and mode wave number  $k_{\parallel}$ ,

$$\frac{1}{v_A^2} \omega^2 = k_{\parallel}^2, \quad (2.89)$$

where the Alfvén velocity,  $v_A$ , is defined as,

$$v_A = \frac{B}{\sqrt{\mu_0 m_i n_0}}. \quad (2.90)$$

This is the familiar dispersion relation for the SAW, which is the foundation of many of the physical phenomena of interest.

## 2.2.5 Comparison with perturbative code CKA-EUTERPE

The perturbative hybrid code package CKA-EUTERPE [51] calculates a reduced ideal MHD eigenfunction by solving the equation,

$$\omega^2 \nabla \cdot \left( \frac{1}{v_A^2} \nabla_{\perp} \phi \right) + \nabla \cdot \left[ \vec{b} \nabla_{\perp}^2 (\vec{b} \cdot \nabla) \phi \right] + \nabla \cdot \left[ \vec{b} \nabla \cdot \left( \frac{\mu_0 j_{\parallel}}{B} \vec{b} \times \nabla \phi \right) \right] \quad (2.91)$$

$$- \nabla \cdot \left( \frac{2\mu_0}{B^2} \left[ (\vec{b} \times \nabla \phi) \cdot \nabla p \right] (\vec{b} \times \vec{\kappa}) \right) = 0$$

for the perturbed electrostatic potential,  $\phi$ . The curvature tensor,  $\vec{\kappa}$  is defined as follows,

$$\vec{\kappa} = \vec{b} \cdot \nabla \vec{b} = \left( \nabla \times \vec{b} \right) \times \vec{b}. \quad (2.92)$$

Note that as before the ansatz  $\phi(s, t) = \phi(s)e^{-i\omega t}$  has been applied, eliminating the time derivative, as CKA is an eigenvalue code solving a time-independent problem. CKA therefore yields a reduced ideal MHD real frequency and growth rate in addition to the time independent mode structure.

The equation to be solved here may be compared with equation 2.87, which should yield similar solutions. The detailed derivation of this equation also proceeds by taking moments of the drift-kinetic Vlasov equation, and can be found in [51]. The pressure and  $E_{\parallel}$  truncations employed in CKA are identical to those posited for the fluid-electron hybrid model.

## 2.2.6 Non-ideal closures

In addition to the ideal MHD closure, it can be useful to add terms to represent other physical effects. One, for instance, is resistivity, which can be rigorously modelled by an energy and momentum-conserving collision operator, but which may be economically approximated by an additional term in Ohm's law. A simple model of a collisional plasma is to posit a finite perturbed parallel electric field proportional to a scalar resistivity,  $\eta$ :

$$E_{\parallel} = -\frac{\partial A_{\parallel}}{\partial t} - \nabla_{\parallel}\phi = -\eta\nabla_{\perp}^2 A_{\parallel}. \quad (2.93)$$

Even where resistive physics are not specifically of interest, it is often useful to include a damping mechanism for numerical stability, a role which can be filled by a resistivity term. Note that this damping mechanism acts most strongly for large perpendicular wavenumber  $k_{\perp}\rho_i$ . It is therefore of particular use damping fine scale structures that may emerge during non-linear simulations.

The resistive term is the only non-ideal closure currently implemented in the code or considered in this work. So far in this chapter, we have chosen to truncate the first moment at zero and the second in terms of advection of the background pressure gradient. This is not strictly consistent, as a complete first moment equation could be derived in the same way as the continuity equation.

We can treat higher order moments in exactly the same way as we have treated the zeroth moment. By multiplying the gyrokinetic equation by  $v_{\parallel}$  and integrating again over all phase space, we can obtain an equation for the first order moment in terms of the zeroth and second order moments.

In the limit  $m_e \rightarrow 0$ , and taking the first moment of the drift-kinetic equation 2.69, we find the following Ohm's law,

$$E_{\parallel} = -\frac{\vec{b}}{en_0} \cdot \nabla P_{\parallel 1e} - \frac{\nabla \times A_{\parallel} \vec{b}}{en_0 B} \cdot \nabla (P_{\parallel 0e} - en_0 \phi). \quad (2.94)$$

The massless electron approximation is justified for small but finite electron beta,  $\beta_e m_i / m_e \gg 1$ , which for a proton-electron plasma requires an electron  $\beta$  considerably greater than 0.05%, which is justified in most tokamak experiments. Note that at high  $\beta$  the assumption of zero  $B_{\parallel 1}$  is violated. A magnetic mirror term (i.e. proportional to  $\nabla B$ ) is also present at the same order as these, but can be neglected if it is assumed that passing particles carry most of the electron current [60].

This first order moment equation depends in turn upon the second order moment,  $P_{1e}$ . It can be seen from the structure of the equations that every moment must be dependent on terms of a higher order. The complete system of fluid moment equations is therefore infinite, and must be truncated somewhere.

Further extensions are also possible and have been proposed [60] but not considered in this work. One can for instance include terms for a gyrofluid closure and finite electron inertia. These possibilities have not been investigated numerically in this work, but will be briefly discussed for completeness.

In a gyrofluid model an additional term appears, similar in form to the resistive dissipation term [92],

$$E_{\parallel} = \eta_{Lf} \nabla_{\parallel} J_{\parallel,e}, \quad (2.95)$$

where the collisionless dissipation term  $\eta_{Lf}$ , is given by,

$$\eta_{Lf} = \frac{\sqrt{\pi}}{2} \frac{v_{te}}{e^2 n_0}. \quad (2.96)$$

The combination of gyrokinetic and gyrofluid codes has not been pursued significantly but may be a future area of interest. Gyrofluid codes are used successfully to simulate both microturbulence [93] and global modes such as Alfvén eigenmodes [94], and could be expanded by the inclusion of gyrokinetic models for ion species while retaining many of the same numerical advantages as drift-fluid models.

Finite electron inertia, meanwhile, can be included into the finite parallel force balance equation (Ohm’s law) in the simple form,

$$n_0 m_e \frac{\partial u_{\parallel 1e}}{\partial t}, \quad (2.97)$$

although numerical implementation with an explicit scheme may be more challenging. Finite electron inertia is not considered in the frame of this work with the fluid and fluid hybrid models. With the exception of resistivity, these closures represent possible future directions for expansion of the code.



# Chapter 3

## Numerical implementation

This work concerns the numerical simulation of physical systems. In the previous chapters, the problems of interest have concisely summarised and the mathematical models we will use to treat them have been derived and their key properties described. In this section, the numerical approach to solving these model equations will be explored in detail.

The principal numerical tool is the gyrokinetic code EUTERPE, developed first at EPFL Lausanne [95] and later at IPP Greifswald [96]. First, the code will be described in overview, with its numerical methods, capabilities, and limitations. Second, the importance of the ‘cancellation problem’ will be discussed, along with the methods used to mitigate it in EUTERPE. Avoiding and/or mitigating this numerical problem has been a key motivator of this work. Finally, the implementation of the hybrid models described in section 2.2 will be described.

### 3.1 EUTERPE code overview

EUTERPE is an initial-value solver for the non-linear, electromagnetic gyrokinetic equations described in section 2 for up to three particle species in arbitrary 3D magnetic geometry. It employs the well-known particle-in-cell (PIC) method.

In the PIC method, large numbers of physical particles are abstracted by a smaller number of representative numerical ‘super-particles’, referred to here as markers. A separate marker species is employed for each physical species, defined by a mass and charge. The PIC method can be regarded as a method of combining the properties of Eulerian and Monte Carlo approaches for solving partial differential equations numerically, in which the dimensionality of the problem is reduced by replacing a 2D grid for the velocity space with markers.

The drawback of this approach is that it introduces the Monte Carlo error scaling proportional to  $1/\sqrt{N}$ . The resulting numerical noise has been a significant issue for PIC codes. It has not always been possible to accurately distinguish physical effects from artefacts of noise [97]. In EUTERPE, the ‘delta f’ method is used to mitigate this problem.

The markers discretise the distribution function for each species. Characteristics of the markers are traced in continuous phase space by solving the gyrokinetic equations of

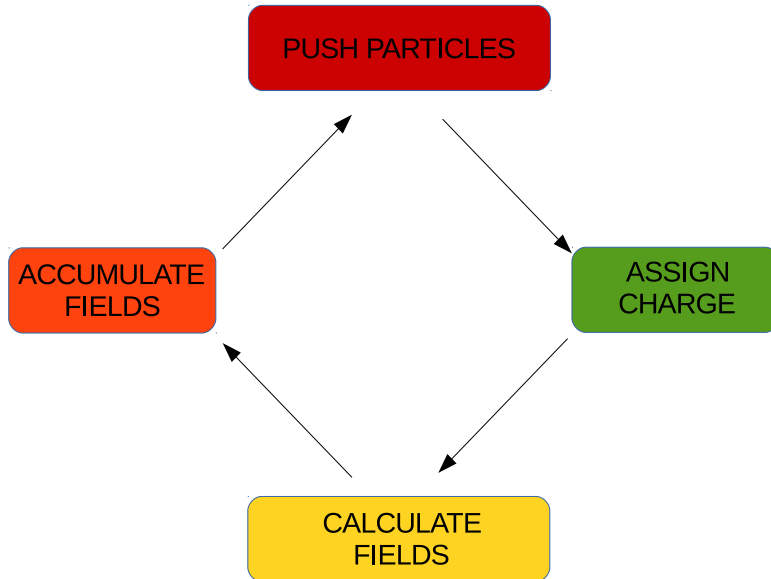


Figure 3.1: Flow chart illustration of the PIC method. The markers are moved according to characteristic equations depending on the perturbed potentials,  $\phi$  and  $A_{\parallel}$ . The position and velocity of the markers is then used to calculate the charge and current density at each grid point. The quasi-neutrality equation and Ampère’s law is then solved at each grid point to yield potential values at each grid point. The potentials acting on each particle are then interpolated and summed from the nearby grid points.

motion. These equations of motion in turn depend upon the electrostatic and magnetic potentials,  $\phi$  and  $A_{\parallel}$ , which are taken from a fixed Eulerian grid.

Having evolved the markers along the characteristics to calculate their positions and velocities at a subsequent timestep, moments are taken to accumulate the charge and current at each grid position. From these charges and currents for each species, matrix equations for Ampère’s law and the quasi-neutrality equation are then solved to calculate the self-consistent electrostatic and magnetic potentials.

Iterating these steps, it is possible to calculate the potentials and moments at any later timestep, subject to limitations of accumulating numerical error. A schematic of the EUTERPE code is shown in figure 3.1.

EUTERPE can solve either gyrokinetic or drift kinetic equations, that is it can solve these equations assuming a physical Larmor radius or zero Larmor radius. The Larmor radius enters by assigning charge and current from an average of those markers on a ring of the Larmor radius, within the precision of the grid, and subsequently accumulating potentials averaged over their values at different positions on such a ring.

### 3.1.1 Gyrokinetic solver

EUTERPE solves the non-linear gyrokinetic Vlasov equation,

$$\frac{df_s}{dt} = \frac{\partial f_s}{\partial t} + \dot{\vec{R}} \cdot \frac{\partial f_s}{\partial \vec{R}} + \dot{\mu} \frac{\partial f_s}{\partial \mu} = 0. \quad (3.1)$$

Like many gyrokinetic codes, EUTERPE employs the ‘delta f’ method to reduce noise. In this approach, the code splits the distribution function into perturbed and background parts,

$$f_s = F_{0s} + f_{1s}, \quad (3.2)$$

and solves for perturbations in the fields and distribution functions,  $f_{s1}$ , as against an assumed static background,  $F_{0s}$ .

In this work the static background  $F_0$  will always be taken to be Maxwellian. Although a fusion plasma is not necessarily in equilibrium, the background plasma evolves on a timescale much longer than that of the instabilities we consider, and so we can approximate the background plasma as being a static equilibrium. In specifying the background distribution function, the perpendicular velocity  $v_\perp$  is used as a variable in place of the magnetic moment,  $\mu$ .

Substituting the split distribution function in equation 3.2 into the Vlasov equation 3.1, we obtain an equation in terms of the perturbed and background components of the distribution function,

$$\begin{aligned} \frac{df_s}{dt} &= \frac{dF_{0s}}{dt} + \frac{df_{1s}}{dt} = 0 \quad (3.3) \\ \frac{df_s}{dt} &= \underbrace{\frac{\partial F_{0s}}{\partial t} + \dot{\vec{R}} \cdot \frac{\partial F_{0s}}{\partial \vec{R}} + \dot{v}_\parallel \frac{\partial F_{0s}}{\partial v_\parallel} + \dot{v}_\perp \frac{\partial F_{0s}}{\partial v_\perp}}_{dF_{0s}/dt} + \underbrace{\frac{\partial f_{1s}}{\partial t} + \dot{\vec{R}} \cdot \frac{\partial f_{1s}}{\partial \vec{R}} + \dot{v}_\parallel \frac{\partial f_{1s}}{\partial v_\parallel} + \dot{\mu} \frac{\partial f_{1s}}{\partial \mu}}_{df_{1s}/dt} = 0 \quad (3.4) \end{aligned}$$

The superscripts (0) and (1) are now introduced for the equations of motion, signifying those components independent of and dependent on the perturbed potentials respectively. Note that in all formulations of the equations of motion,  $\mu$  is constant to the relevant order.

In all cases the sum of the purely linear contributions, proportional to  $\dot{Z}^{(0)} \cdot F_{0s}$ , are set to zero. It is always possible to choose a distribution function  $F_{0s}$  such that this is true for an axisymmetric geometry. Although this does not necessarily hold for stellarators, in general we are interested in timescales much shorter than those on which the background distribution function would change.

We therefore solve the equations,

$$\frac{\partial f_{1s}}{\partial t} + \dot{\vec{R}} \cdot \frac{\partial f_{1s}}{\partial \vec{R}} + \dot{v}_\parallel \frac{\partial f_{1s}}{\partial v_\parallel} = -\dot{\vec{R}}^{(1)} \cdot \frac{\partial F_{0s}}{\partial \vec{R}} - \dot{v}_\parallel^{(1)} \frac{\partial F_{0s}}{\partial v_\parallel} - \dot{v}_\perp \frac{\partial F_{0s}}{\partial v_\perp}, \quad (3.5)$$

where linear and non-linear terms are both retained in the equations of motion on the left hand side. For linear simulations, these are omitted, so that the equations solved

are,

$$\frac{\partial f_{1s}}{\partial t} + \dot{\vec{R}}^{(0)} \cdot \frac{\partial f_{1s}}{\partial \dot{\vec{R}}} + \dot{v}_{\parallel}^{(0)} \frac{\partial f_{1s}}{\partial v_{\parallel}} = -\dot{\vec{R}}^{(1)} \cdot \frac{\partial F_{0s}}{\partial \dot{\vec{R}}} - \dot{v}_{\parallel}^{(1)} \frac{\partial F_{0s}}{\partial v_{\parallel}} - \dot{v}_{\perp}^{(1)} \frac{\partial F_{0s}}{\partial v_{\perp}}, \quad (3.6)$$

The equation for the time derivative of the perpendicular velocity is,

$$\frac{dv_{\perp}}{dt} = \frac{d}{dt} \sqrt{\frac{2B\mu}{m}} = \sqrt{\frac{2\mu}{mB}} \frac{1}{2} \nabla B \cdot \dot{\vec{R}} = \frac{v_{\perp}}{2B} \nabla B \cdot \dot{\vec{R}}, \quad (3.7)$$

which allows us to eliminate the explicit dependence on this variable.

At this point it is possible to write an equation for the evolution of the perturbed distribution function in terms of known quantities. This is as follows,

$$\frac{df_{1s}}{dt} = -\dot{\vec{R}}^{(1)} \cdot \frac{\partial F_{0s}}{\partial \dot{\vec{R}}} - \dot{v}_{\parallel}^{(1)} \frac{\partial F_{0s}}{\partial v_{\parallel}} + \frac{v_{\perp}}{2B} \nabla B \cdot \dot{\vec{R}} \frac{\partial F_{0s}}{\partial v_{\perp}} = S^{(1)}. \quad (3.8)$$

The perturbed distribution function is discretised in terms of markers. It is defined as follows,

$$f_{1s}(\vec{R}, v_{\parallel}, \mu, t) = \sum_{\nu=1}^{N_p} w_{\nu}(t) \frac{1}{J} \delta(\vec{R} - \vec{R}_{\nu}) \delta(v_{\parallel} - v_{\parallel}) \delta(\mu - \mu_{\nu}), \quad (3.9)$$

where  $N_p$  is the number of markers,  $w$  is the weight of a marker, which quantifies the proportion of physical particles that are represented by that marker, and  $J$  is the Jacobian in the relevant coordinate system.

Substituting equation 3.9 into equation 3.8, and integrating over a phase space volume  $\Omega_p$  centred on the marker, gives an equation for the evolution of the marker weights,

$$\frac{1}{dt} \int_{\Omega_p} J \sum_p w_p(t) \frac{1}{J} \delta(\vec{R} - \vec{R}_{\nu}) \delta(v_{\parallel} - v_{\parallel}) \delta(\mu - \mu_{\nu}) = - \int_{\Omega_p} d^6z JS^{(1)}(\vec{R}_k(t), t) \quad (3.10)$$

which, upon performing the integral, gives the simplified relation,

$$\dot{w}_p = -S^{(1)} \Omega_p = -\frac{F_{0s} \Omega_p}{N_{ph}} \left[ \dot{\vec{R}}^{(1)} \frac{\nabla F_{0s}}{F_{0s}} + \dot{v}_{\parallel}^{(1)} \frac{1}{F_{0s}} \frac{\partial F_{0s}}{\partial v_{\parallel}} + \frac{v_{\perp}}{2B} \dot{\vec{R}}^{(1)} \cdot \nabla B \frac{1}{F_{0s}} \frac{\partial F_{0s}}{\partial v_{\perp}} \right]. \quad (3.11)$$

The equations of motion,  $\dot{\vec{R}}$  and  $\dot{v}_{\parallel}$ , where are necessary to solve this set of equations, are different depending upon the formulation chosen, and are shown in section 2.1. Note that, depending upon the chosen formulation,  $v_{\parallel}$  does not necessarily correspond to the physical velocity of the particle; referring to equation 2.41, we can see that this correspondence holds in the symplectic formulation but not in the canonical momentum or mixed variables formulations.

### 3.1.2 Distribution functions

The Maxwellian unperturbed distribution function,  $F_{s0}$ , is defined as,

$$F_{0s} = \frac{n_{0s}(s_0)}{(2\pi)^{3/2}v_{th,s}^3} \exp\left(-\frac{v_{\parallel}^2 + v_{\perp}^2}{2v_{th,s}^2}\right), \quad (3.12)$$

where  $v_{th,s}$  is the thermal velocity of each species,

$$v_{th,s}(s_0) = \sqrt{\frac{T_s(s_0)}{\bar{m}_s}}. \quad (3.13)$$

Note that the phase space variable  $v_{\parallel}$  has been used to characterise the Maxwellian distribution function.

Although not used in this work, other distribution functions are also included in the EUTERPE code. These are especially suited for modelling energetic particle populations, which are often not in thermal equilibrium. Two such distribution functions are the slowing down, and triple slowing down distribution functions. These attempt to model the collision of a beam of particles produced at a given velocity with the thermal plasma.

The slowing down distribution is a simple model of such an interaction between an energetic particle beam and a thermal plasma. It is given by the equations,

$$F_{0s} = n(r) \frac{N}{v_{crit}^3 + v^3} F_{0s} = 0 \quad (3.14)$$

where the constant,  $N$ , is given by

$$N = \left(4\pi \int_0^{v_{beam}} v^2 \frac{1}{v_{crit}^3 + v^3} dv\right)^{-1}, \quad (3.15)$$

the critical velocity,  $v_{crit}$ , is given by

$$v_{crit}^3 = \frac{3\sqrt{\pi}}{4} \frac{m_e}{m_{fast}} v_e^3, \quad (3.16)$$

and it is assumed that  $v_i < v_{beam} < v_e$ , where the thermal velocities  $v_s = \sqrt{2T_s/m_s}$ .

The triple slowing down distribution function is a development on this concept intended to model Neutral Beam Injection (NBI).

### 3.1.3 Gyrokinetic field equations

Solving the Vlasov equation for each species gives the perturbed distribution function for each species, depending upon the perturbed potentials. In order to calculate the perturbed fields at the subsequent timestep, two further equations must be solved, the quasi-neutrality equation and Ampère's law,

$$-\nabla \cdot \left[ \left( \sum_{s=i,f} \frac{q_s^2 n_s}{T_s} \rho_s^2 \right) \nabla_{\perp} \phi \right] = \sum_{s=i,e,f} q_s n_{1s} \quad (3.17)$$

$$\left( \sum_{s=i,e,f} \frac{\hat{\beta}_s}{\rho_s^2} - \nabla_{\perp}^2 \right) A_{\parallel} = \mu_0 \sum_{s=i,e,f} j_{\parallel 1s}, \quad (3.18)$$

where  $d^6Z = B_{\parallel}^* d\vec{R} dv_{\parallel} d\mu d\theta$  defines the phase-space volume,  $\rho_s = \sqrt{m_s T_{0s}} / (eB)$  is the thermal gyroradius and  $\hat{\beta}_s = \mu_0 n_{0s} T_{0s} / B_0^2$  is the EUTERPE-defined ‘partial’ plasma beta for each species. The polarization density is treated in the long-wavelength approximation. Finite Larmor radius (FLR) effects are neglected for electrons. The zeroth-order densities of the particle species satisfy the quasineutrality equation  $\sum_s q_s n_s = 0$  with  $s = i, e, f$ .

The density and current moments are defined as

$$n_{1s} = \int d^6Z f_{1s} \delta(\vec{R} + \vec{\rho} - \vec{x}) \quad (3.19)$$

and

$$j_{\parallel 1s} = q_s \int d^6Z f_{1s} v_{\parallel} \delta(\vec{R} + \vec{\rho} - \vec{x}). \quad (3.20)$$

The fields are discretised on the grid using the finite element method, defining the potentials as,

$$A_{\parallel}(\vec{x}, t) = \sum_{\nu} a_{\nu} \Lambda_{\nu}(\vec{x}) \quad (3.21)$$

and

$$\phi(\vec{x}, t) = \sum_{\nu} \Phi_{\nu} \Lambda_{\nu}(\vec{x}), \quad (3.22)$$

where  $\Lambda_{\nu}$  is a tensor product of unidimensional B-splines of order  $k$ ,

$$\Lambda_{\nu} = B_l^k(r) B_m^k(\chi) B_n^k(\psi). \quad (3.23)$$

B-splines consistently maintain energy and particle conservation.

The complete quasineutrality (long-wavelength approximation) and Ampère’s law equations given for the  $p_{\parallel}$  formulation in section 2.1.4 are therefore discretised in terms of splines as follows,

$$- \int d\vec{x} \Lambda_k(\vec{x}) \nabla_{\perp} \cdot \left( \frac{en_0}{T_i} \rho_i^2 \nabla_{\perp} \phi \right) = \int d\vec{x} \Lambda_k(\vec{x}) (\bar{n}_i(\vec{x}) - n_e(\vec{x})) \quad (3.24)$$

$$\int d\vec{x} \Lambda_k(\vec{x}) \left[ \frac{\beta_e}{\rho_e^2} + \frac{\beta_i}{\rho_i^2} - \nabla_{\perp}^2 A_{\parallel} \right] = \mu_0 \int d\vec{x} \Lambda_k(\vec{x}) (\bar{j}_{\parallel i}(\vec{x}) + j_{\parallel e}(\vec{x})), \quad (3.25)$$

so that the two equations take the form,

$$\sum_{l=1}^{N_s} M_{kl}^{(Q)} \Phi_l = N_k^{(Q)}, \quad \sum_{l=1}^{N_s} M_{kl}^{(A)} a_l = N_k^{(A)}, \quad (3.26)$$

where the matrices are given by the equations,

$$M_{kl}^{(Q)} = \frac{m_i}{e^2} \int d\vec{x} \frac{n_0}{B^2} \nabla_{\perp} \Lambda_l \cdot \nabla_{\perp} \Lambda_k \quad (3.27)$$

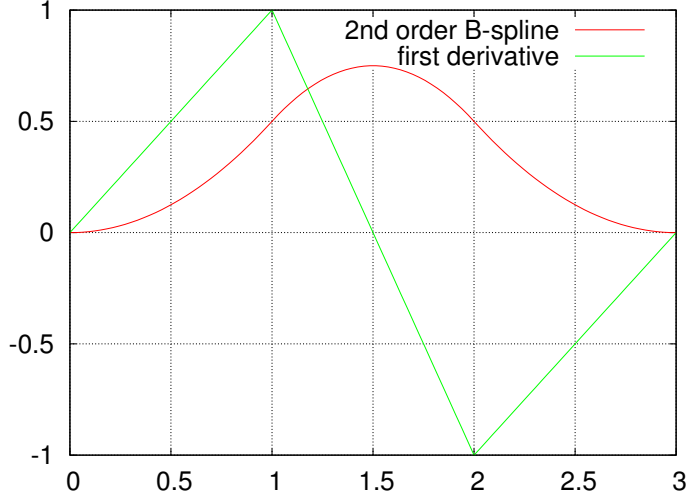


Figure 3.2: A depiction of a quadratic B-spline and its first derivative. Note that the derivatives of B-splines are well-defined functions.

$$M_{lk}^{(A)} = \frac{e}{m_e} \int d\vec{x} n_0 \Lambda_k \Lambda_l + \frac{e}{m_i} \int d\vec{x} n_0 \Lambda_k \Lambda_l + \frac{1}{e\mu_0} \int \nabla_{\perp} \Lambda_k \cdot \nabla_{\perp} \Lambda_l. \quad (3.28)$$

Corresponding equations are required and can be derived simply by the same method for the  $v_{\parallel}$  and mixed variables formulations of the equations of motion. For the hybrid models, a B-spline discretisation will also be required for the continuity equation used to calculate the electron density fields.

## 3.2 Finite Larmor radius

The gyroaverage operator,

$$\langle z \rangle = \int \frac{d\theta}{2\pi} z(\vec{R} + \vec{\rho}) \quad (3.29)$$

is executed numerically by means of an N-point fixed sum method. The quantity is averaged over the neighbouring grid points,  $k$ , to the value at  $N_c$  positions on a circle of radius  $\rho_s$  around the marker perpendicular to the magnetic field, as illustrated in figure 3.3 and given by the equation

$$\langle z \rangle \approx \sum_{k=1}^N \frac{1}{N} z(\vec{R} + \vec{\rho}_k). \quad (3.30)$$

The potentials are calculated by averaging the perturbed densities and currents along the gyroring, and the perturbed densities and currents are in turn assigned by averaging over all markers whose gyrorings intersect a given grid point.

The number of points,  $N_c$ , should vary with gyroradius, a large number being required to accurately average the potentials as the gyroradius grows larger. For gy-

rokinetic simulations of fast particle interaction with global modes, and hence in most simulations presented in this work,  $N_c = 32$  points are taken.

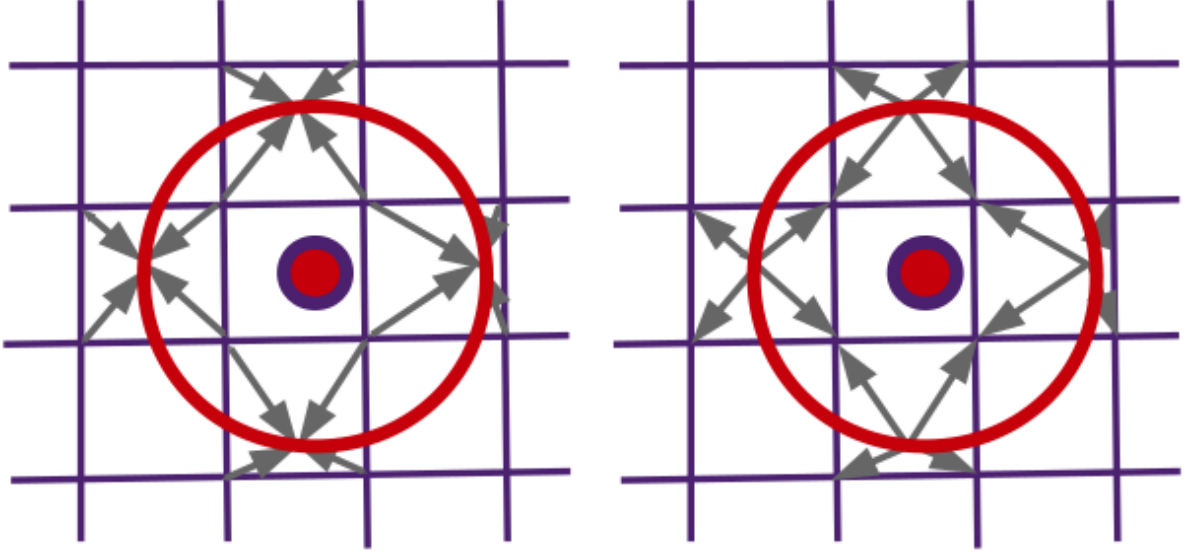


Figure 3.3: The implementation of the finite Larmor radius in PIC: an average field influences the particle trajectories based on average sampling over many grid points lying on the gyroring (left) and the charge and current are assigned from sampling multiple particles whose gyrorings pass close to it (right).

### 3.3 Coordinates

The EUTERPE code uses magnetic (PEST) coordinates  $(s, \theta, \varphi)$  for the perturbed fields  $\varphi$  and  $A_{\parallel}$ , and cylindrical co-ordinates  $(R, \varphi, Z)$  to calculate the motion of the markers.

The PEST coordinate system is defined such that the magnetic field lines are straight. The magnetic field can be expressed in terms of the physical quantities,

$$\vec{B} = \nabla\varphi \times \nabla\chi(s) + \nabla\Psi(s) \times \nabla\theta, \quad (3.31)$$

where  $\varphi$  and  $\theta$  are respectively the geometrical toroidal angle and the poloidal angle in a coordinate system such that the magnetic field lines are straight.  $2\pi\chi(s)$  and  $2\pi\Psi(s)$  are the poloidal and toroidal fluxes respectively. The flux label  $s$  is the normalised toroidal flux,

$$s = \frac{\Psi}{\Psi_a}, \quad (3.32)$$

where  $\Psi_a$  is the label of the last closed flux surface in the toroidal device.

This coordinate system is advantageous because the fast particle movement along the field lines is substantially simplified by following a straight trajectory. In terms of the spatial grid, short length scale changes in the direction of the magnetic field lines do not need to be resolved.



In EUTERPE, the poloidal angle  $\varphi$  is chosen such that it coincides with the angle in the cylindrical coordinate system.

### 3.4 Normalisation

The physical quantities in EUTERPE are normalised as follows.

The magnetic field strength is expressed as a ratio of the magnetic field strength on axis and the temperature as a ratio of the electron temperature at the defined flux surface,  $s_0$ ,

$$B_* = B(s = 0, \varphi = 0), \quad T_* = T_e(s_0). \quad (3.33)$$

The length scale is defined in terms of the gyroradius for a proton in a plasma with temperature  $T_*$  and magnetic field strength  $B_*$ ,

$$r_* = \frac{\sqrt{k_B T_* m_p}}{|e| B_*}. \quad (3.34)$$

Note that unless  $s_0 = 0.0$  and a hydrogen plasma is being considered, this does not correspond to the actual ion Larmor radius anywhere in the plasma.

The time scale is defined in terms of the cyclotron frequency,

$$\Omega_* = \frac{|e| B_*}{m_p}. \quad (3.35)$$

The velocity is therefore normalised in terms of the two preceding quantities,

$$v_* = r_* \Omega_* = \sqrt{\frac{k_B T_*}{m_p}}. \quad (3.36)$$

The perturbed electrostatic and magnetic potentials are normalised in terms of the normalised radius, magnetic field, and temperature,

$$\phi_* = \frac{k_B T_*}{|e|}, \quad A_{||*} = r_* B_*. \quad (3.37)$$

The density is defined in terms of the volume averaged ion density,

$$n_* = n_{av} = \frac{N_{ph,i}}{V} \quad (3.38)$$

and consequently the current is normalised as,

$$j_* = |e| n_* v_*. \quad (3.39)$$

### 3.5 Fourier filtering

In order to mitigate noise, reduce the required resolution, and save computational expense, it is useful to impose a filter in Fourier space that excludes harmonics outside the range of interest. As EUTERPE considers the full torus, simulations are filtered in both poloidal and toroidal harmonics, with numbers  $m$  and  $n$  respectively.

At each timestep, a Fast Fourier Transform (FFT) is performed on the perturbed potentials after they have been calculated. The desired harmonics are extracted and an inverse Fourier transform is performed on this filtered group of harmonics. It is these, filtered, potentials which are then used in the equations of motion to calculate the motion of the markers.

Specifying the maximum and minimum mode numbers to be included in  $m$  and  $n$ , the filtering operation results in the following equations,

$$\mathcal{W}\phi \rightarrow \sum_{m=m_{min}}^{m_{max}} \sum_{n=n_{min}}^{n_{max}} \phi(m, n) \quad (3.40)$$

$$\mathcal{W}A_{\parallel} \rightarrow \sum_{m=m_{min}}^{m_{max}} \sum_{n=n_{min}}^{n_{max}} A_{\parallel}(m, n) \quad (3.41)$$

where  $\mathcal{W}$  is the filter operator.

In this example, a rectangular filter is used, but the shape of the filter may be adapted to the problem, and multiple domains that are not contiguous in poloidal harmonics may also be selected. One particularly useful filter follows the safety factor profile for a given range of parallel wave numbers,  $k_{\parallel}$ , according to the equation 1.12. This results in a filter lying diagonally in harmonic number phase space. This concept has previously been applied in turbulence simulations but will later be used in non-linear TAE studies.

### 3.6 Phase factor transformation

The phase factor transformation is another technique which takes advantage of knowledge of how the mode of interest is localised in terms of poloidal and toroidal Fourier harmonics  $m$  and  $n$ . The advantage of this approach is that, instead of calculating all harmonics up to the maximum and minimum in  $m$  and  $n$  and then discarding unwanted components via Fourier filtering, these unwanted components need not be computed at all.

The phase factor transformation is a numerical technique that permits the simulation to be shifted in Fourier space. To simulate modes with higher poloidal and toroidal mode numbers, then, fewer modes in total must be included in the Fourier filter, and less poloidal and toroidal resolution is therefore required. This method is particularly useful for high mode number simulations, e.g. of ion temperature gradient-driven (ITG) turbulence, but has some application also for the simulation of low mode number global modes.

For linear simulations, the ansatz

$$\phi(s, \theta^*, \psi, t) = \bar{\phi}(s, \theta^*, \psi, t) e^{i(m_0 \theta^* + n_0 \psi)} \quad (3.42)$$

can be made, where  $\bar{\phi}$  represents the extracted electrostatic potential.

As the phase factor enters the quasi-neutrality and Ampère's law equations, it is fixed in the calculation of the matrices at the beginning of the simulation, requiring additional terms.

An important practical limitation of the current implementation is that the technique is only available for linear simulations. Non-linear simulations will therefore often require greater toroidal resolution with consequent increase in computational expense.

### 3.7 Plasma equilibrium

EUTERPE calculates the evolution of perturbed quantities on a short timescale. It does so against a fixed background (unperturbed) magnetic field structure, which can be considered an initial condition for the magnetic configuration. Physically, large changes in the magnetic configuration would occur on a timescale that is long in comparison to the timescale of simulations of phenomena of interest, so it is justifiable to rule out such evolution.

The background magnetic field structure is calculated separately and taken by EUTERPE as an input. Through the unperturbed magnetic field,  $B_0$ , this determines the magnetic geometry of the simulation. In the both fluid and kinetic models, derived quantities are calculated from the equilibrium.

In the fluid models, the equilibrium current is calculated from the equilibrium by the equation,

$$j_{\parallel 0e} = \frac{1}{\mu_0} \nabla \times \vec{B}_0, \quad (3.43)$$

on the assumption that the total equilibrium parallel current is dominated by that carried by the electrons. In the kinetic models, a corresponding calculation is performed to account for the equilibrium parallel current in the definition of the equilibrium distribution function.

A plasma is in MHD equilibrium when the magnetic pressure balances the thermal pressure, that is,

$$\vec{j} \times \vec{B} = \nabla P. \quad (3.44)$$

The equilibria considered in this work have been calculated using the Variational Moments Equilibrium Code (VMEC). [98, 99] This code calculates a 3-D magnetic equilibrium by minimising the MHD energy functional,

$$W = \int_{\Omega_p} \left( \frac{1}{2\mu_0} B^2 + p \right) \cdot dV. \quad (3.45)$$

The VMEC code assumes that the magnetic field lines form nested flux surfaces, which is not the case for stellarators in general. It can, however, be an acceptable approximation in the case where the size of magnetic islands is small.

To calculate an equilibrium in fixed boundary mode, VMEC takes a definition of the position edge of the plasma, a peak magnetic field on axis, a safety factor profile, and a pressure profile. In free boundary mode, a current distribution is defined and the magnetic field generated by that current distribution is calculated from it. The equilibrium pressure profile is then derived.

VMEC outputs an equilibrium in terms of cylindrical coordinates,  $R$ ,  $\varphi$  and  $Z$ , which are then mapped to PEST coordinates,  $s$ ,  $\theta$  and  $\varphi$ . This mapping is performed by a third separate code, the VM2MAG code.

### 3.8 Cancellation problem and mitigation

The cancellation problem is a numerical inaccuracy that arises from the choice of coordinate system in which to solve the gyrokinetic system of equations.

In the conventional  $p_{\parallel}$  formulation of the equations described in the previous section, the problem can be seen in Ampère's law,

$$\left( \sum_{s=i,e,f} \frac{\hat{\beta}_s}{\rho_s^2} - \nabla_{\perp}^2 \right) A_{\parallel} = \mu_0 \sum_{s=i,e,f} j_{\parallel 1s}. \quad (3.46)$$

The left-most terms in this equation, the electron and ion skin terms, are unphysical and arise only because of the co-ordinate system. In the  $v_{\parallel}$  formulation, they are not present. Problematically, in electromagnetic simulations these terms can be very large. One can see that these terms increase in size with  $n$  and  $T$  and with decreasing  $m_e$ . They are therefore especially significant when modelling electrons in a high  $\beta$  plasma.

In this case, the unphysical skin terms can become much larger than the field quantity,  $-\nabla_{\perp}^2 A_{\parallel}$ , that we wish to calculate. In principle, the adiabatic part of the perturbed gyrocentre current -  $j_{\parallel 1s}$  - should cancel this unphysical contribution exactly. In practice, there will always be numerical error which will therefore be amplified by this cancellation problem in the calculation of the desired physical quantity.

Mathematically, we can posit an adiabatic part of the distribution function, responding to  $A_{\parallel}$ ,

$$f_{1s}^{ad} = -\frac{ev_{\parallel} F_{0s}}{k_B T_s} A_{\parallel}, \quad f_{1s} = f_{1s}^{ad} + f_{1s}^{non-ad}. \quad (3.47)$$

This implies that

$$\frac{\beta_s}{\rho_s^2} A_{\parallel} = \frac{\mu_0 n_0 q^2}{m_s} A_{\parallel} = -\mu_0 q \int d^6 Z f_{1s}^{ad} v_{\parallel} \delta(\vec{R} - \vec{x}) = \mu_0 j_{\parallel 1s}^{ad} \quad (3.48)$$

and therefore

$$-\nabla_{\perp}^2 A_{\parallel} = \mu_0 \sum_{s=i,e,f} j_{\parallel 1s}^{non-ad}. \quad (3.49)$$

The cancellation problem scales with the size of the adiabatic current in relation to non-adiabatic current. The electron adiabatic current dominates due to the much lower

electron mass, so that the problem scales approximately with

$$\frac{j_{\parallel}}{j_{\parallel i} + j_{\parallel e}^{non-ad}} \propto \frac{\beta_e / \rho_e^2 A_{\parallel}}{\nabla_{\perp}^2 A_{\parallel}} \propto \frac{n_0 A_{\parallel}}{m_e \nabla_{\perp}^2 A_{\parallel}}, \quad (3.50)$$

so it can be seen at once that the problem scales with the electron density,  $n_0$ , and with  $1/k_{\perp}^2$ . The ‘MHD-limit’, where  $k_{\perp} \rho_i \rightarrow 0$ , is therefore particularly challenging. This regime is important for simulating Alfvén eigenmodes, which often have low  $k_{\perp}$ , and for non-linear electromagnetic simulations of all kinds, where the zonal mode ( $k_{\perp} = 0$ ) is often important.

In general,  $k_{\perp}$  is also a function of radial position. Taking the relation for a cylinder,

$$\frac{1}{k_{\perp}^2} = \frac{R_a^2}{\left(\frac{m}{r/R_a}\right)^2 + \pi^2} \quad (3.51)$$

where  $m$  is the poloidal mode number and  $R_a$  is the minor radius, we can see that the cancellation problem is most severe for  $m = 0$  and, for lower mode numbers, more severe closer to the edge of the device [100].

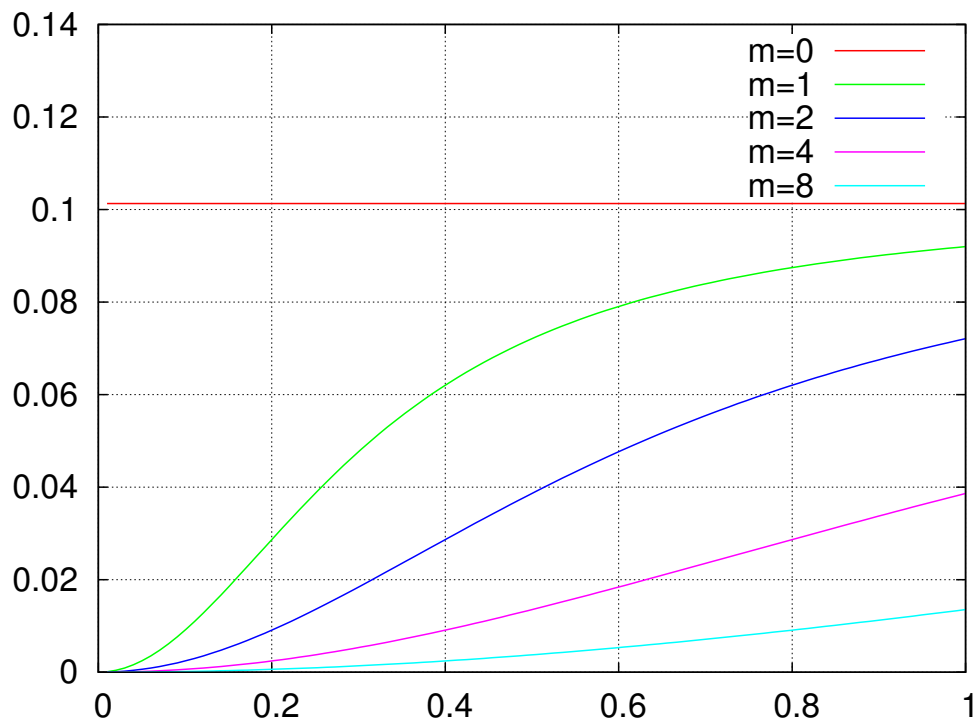


Figure 3.4: The severity of the cancellation problem depends upon the mode number and radial position of the mode. Depicted here for a cylindrical configuration [100].

Although here the cancellation problem has so far been discussed in relation to Ampère’s law, it is also present in the quasi-neutrality equation. Splitting this equation into adiabatic and non-adiabatic parts, we again see that there is an adiabatic

contribution, this time in the polarisation density,

$$n_e^{ad} = \int d^6 Z \delta(\vec{R} - \vec{x}) \frac{ev_{\parallel} e F_{0e}}{k_B T_e} A_{\parallel} \quad (3.52)$$

This contribution has to ‘cancel with zero’. It therefore does not exhibit the same pathological scalings of the Ampère’s law cancellation problem, but does scale with  $\sqrt{\beta}/m_e$  and it in any case still presents a problem of high noise to signal ratio in the presence of statistical error.

### 3.8.1 Adjustable control variate scheme

A control variate scheme is a generic approach to noise reduction in Monte Carlo simulation. It exploits correlation between a known quantity and a modelled quantity in order to reduce error in calculating other, unknown quantities.

The delta-f method is already a control variate scheme, in which the known Maxwellian background is used to reduce error in calculating the perturbation to that background. Where the perturbation of the background is small, the delta-f method is very powerful; without it, simulations of the linear stage of instabilities, where the perturbation of interest is many orders of magnitude smaller than the background, would be prohibitively computationally demanding. Depending on the saturation level, this consideration may also apply to non-linear simulations.

A control variate scheme is implemented in EUTERPE to mitigate the cancellation problem. [101, 102] Let there be two functions,  $X$  and  $Y$ , which yield unknown and known values respectively. If the expected value of  $X$  then is  $a$ , and  $Y$  is  $b$ , the expected value of

$$Z = X + c(Y - b) \quad (3.53)$$

is also  $a$ . The variance of  $Z$ , then, is

$$\text{Var}(Z) = \text{Var}(X) + c^2 \text{Var}(Y) + 2c \text{Cov}(X, Y). \quad (3.54)$$

The choice of  $c$  that minimises this variance is

$$c_{min} = -\frac{\text{Cov}(X, Y)}{\text{Var}(Y)}, \quad (3.55)$$

giving a variance of the value estimated by the new function that is lower than that of the original,

$$\text{Var}(Z) = \text{Var}(X) - \frac{|\text{Cov}(X, Y)|^2}{\text{Var}(Y)} = (1 - \text{Cor}(X, Y)^2) \text{Var}(X). \quad (3.56)$$

The degree of reduction in variance therefore depends upon the correlation between the desired unknown quantity and the known control quantity.

We define  $X - cY$  above by introducing a new population of ‘non-adiabatic’ weight,

$$\bar{w}_{pe} = \Omega_{pe} (f_{1e} - f_{\parallel 1e}^{ad}) = \tilde{w}_{pe} + \Omega \frac{ev_{\parallel} F_{0e}}{k_B T_e} A_{\parallel}, \quad (3.57)$$

however we do not know  $A_{\parallel}$ .

On the B-spline basis, Ampère's law can be written,

$$(L + S_i + S_e)\vec{c} = \mu_0 J_{\parallel i} + \mu_0 J_{\parallel e} - J_{\parallel e}^{ad}\vec{c} + S_e\vec{c} \quad (3.58)$$

where  $L$  is the Laplacian matrix,  $S_s$  are the skin terms,  $J_{\parallel e}^{ad}\vec{c}$  is the adiabatic part of the numerically calculated electron current, and  $\vec{c}$  is the B-spline coefficient vector corresponding to a  $a_{\nu}$  where  $A_{\parallel}(\vec{x}) = \sum_{\nu} a_{\nu} \Lambda_{\nu}(\vec{x})$ . Note that here the currents  $J_{\parallel 1s}$  differ from the currents defined earlier in terms of markers in that they have been interpolated onto the B-spline grid. On the right hand side, the non-adiabatic part of the current has been expressed in terms of the total current and the adiabatic part.

It is then possible to cancel the skin terms on both sides of the equation, removing the cancellation problem analytically, to yield,

$$(L + S_i + J_{\parallel e}^{ad})\vec{c} = \mu_0 J_{\parallel i} + \mu_0 J_{\parallel e} \quad (3.59)$$

Solving for  $\vec{c}$  yields  $A_{\parallel}$ .

This vector is calculated in the code using an iterative method, with subsequent iterations calculating progressively more terms in a series solution,  $\vec{c} = \sum_n \vec{c}^{(n)}$ .

The initial value of the vector is calculated by,

$$\vec{c}^{(0)} = \mu_0 (L + S_e + S_i)^{-1} (J_{\parallel 1i} + J_{\parallel 1e}). \quad (3.60)$$

At each subsequent iteration the approximation is refined by the calculation of further terms,

$$\vec{c}^{(n+1)} = (L + S_e + S_i)^{-1} [(S_e - J_{\parallel 1e}^{ad}) \vec{c}^{(n)}]. \quad (3.61)$$

Note that all of the quantities here are either calculated as time-independent matrices, i.e. they need to be calculated only once in the entire simulation, or they are acquired via the charge and current interpolation which must be performed anyway. The iterative scheme is therefore computationally efficient. In the simulations presented in this thesis, four iterations will be used for gyrokinetic simulations, which will all use the control variate scheme.

Although in principle this method solves the cancellation problem analytically, it can be shown that the problem still exists in practice in the EUTERPE code [80, 81], albeit strongly mitigated. Depending on the particular numerical properties of a given set of parameters, it would appear that the iterative scheme does not necessarily converge. In this case, large error can still be present in the calculation of  $A_{\parallel}$  in practice. The minimum criterion for convergence is that the difference between the analytical skin term and the adiabatic current term be small relative to the other terms,

$$|(S_e - J_{\parallel 1e}^{ad}) / (L + S_e + S_i)| < 1 \quad (3.62)$$

This imperfect mitigation has provided the impetus for further developments to minimise this problem, which are used in tandem with the iterative control variate scheme described here. These methods will be considered in the following section, and centre on the development of the mixed variables formulation of the equations of motion already described in section 2.1.5

### 3.8.2 Mixed variables scheme

The cancellation problem described above can be eliminated by choosing the  $v_{\parallel}$  formulation of the gyrokinetic equations. Unfortunately this introduces a new problem: the equations contain a nested time derivative,  $\partial \langle A_{\parallel} \rangle / \partial t$ , which is numerically difficult to solve [103]:

$$\dot{\vec{R}} = v_{\parallel} \tilde{\vec{b}}^* + \frac{1}{q_s \tilde{B}_{\parallel}^*} \vec{b} \times \left[ \mu \nabla B + q_s \left( \nabla \langle \phi \rangle + \frac{\partial \langle A_{\parallel} \rangle}{\partial t} \vec{b} \right) \right], \quad (3.63)$$

$$\dot{v}_{\parallel} = -\frac{1}{m_s} \tilde{\vec{b}}^* \cdot \mu \nabla B - \frac{q_s}{m_s} \left( \tilde{\vec{b}}^* \cdot \nabla \langle \phi \rangle + \frac{\partial \langle A_{\parallel} \rangle}{\partial t} \right). \quad (3.64)$$

It is, however, possible to make a choice of co-ordinates that intelligently minimises the cancellation problem without having to solve this nested time derivative, the mixed variables formulation described in section 2.1.5, with the following equations of motion,

$$\dot{\vec{R}}^{(1)} = \frac{\vec{b}}{B_{\parallel}^*} \times \nabla \langle \phi - v_{\parallel} A_{\parallel}^{(s)} - v_{\parallel} A_{\parallel}^{(h)} \rangle - \frac{q}{m} \langle A_{\parallel}^{(h)} \rangle \vec{b}^* \quad (3.65)$$

$$\dot{v}_{\parallel}^{(1)} = -\frac{q}{m} \left[ \tilde{\vec{b}}^* \cdot \nabla \langle \phi - v_{\parallel} A_{\parallel}^{(h)} \rangle + \frac{\partial \langle A_{\parallel}^{(s)} \rangle}{\partial t} \right] - \frac{\mu}{m} \frac{\vec{b} \times \nabla B}{B_{\parallel}^*} \cdot \nabla \langle A_{\parallel}^{(s)} \rangle, \quad (3.66)$$

Returning to equation 3.46, we see that we retain both the unphysical skin terms, and the undesirable nested time derivative. However, note that in the derivation of these equations the distribution of  $A_{\parallel}$  into  $A_{\parallel}^{(s)}$  and  $A_{\parallel}^{(h)}$  is arbitrary. Because we can distribute  $A_{\parallel}$  between  $A_{\parallel}^{(h)}$  and  $A_{\parallel}^{(s)}$  arbitrarily, we can gain an additional degree of freedom. We can posit an equation for  $A_{\parallel}^{(s)}$  so as to eliminate the time derivative and minimise the skin terms.

One sensible idea for such an equation would be to take the form of the ideal MHD Ohm's law, which will closely approximate the total  $A_{\parallel}$  by  $A_{\parallel}^{(s)}$  in many cases where ideal MHD is applicable. As in the fluid system of equations, then,

$$\frac{\partial A_{\parallel}^{(s)}}{\partial t} + \vec{b} \cdot \nabla \phi = 0. \quad (3.67)$$

Substituting this into the equations of motion, we obtain,

$$\dot{\vec{R}}^{(1)} = \frac{\vec{b}}{B_{\parallel}^*} \times \nabla \langle \phi - v_{\parallel} A_{\parallel}^{(s)} - v_{\parallel} A_{\parallel}^{(h)} \rangle - \frac{q}{m} \langle A_{\parallel}^{(h)} \rangle \vec{b}^* \quad (3.68)$$

$$\dot{v}_{\parallel}^{(1)} = -\frac{q}{m} \left[ \frac{m v_{\parallel}}{q} (\nabla \times \vec{b}) \cdot \nabla \langle \phi - v_{\parallel} A_{\parallel}^{(h)} \rangle \right] - \frac{\mu}{m} \frac{\vec{b} \times \nabla B}{B_{\parallel}^*} \cdot \nabla \langle A_{\parallel}^{(s)} \rangle, \quad (3.69)$$

eliminating the time derivative and further simplifying the remaining term.



This equation moreover provides a good physical ‘guess’ for the total magnetic potential in certain circumstances, particularly when simulating ideal MHD modes. This equation is not an approximation and does not truncate the physical content of the model, but while it is a good guess for the total magnetic potential and skin terms, multiplied by  $A_{\parallel}^{(h)}$  remain small. In practice, the skin terms can be diminished by several orders of magnitude when simulating, for instance, TAE.

As explained in section 2.1, the distribution function is modified in general when the equations are transformed into a new coordinate system. The mixed-variables densities and currents therefore do not necessarily correspond to the physical densities and currents. The physical (symplectic) distribution function is related to the mixed-variables distribution function by the equation

$$f_{1s}^{(s)} = f_{1s}^{(m)} + \frac{q_s \langle A_{\parallel}^{(h)} \rangle}{m_s} \frac{\partial F_{0s}}{\partial v_{\parallel}}. \quad (3.70)$$

Furthermore the gyrokinetic parallel velocity variable,  $v_{\parallel}$ , which in the  $v_{\parallel}$  formulation (symplectic formulation) is the physical  $v_{\parallel}$  and in the  $p_{\parallel}$  formulation (Hamiltonian formulation) is the canonical momentum, takes the form

$$v_{\parallel}^{(m)} = v_{\parallel}^{(gc)} + \frac{\vec{b}^*}{B} \cdot \nabla \left[ \int^{\theta_{(gc)}} (\phi - \langle \phi \rangle) d\theta_{(gc)} \right] + \frac{e}{m} A_{\parallel}^{(h)} + \frac{e}{m} \tilde{A}_{\parallel}^{(s)}, \quad (3.71)$$

$$\tilde{A}_{\parallel}^{(s)} = A_{\parallel}^{(s)} - \langle A_{\parallel}^{(s)} \rangle \quad (3.72)$$

in the mixed-variables formulation. Here  $v_{\parallel}^{(gc)}$  is the perturbed guiding centre velocity.

At each time step, then, we can reassign the magnetic potential such that  $A_{\parallel(k+1)}^{(s)} = A_{\parallel(k)}$ , noting that for consistency we must then adjust the distribution function to correspond to these new potentials. The following operation is performed,

$$f_{1s(k+1)}^{(m)} = f_{1s(k)}^{(s)} = f_{1s(k)}^{(m)} + \frac{q_s \langle A_{\parallel}^{(h)} \rangle}{m_s} \frac{\partial F_{0s}}{\partial v_{\parallel}} \quad (3.73)$$

where  $k$  is the current time step.

The mixed-variables scheme has benchmarked against existing linear gyrokinetic cases, and has been shown to reproduce the existing linear results in all cases, potentially greatly reducing the resolution requirement, depending on the severity of the cancellation problem in each case. In cases where the cancellation problem is particularly severe, such as the simulation of ITG in stellarator geometry or the most extreme cases in the  $k_{\perp} \rightarrow 0$  regime, such as low harmonic TAE modes, the mixed-variables scheme permits simulations that were otherwise impossible.

This scheme is valid in the linear regime. In the non-linear regime, however, it has been shown that there is a small quantitative disagreement between the  $p_{\parallel}$  and mixed variables schemes in some cases, as the equations thus far presented are consistently ordered only in the linear regime.

A complete non-linear scheme has been derived and will be published in [104], which includes some algebraically complicated but usually quantitatively small corrections to the equations of motion. These non-linear terms are yet to be implemented

in EUTERPE, and in this work these equations have not been used, however their implementation is shortly to be expected. It is not expected that the difference is qualitatively significant. This question will be investigated in future work.

### 3.9 Hybrid models

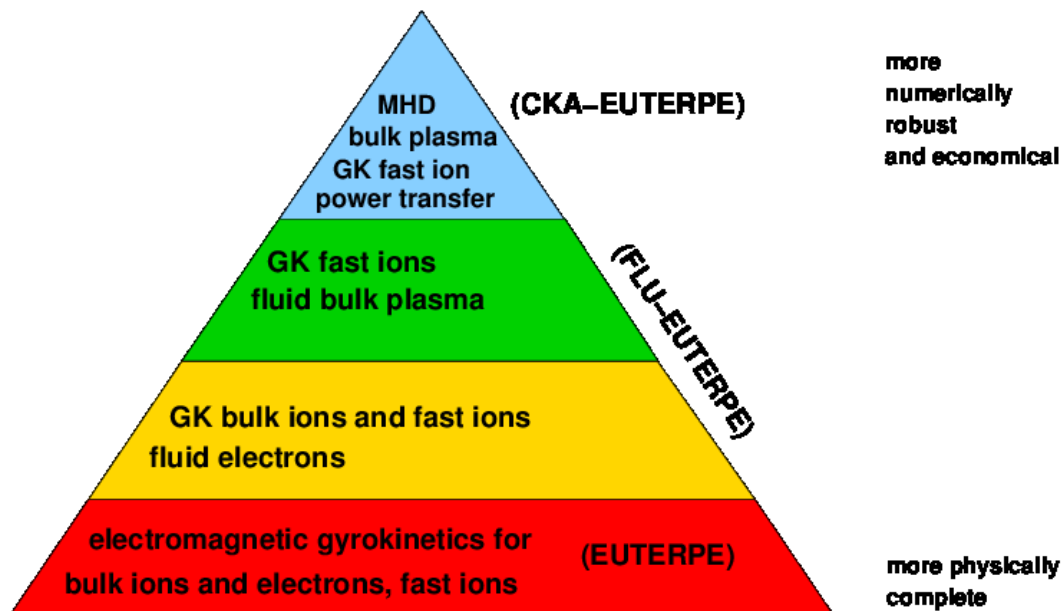


Figure 3.5: A depiction of the hierarchy of models included in the EUTERPE code package. The less physically complete models generally require fewer CPU-hours for a given simulation time, and encounter fewer difficulties with complex geometries.

The major work of this thesis concerns the development and exploitation of the two intermediate models, labelled together FLU-EUTERPE, which self-consistently solve for the gyrokinetic evolution of a population of thermal or fast ions, or both, in the presence of perturbed fields. The most complete couples a gyrokinetic description of the thermal ions and a fast particle species with a fluid description of the thermal electrons. The second model self-consistently couples a one-fluid description of the thermal plasma with a gyrokinetic description of a species of fast particles. These two models will be detailed in this section.

EUTERPE contains two non-perturbative models, FLU-EUTERPE, and one perturbative hybrid model, CKA-EUTERPE. A perturbative model is one in which the structure of the perturbed potentials does not evolve in response to a gyrokinetic species. Within the two non-perturbative hybrid models, the physical content can be altered further by considering, e.g. different fluid closures; this will be developed and detailed later.

In figure 3.5, the properties of these four basic models are depicted. At the bottom of the pyramid is the fully gyrokinetic EUTERPE detailed in the previous section.

Model	Self-consistent	GK $f$	GK $i$	GK $e$	$E_{\parallel}$	Canc. problem
CKA-EUTERPE	No	Yes	No	No	No	No
Fluid bulk plasma	Yes	Yes	No	No	No	No
Fluid-electron hybrid	Yes	Yes	Yes	No	No	No
EUTERPE	Yes	Yes	Yes	Yes	Yes	Yes

Table 3.1: A table of comparison for the various models included in EUTERPE. Self-consistency refers to the perturbed fields’ ability to react to the influence of kinetic species present.  $E_{\parallel}$  refers to the absence of fluid truncation in the Ohm’s law.

This is the most physically complete, but also the most computationally demanding and complex model, and the only one in which the cancellation problem is present.

At the top of the pyramid, CKA-EUTERPE is the sole perturbative hybrid model included in the EUTERPE code package. CKA-EUTERPE reads in a mode structure in perturbed  $\phi$  and  $A_{\parallel}$  from the reduced ideal MHD eigenvalue code CKA. These prescribed perturbed fields are then applied to the gyrokinetic solver detailed previously to calculate the particle orbits of an energetic particle population [51].

The main differences between the models are depicted in table 3.1. Physically, the principal omissions involved in the simplification of the plasma model are the omission of kinetic effects such as Landau damping and gyroscale effects for some or all species, the omission of finite  $E_{\parallel}$  effects such as resistivity and electron inertia, and the assumption of negligible modification of the reduced ideal MHD mode structure by any other mechanism.

Both FLU-EUTERPE non-perturbative hybrid schemes employ the  $v_{\parallel}$  equations of motion set out in section 2.1.3, in which there are no electron skin terms in Ampère’s law and hence the cancellation problem is not present. The time derivative of  $A_{\parallel}$  is eliminated by a fluid closure. The control variate scheme is therefore neither required nor used with the perturbative hybrid schemes. The intrinsic absence of the cancellation problem is a major advantage of the hybrid approach, eliminating the strong dependence of numerical stability upon  $k_{\perp}\rho_i$ . The hybrid models are therefore especially well suited for simulating kinetic interactions with MHD modes.

### 3.9.1 Numerical scheme

The general numerical scheme for the fluid hybrid models is concisely outlined below. The fluid equations to be solved will be recapitulated briefly and set in context of their place in the numerical scheme. The full set of equations and their derivation are set out in section 2.2.

1. Initial conditions are defined: initial distribution functions,  $f_{s(k)}$  are required for any gyrokinetic species that may be present, and initial conditions for the fluid density,  $\rho_{1(k)}$  or  $n_{1e(k)}$ , the parallel magnetic potential,  $A_{\parallel}$ , and the perturbed pressure,  $P_1$  or  $P_{1e}$ , are also required.

2. Taking the distribution functions of the gyrokinetic species, moments are calculated to yield the perturbed current and density contributions for those species,  $n_{1(i,f)(k)}$  and  $j_{\parallel 1(i,f)(k)}$ .
3. The perturbed parallel electrostatic potential is calculated from the perturbed densities using the quasineutrality equation. In the fluid bulk plasma model, this takes the form,

$$-\nabla_{\perp} \frac{m_i n_0}{B^2} \nabla_{\perp} \phi_{(k)} = \rho_{1(k)} \quad (3.74)$$

Meanwhile the quasi-neutrality equation couples the fluid electrons discretised by B-splines on the grid to the thermal ions discretised by markers in the case where they are simulated gyrokinetically,

$$-\nabla_{\perp} \frac{m_i n_0}{B^2} \nabla_{\perp} \phi_{(k)} = e n_{1i(k)} - e n_{1e(k)}. \quad (3.75)$$

4. The perturbed parallel magnetic potential is calculated from the perturbed electrostatic potential from Ohm's law,

$$A_{\parallel(k+1)} = f(\phi_{(k)}) \quad (3.76)$$

5. The perturbed fluid parallel velocity is calculated from the currents using Ampère's law. In the fluid bulk plasma mode this equation is,

$$u_{\parallel 1e(k+1)} = \frac{1}{\mu_0 |e| n_0} \nabla_{\perp}^2 A_{\parallel(k+1)} \quad (3.77)$$

Ampère's law couples the fluid electrons discretised on the grid to the thermal ions discretised by markers in the case where they are simulated gyrokinetically,

$$u_{\parallel 1e(k+1)} = \frac{1}{\mu_0 e n_0} \left( \nabla_{\perp}^2 A_{\parallel(k+1)} - \mu_0 j_{\parallel 1i(k+1)} \right), \quad (3.78)$$

as the perturbed ion current is represented by markers while the perturbed parallel electron velocity, like the perturbed parallel magnetic potential, is represented as a field on the grid.

6. The perturbed pressure is then calculated using the pressure truncation,

$$P_{1e(k+1)} = f(P_{1e(k)}, P_0). \quad (3.79)$$

7. The perturbed fluid density is then calculated at the next time step using the continuity equation,

$$n_{(k+1)} = f(u_{\parallel(k)}, A_{\parallel(k)}, \phi_{(k)}, P_k). \quad (3.80)$$

If present, the perturbed GK distribution functions are calculated by solving the gyrokinetic equation(s).

Steps 2.-7. are then iterated.

The output quantities are the distribution functions for all gyrokinetic species, from which moments can be calculated, the zeroth, first, and second moments of the fluid species (perturbed density, current and pressure), and the perturbed fields. Higher order fluid moments are not considered.

## 3.10 Diagnostics

In this section the most common diagnostics that will be used in presenting the results will be described and explained. In the following section, outputs from the various diagnostics will be shown.

- **Radial mode structure, poloidal decomposition** - The amplitudes of the perturbed electrostatic and magnetic potentials are plotted, Fourier decomposed into poloidal harmonics, at each radial plot. This diagnostic is particularly suited to axisymmetric geometries in which the mode structure is unchanged toroidally and in which typically only a single toroidal mode number is considered. Where multiple toroidal modes are important, this diagnostic may be less appropriate. The perturbation amplitude is taken only at the single toroidal slice where  $\varphi = 0$ .
- **Mode structure in poloidal cross-section** - The amplitudes of the perturbed electrostatic and magnetic potentials are plotted at each radial and poloidal position in a cross-section through the device taken at a defined toroidal position,  $\varphi = 0$ . This diagnostic presents essentially the same information as the previous but in a different visual form. This form can be more useful if one is interested in the collective form of multiple poloidal harmonics.
- **Linear growth rate and frequency** - A function is numerically fitted to the evolution of the amplitudes of the perturbed electrostatic or magnetic potential decomposed poloidally, to estimate the growth rate and frequency of the evolution of each poloidal harmonic, assuming a form,

$$\phi(t) = \cos(\omega t)e^{\gamma t} \quad (3.81)$$

- **Power spectrum diagnostic** - The amplitude of the electrostatic and magnetic potential integrated in the radial direction is plotted for each combination of poloidal and toroidal mode number. This diagnostic is important for determining whether the system is being truncated by the chosen filter. It also shows whether a single or multiple distinct modes are present in the system.
- **Magnetic field perturbation** - A maximum of the perturbed magnetic field as a ratio of the equilibrium magnetic field,

$$\epsilon_{\Delta} = \delta B/B_0 \quad (3.82)$$

is taken over all radial, poloidal and toroidal points. A time series can then be plotted. This diagnostic is particularly important for non-linear simulations, where it shows the time of onset of the non-linear phase and the saturated perturbed magnetic field amplitude.

- **Frequency spectrum** - The amplitude of the perturbed electrostatic or magnetic potential is plotted in frequency bins over a time series. In linear simulations, typically the mode is well localised in frequency. In the saturated phase of non-linear simulations, this diagnostic yields important information about the behaviour of the system, such as the presence of frequency chirping.

- **Power transfer** The power transfer is calculated by

$$\frac{dW}{dt} = \vec{J} \cdot \vec{E} \quad (3.83)$$

for particles at each position in the phase space  $v_{\parallel}, v_{\perp}$ . The power transfer for each individual marker is then summed over many markers within energy and pitch angle bins. This diagnostic shows at which energy and pitch angle particles are resonant with a given mode. As

$$\vec{J} \cdot \vec{E} = q_s \left( v_{\parallel} E_{\parallel} + \vec{v}_d \cdot \vec{E} \right), \quad (3.84)$$

this diagnostic can also decompose the particular drifts responsible for driving or damping a mode.

# Chapter 4

## Linear simulations

In this chapter, the results of linear simulations with the EUTERPE code using all of the available models will be presented. Particular emphasis is placed upon validating the applicability of the numerical models available in as wide as possible circumstances. Limiting parameters include the electron  $\beta$  and density, and perpendicular wavenumber  $k_{\perp}\rho_i$ , with which the cancellation problem scales, and the complexity of the magnetic geometry particularly in 3D.

In this chapter, only the linearised gyrokinetic Vlasov equation,

$$\frac{\partial f_1}{\partial t} + \dot{\vec{R}}^{(0)} \cdot \frac{\partial f_1}{\partial \vec{R}} + v_{\parallel}^{(0)} \frac{\partial f_1}{\partial v_{\parallel}} = -\dot{\vec{R}}^{(1)} \cdot \frac{\partial F_0}{\partial \vec{R}} - v_{\parallel}^{(1)} \frac{\partial F_0}{\partial v_{\parallel}} \quad (4.1)$$

will be solved, where  $\dot{\vec{R}}^{(0)}$  and  $v_{\parallel}^{(0)}$  denote the gyrokinetic equations of motion in the relevant formulation neglecting those terms proportional to perturbations of the electrostatic and magnetic fields. The superscript 1 correspondingly denotes the terms in the equations of motion proportional to the perturbed fields.

First, the fluid-hybrid models will be benchmarked against the most challenging case investigated using the fully gyrokinetic code at the beginning of this work, a standard linear TAE benchmark case. Convergence scans will also be performed using all non-perturbative models, and the performance of the different models compared.

The limits of the fluid models will then be explored with a more complex TAE case based on this benchmark, in which ion and electron Landau damping, and finite  $E_{\parallel}$  effects are more pronounced. This case will help to delimit the range of applicability of the new models and give an idea where the physical truncations have relevance.

The extreme  $k_{\perp}\rho_i \rightarrow 0$  limit, and MHD current drive, will then be considered with simulations of the internal kink mode and the associated  $m = 1$  Energetic Particle Mode (EPM). As the cancellation problem is most pronounced in this case, it will be considered only using the hybrid models where the cancellation problem is not present.

Finally, proof of principle simulations of global modes in numerical stellarator equilibria will be presented using both gyrokinetic and hybrid models. Outstanding limitations with such simulations will be discussed and future work to address those issues will be outlined.

## 4.1 ITPA TAE benchmark

The International Tokamak Physics Activity (ITPA) Toroidal Alfvén Eigenmode benchmark is a useful verification tool for the new hybrid models of FLU-EUTERPE. It has been performed by many codes with a range of different numerical implementations, e.g. initial value and eigenvalue, and physical models, including full gyrokinetic, gyrofluid, and MHD-kinetic hybrid. [105] Most of these codes have been discussed in section 1.5.

The physical parameters chosen are a large aspect ratio tokamak with major radius,  $R_0 = 10.0$  m and minor radius,  $a = 1.0$  m. The magnetic field strength on-axis is 3.0 T. A low shear analytical safety factor profile is chosen with the form,

$$q(r) = 1.71 + 0.16(r/a)^2. \quad (4.2)$$

The bulk ion and electron temperature profiles are flat, with absolute values  $T_i = T_e = 1$  keV. The bulk ion density profile is flat with an absolute value of  $2 \times 10^{19} \text{ m}^{-3}$ .

The Alfvén continuum corresponding to the equilibrium parameters described above is depicted in figure 4.1. Note that, in this frequency range, there is a single gap associated with poloidal and toroidal harmonics  $n = -6$  and  $m = 10, 11$ .

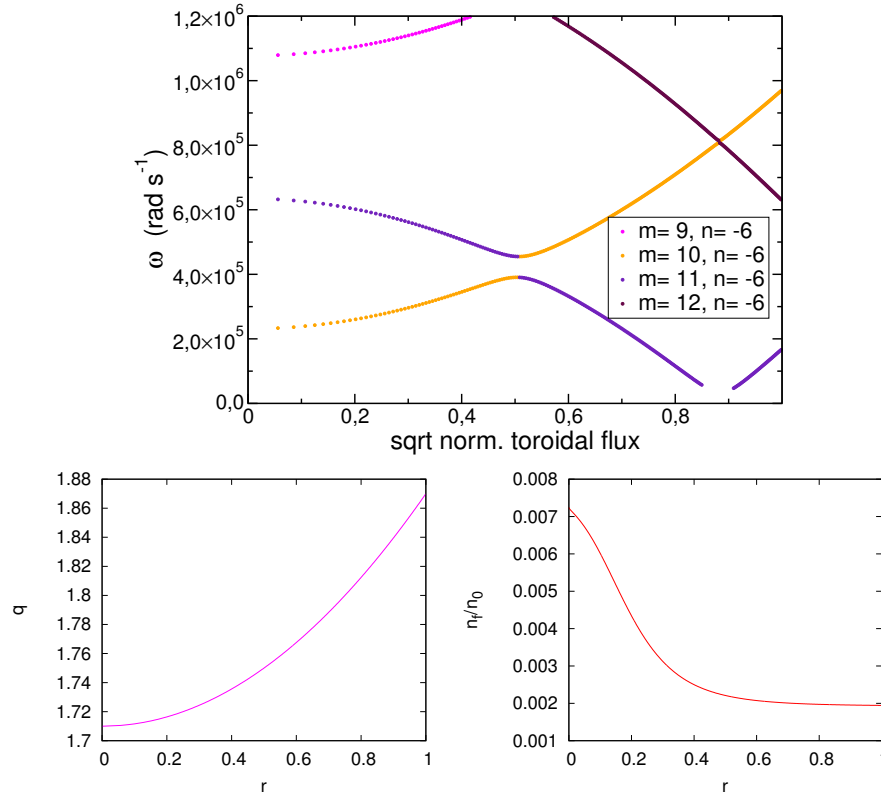


Figure 4.1: Above: the continuum for the ITPA TAE tokamak benchmark case. Below: the safety factor (left) and fast particle density profiles (right). Both in terms of  $r$ , where with circular flux surfaces  $s = r^2$ .

The benchmark naturally concerns itself with the TAE associated with this  $n = -6$ ,



$m = 10, 11$  gap. The mode is driven by a fast particle population of density  $n_{0f} = 7.5 \times 10^{16} \text{ m}^{-3}$  and profile,

$$n_f(r) = n_{0f} \exp\left(-\frac{2}{3} \tanh\left(\frac{r-0.5}{0.2}\right)\right). \quad (4.3)$$

The peak density gradient therefore coincides with the expected central location of the TAE, in the gap.

The distribution function is Maxwellian with a temperature varied up to 800keV. One limit to the numerical performance of different codes is how close to marginal stability they can simulate such modes. Self-consistent initial value codes are generally more problematic in this respect, as a weakly driven mode must be given time to form against an arbitrary initialised background. Such problems can be somewhat alleviated by careful consideration of the mode initialisation.

Numerically, each gyrokinetic species is discretised with  $N = 10^6$  markers. The number of grid points is  $n_s = 80$  in the radial direction,  $n_\chi = 64$  in the poloidal direction, and  $n_\phi = 1$  in the toroidal direction. Using the phase factor transform, the Fourier filter can be centred on the mode, at  $m = 10$ ,  $n = -6$ . Four lower and higher number poloidal harmonics are also included in the Fourier filter. As there is no toroidal coupling, no additional toroidal harmonics are considered. The fluid-electron hybrid fully gyrokinetic (mixed variables formulation) models are used; gyrokinetic bulk ion physics in the fluid formulation are not significant.

The two quantities for comparison in this benchmark are the mode frequency and the linear growth rate. The mode frequency is modified by the fast particle population, but a TAE should remain within the gap or it will become subject to continuum damping. A mode that resides outside the gap is generally an EPM, and would not exist without the presence of fast particles. An EPM is generally only possible at high fast particle  $\beta$  [106].

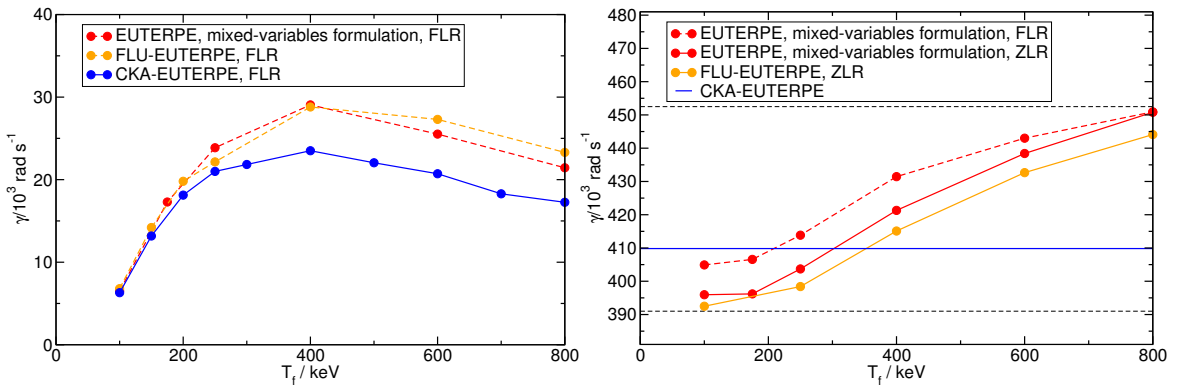


Figure 4.2: Growth rate (left) and frequency (right) of the ITPA TAE benchmark compared for three models of increasing completeness. Some divergence is seen between the perturbative and non-perturbative models, but both non-perturbative models yield almost identical results. The position of the Toroidicity gap is marked in black in the frequency plot.

The linear growth rate should increase with fast particle temperature until Finite Orbit Width (FOW) and Finite Larmor Radius (FLR) effects begin to damp the mode, as the fast particle Larmor radius becomes significant in comparison with the size of the device. This occurs as the orbit and FLR effects tend to average the potentials experienced by the particles over a greater part of the plasma volume, weakening the perceived gradients.

In figure 4.2 the mode frequency and linear growth rates are depicted for the four models included in the EUTERPE code package. The expected trends in frequency and linear growth rate are seen with all models and are consistent with a TAE mode that does not at any stage become an EPM.

Quantitatively, all four models show good agreement; the self-consistent hybrid and the fully gyrokinetic models in particular show almost exact agreement. There is some discrepancy in frequency between the fluid-electron hybrid and the fully gyrokinetic models. This will be a generic feature of the models, with the fluid-electron hybrid model consistently showing a somewhat lower frequency, except at very low levels of fast particle drive. In the fully gyrokinetic model, the inclusion of FLR effects causes an up-shift in frequency.

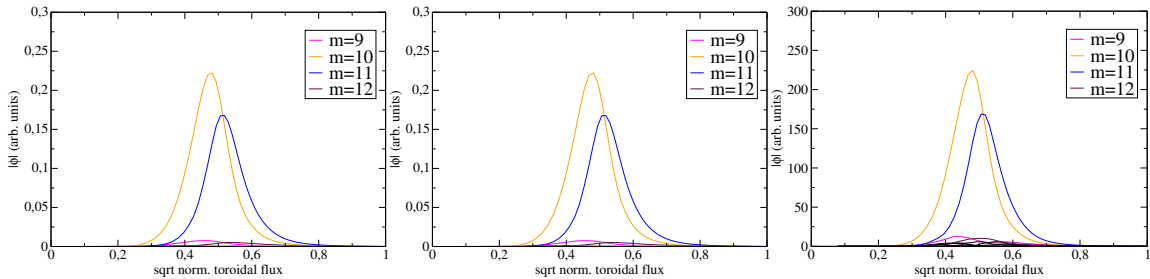


Figure 4.3: The mode structures calculated by, from left to right, CKA-EUTERPE, FLU-EUTERPE, and EUTERPE. All three models show close agreement, although the mode structure from the perturbative hybrid model CKA-EUTERPE is noticeably narrower. Note that it is calculated externally and fixed.

The mode structures are shown in figure 4.3. The mode structures calculated self-consistently by the fluid-electron hybrid model and the fully gyrokinetic model are almost identical in this case. The CKA-EUTERPE mode structure is calculated entirely by the reduced ideal MHD eigenvalue code CKA, and is somewhat narrower.

In figure 4.5, results for the linear growth rate from all codes included in the ITPA TAE benchmark are depicted along with those from the fluid-electron hybrid model and the fully gyrokinetic EUTERPE with mixed variables formulation of the equations of motion. One can see that all models show good qualitative agreement with the growth rate increasing with fast particle temperature up to a peak and then reducing as temperature continues to increase above about 500keV. Without FOW, this peak and decrease in growth rate with temperature does not occur. At lower fast particle temperatures, the growth rates returned by various codes are more tightly bunched.

All codes in the EUTERPE package return linear growth rate results that fall within the range of scatter exhibited by the other codes. The two non-perturbative models

return results that are clustered toward the high end of the range. There are numerous possible source of discrepancy between codes that may explain the spread in growth rates. For instance, in different codes the equilibrium is calculated differently. A circular axisymmetric equilibrium can, for instance, be calculated analytically. EUTERPE codes, however, use a numerical equilibrium. An additional generic source of discrepancy is that the codes may have used different resolutions. Different codes also have different discretisation schemes. About the mean value, the linear growth rate varies by about 25%.

The perturbative code CKA-EUTERPE returns linear growth rates close to the middle of the spread. It is possible, then, that mode structure and mode frequency modification may have some influence on the growth rate, as these mechanisms are absent in CKA-EUTERPE. Comparison of mode structures in figure 4.3, suggests that this may be due to the reduced width of the mode calculated by CKA, which reduces the radial domain over which the fast particle gradients can drive the mode. As the other perturbative code, NOVA-K, returns lower values, it may tentatively be suggested that perturbative codes consistently calculate lower growth rates than non-perturbative codes.

The ITPA benchmark activity itself was principally concerned with the change in the linear mode growth rate and frequency with changing fast particle temperature. Studies are additionally performed varying the fast particle density at fixed temperature. In figure 4.4, the results of these studies are presented. The growth rate increases linearly with the fast particle fraction, where a fast particle fraction of 1.0 corresponds to the nominal ITPA TAE case fast particle density. The frequency increases slightly with increasing fast particle fraction, but remains within the TAE gap.

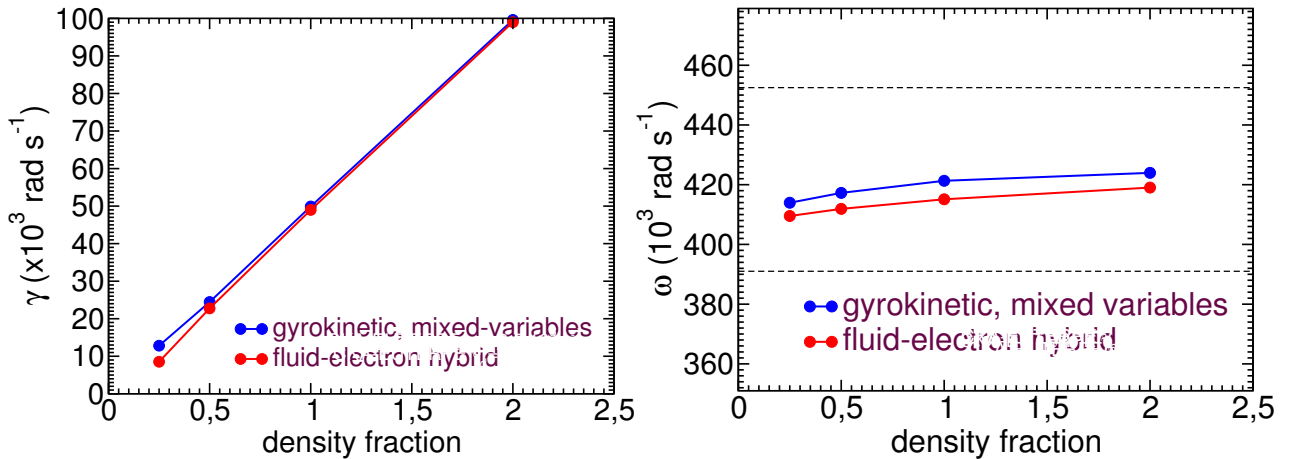


Figure 4.4: Growth rate (left) and frequency (right) of the ITPA TAE benchmark for the nominal parameters with  $T_f = 400\text{keV}$  and varying fast particle density expressed as a fraction of the nominal density, compared for the fully gyrokinetic (mixed variables) model and the fluid-electron hybrid model.

The ITPA benchmark credibly establishes the capability of the fluid-electron hybrid model and the fully gyrokinetic scheme with equations of motion in the mixed variables formulation to accurately treat the physics of linear Alfvén eigenmodes driven by fast

particles. The numerical parameters and computational requirements are discussed in greater detail in the following section.

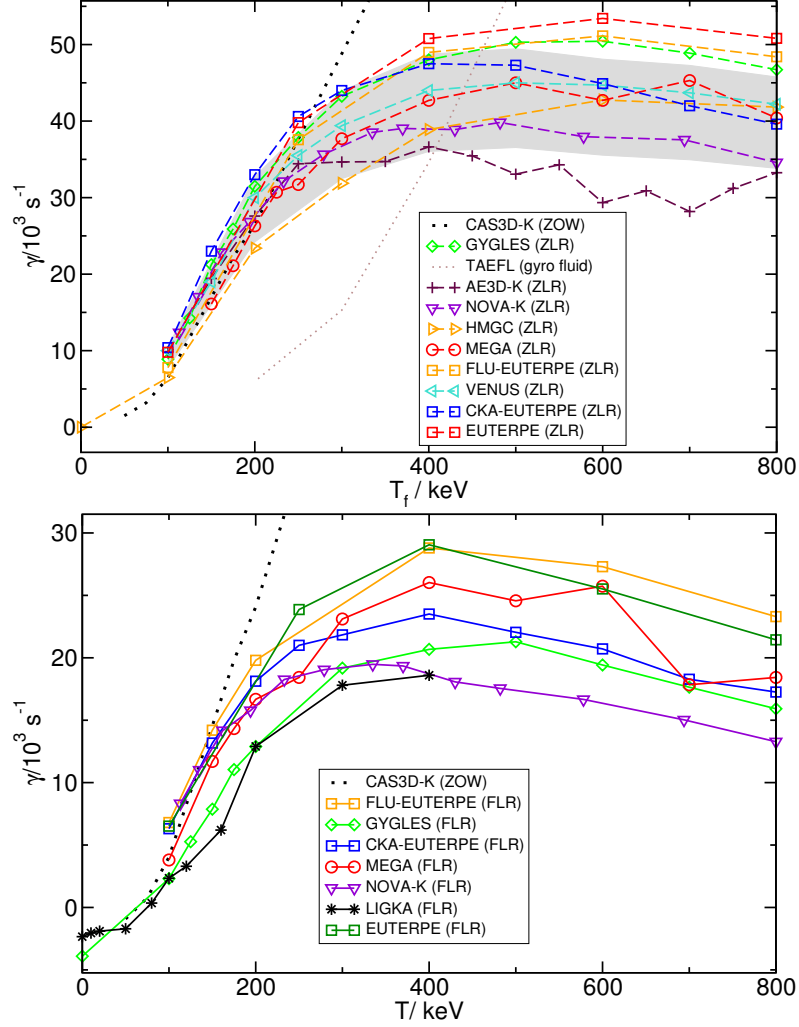


Figure 4.5: Comparison of the linear growth rate for the ITPA TAE benchmark case including all involved codes [105], the fluid-electron hybrid model FLU-EUTERPE, and the fully gyrokinetic EUTERPE with mixed variables scheme. The results are presented in the limit of zero Larmor radius (left) and with the physical finite Larmor radius considered (right).

## 4.2 Convergence studies and computational requirements

An important difference between the fully gyrokinetic and the fluid-electron hybrid models is the required numerical resolution, which is important in determining the computational requirements of each model. In this section the marker and grid resolution will be investigated using the ITPA TAE case. Although in general it is necessary

to perform convergence studies for each new case, the ITPA TAE case will illustrate some broad differences in performance between the two models.

First we consider the marker resolution required to converge on an accurate mode frequency and growth rate. We take the nominal ITPA parameters with  $T_f = 400$  keV. We take, as before, the number of radial grid points  $n_s = 80$ , poloidal grid points  $n_\chi = 64$  and toroidal grid points  $n_\phi = 1$ . Note that the number of markers per grid cell is also an important figure of merit, here being the number of markers divided by 5,120 total grid points.

In figure 4.6, the variation in frequency and linear growth rate is plotted. It can immediately be seen that the fluid model, which does not need the markers to resolve the mode itself, converges to the nominal value almost immediately with a low number of markers. The resolution in fast particles required to generate the correct growth rate and frequency modification is small. Note that, as in the previous section, there is a small discrepancy in the frequency predicted by the two models of about  $5 \times 10^3$  rad s<sup>-1</sup>.

This reduced marker resolution requirement is a significant contributor to the greater numerical efficiency of the hybrid models. In the fully gyrokinetic code, computational requirement in terms of CPU-hours is approximately proportional to the number of markers used, with some fixed overhead solving the matrix equations for the quasi-neutrality equation and Ampères law. In the fluid-electron hybrid model, this overhead is somewhat greater as matrix operations must furthermore be performed to solve the continuity equation. In cases such as here, this fixed overhead can be greater than the time taken to evolve the marker positions and weights with the required marker resolution; the duration of a timestep is therefore determined by the matrix equations and not the marker number.

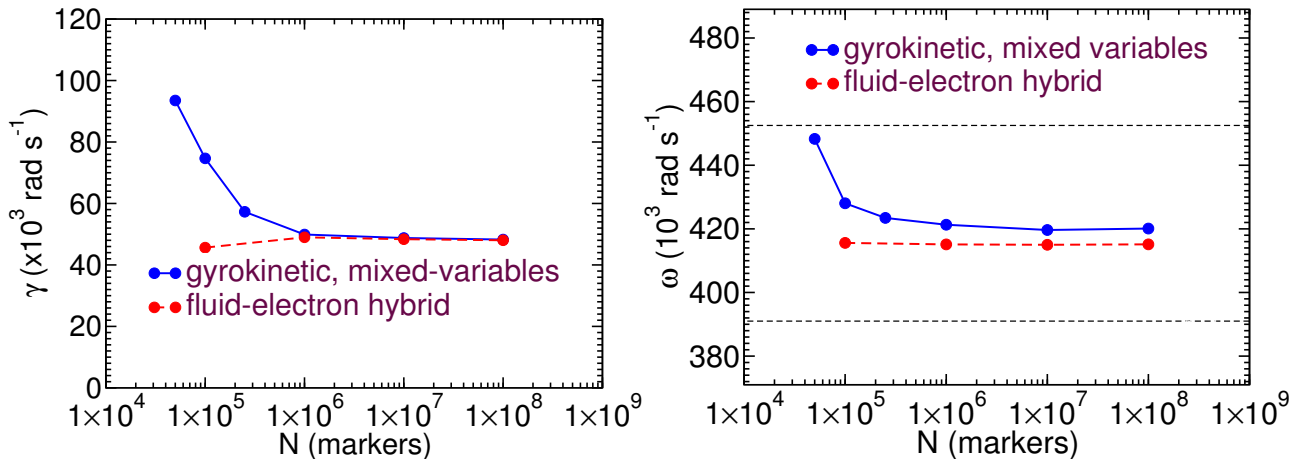


Figure 4.6: Growth rate (left) and frequency (right) for the ITPA TAE benchmark for the nominal parameters with  $T_f = 400$  keV. Only the number of markers is varied. Note the horizontal lines in the frequency plot indicating the position of the toroidicity gap.

Because solving matrix equations is generally proportionally more computationally demanding for the hybrid models than for the fully gyrokinetic model, changes in grid resolution are more significant for the performance of the code. This is because an

increase in the number of radial or poloidal grid points creates a requirement to solve larger matrix equations on every CPU.

Fortunately, a large number of grid points is often not necessary when considering long wavelength global modes. In figure 4.7, the ITPA TAE benchmark case is performed for fixed marker number  $10^6$  for all species with a varying radial resolution. One can see that with both models there is very little divergence in the calculated linear growth rate and frequency over a large range of values of radial resolution. At very high radial resolution there is an upward drift in the growth rate shown in the fully gyrokinetic model, possibly because of the reducing resolution in terms of markers per cell. Compare with figure 4.6 where reduced total marker number with fixed grid cell number shows an increase in measured growth rate.

In cases with more complex fine scale structure, there may be a stronger dependence on radial resolution, however in such cases the advantages of a global over a local (e.g. flux tube) approach may also be less. The fluid-electron hybrid model exhibits somewhat less variance in quantitative result with radial resolution than the fully gyrokinetic model.

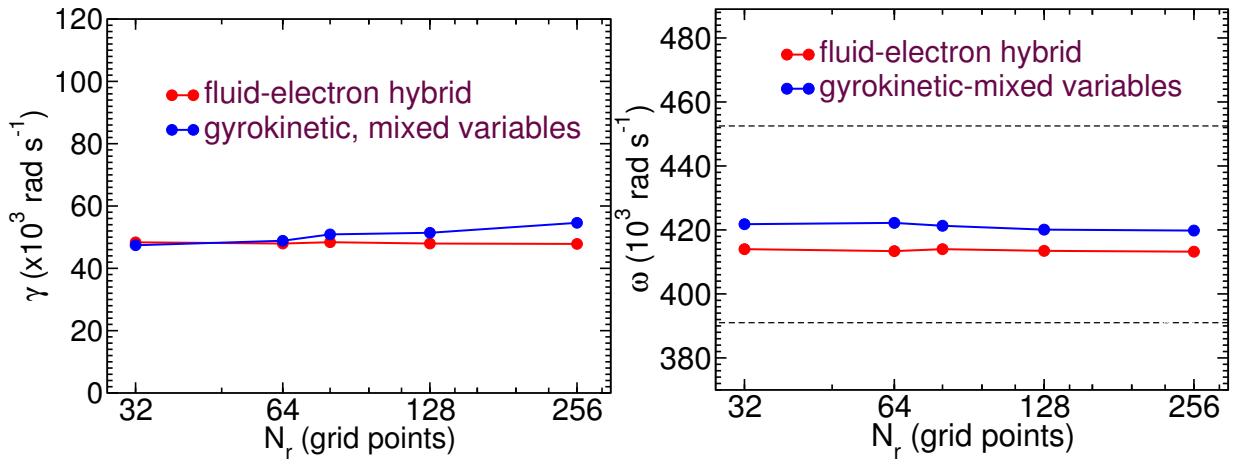


Figure 4.7: Growth rate (left) and frequency (right) for the ITPA TAE benchmark case for the nominal parameters with  $T_f = 400$  keV. Only the number of radial grid points is varied. The marker number here is fixed at  $10^6$ . The horizontal lines in the frequency plot once again indicate the position of the toroidicity gap.

The computational requirements of each model vary significantly. A simple comparison is shown in table 4.1, where the radial resolution  $s = 80$  is used in every case. One can see at once that the reduced models converge at much lower resolution. In this case the simpler models show a clear superiority over the more complete models, being physically sufficient and computationally inexpensive.

Considerations such as the differing degree to which different models are dependent upon matrix operations, which are parallelised only by domain decomposition of the grid, and marker operations, which are additionally parallelised within each domain by grid clones, can affect the optimally efficient numerical setup.

For instance, in a fluid-electron hybrid simulation dominated by the matrix solve time, it is more efficient in terms of CPU-hours to run the code on a number of CPUs

Model	Markers	Timestep	CPU-hours ( $10^5 \Omega_c^{-1}$ )
Fluid bulk plasma	$2 \times 10^5$	10.0	12.8
Fluid-electron hybrid	$2 \times 10^5$	10.0	18
EUTERPE ( $p_{\parallel}$ )	$3 \times 10^7$	0.75	79,076
EUTERPE (mixed)	$3 \times 10^6$	10.0	256

Table 4.1: A table depicting the computational requirements of each model for the ITPA TAE case with nominal parameters to reach an ‘end time’ of  $10^5 \Omega_c^{-1}$ , at which all the properties of interest of the mode are well established and can be diagnosed with good accuracy. Note that this time was not reached with any set of parameters for the fully gyrokinetic model in the  $p_{\parallel}$  formulation and the CPU-hour requirement is extrapolated assuming it would do so with the smallest number of markers and largest time step able to produce a diagnosable result.

equal to the number of decomposed domains. In a fully gyrokinetic simulation dominated by the time required to calculate marker quantities, the code scales very well with additional CPUs into the thousands or tens of thousands regardless of the number of decomposed domains [107].

It can be seen that the mixed variables formulation of the equations of motion dramatically increases the efficiency of fully gyrokinetic simulations. Not only is the minimum marker resolution reduced by an about an order of magnitude, but the workable timestep is increased by around an order of magnitude. The fully gyrokinetic treatment is nonetheless still around one order of magnitude more expensive than the fluid-electron hybrid approach.

Note that in the case of the fully gyrokinetic EUTERPE in the  $p_{\parallel}$  formulation, the simulations failed in all tested cases up to maximum  $10^8$  markers before reaching  $t = 100000 \Omega_c^{-1}$ . With  $10^6$  markers the simulation successfully reached  $t = 5000 \Omega_c^{-1}$  having simulated only one complete mode period. With  $10^7$  markers the simulation reached  $t = 16000 \Omega_c^{-1}$  and completed seven mode periods, while  $10^8$  markers showed no significant improvement over  $10^7$ .

This comparison therefore understates the improvement in performance of fully gyrokinetic simulations in this case due to the mixed variables formulation. This improvement will not be so large in cases where the cancellation problem is small, either for geometrical reasons or because of low electron  $\beta$ , and may not be large in cases where the evolution of the perturbed magnetic potential deviates significantly from that dictated by an ideal MHD Ohm’s law. The latter restriction may be possible to overcome by adapting the scheme [80].

### 4.3 TAE-continuum interaction

Having investigated a case in which all the models are broadly sufficient, it is interesting to proceed to cases where one or several of them break down. Building upon the well-understood ITPA benchmark case, it is possible to better differentiate the models with



only a small increase in physical complexity.

Keeping all other equilibrium parameters the same, we increase the magnetic shear such that the safety factor profile is now given by  $q(r) = 1.5 + (r/a)^2$ . This results in a significantly more complex continuum. The two continua are depicted in figure 4.8 [105, 68]. It should also be noted that the steeper safety factor profile is much closer to that seen in present-day tokamak experiments than that used for the ITPA benchmark.

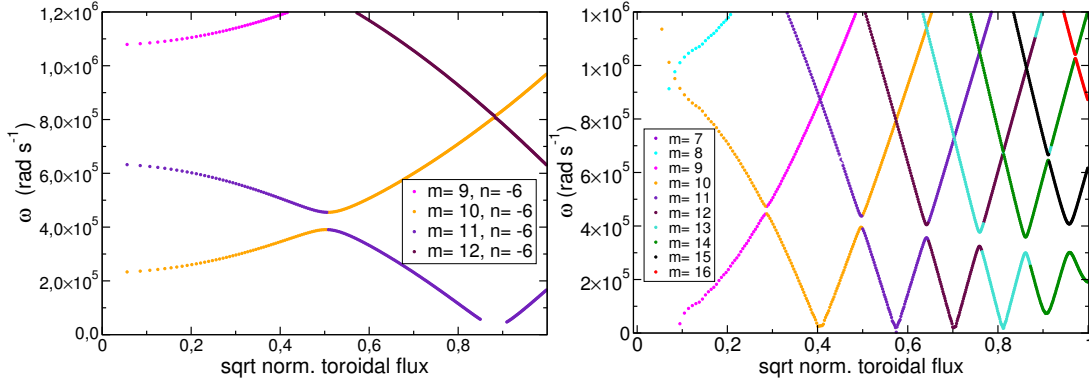


Figure 4.8: Continua compared: the ITPA TAE case (left) and the high shear case (right). Note that in the high shear case the gaps are spaced such that a global mode residing in one gap can touch the continuum at the radial position of the others [105, 68].

In addition to the safety factor profile, the background temperatures are also of importance. In this case, higher background temperature can increase the significance of Landau damping by the thermal plasma. Keeping all other bulk plasma parameters the same, the bulk temperature is increased to 9 keV. In this case, the mode frequency is also shifted upwards sufficiently that the mode begins to interact with the continuum. The fast particle parameters are the same as previously.

An important feature of this case is that a mode centred just below the central gap, where one would expect damping to be weakest and therefore the strongest growing mode to exist, will interact with the continuum via the other harmonics if it is sufficiently radially extended. This therefore leads to important continuum damping effects being present even for a gap mode, as discussed in section 1.3.2.

Considering the results, in this case there is a clear difference in observed mode structure for the three models. In figure 4.9, the calculated mode structures are depicted for the two fluid hybrid, and the fully gyrokinetic models [68, 84].

When the mode structure is calculated using the reduced ideal MHD bulk plasma model, and only the fast particle population is considered gyrokinetically, a series of six modes, each corresponding to one of the six continuum gaps, is seen. The addition of a gyrokinetic description of the thermal ions damps these modes. The  $n = 6$ ,  $m = -10, -11$  mode is least damped, and forms a global structure with coupling to side bands located at  $s = 0.3$  and  $s = 0.65$ , corresponding to the positions of the other TAEs. A fully gyrokinetic description does not significantly alter this mode structure, suggesting that the ion kinetic physics is decisive here.



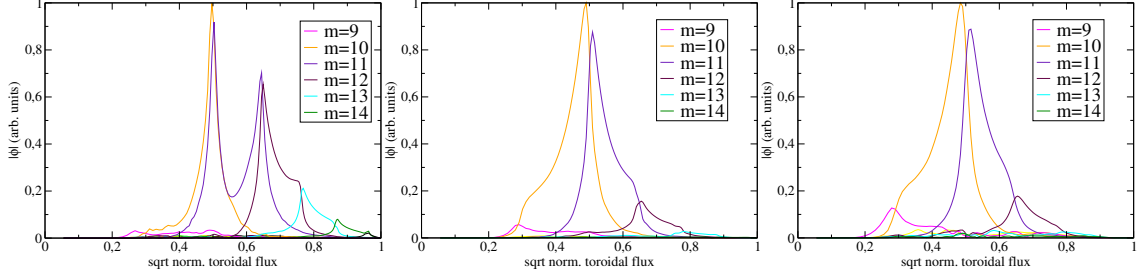


Figure 4.9: The mode structure calculated by, from left to right, the MHD-fast particle hybrid model, the fluid electron hybrid model, and the fully gyrokinetic model. Note the major change that occurs when thermal ion kinetics are considered. [84]

The quantitative frequency and linear growth rates may also be compared. In figure 4.10, the maximum growth rate in each case is depicted as the thermal temperature of the applied fast particle population is varied. It is first of all evident that the maximum growth rates calculated by the perturbative and non-perturbative fluid thermal plasma models are in close agreement with one another.

When gyrokinetic bulk ions are added to the model, the maximum growth rate increases, although the other modes are damped. A plausible explanation is that the other modes, which interact more strongly with the continuum, are damped while the  $m = -10, -11$  mode structure is broadened, increasing the effective proportion of the fast particle density gradient driving the mode. The fixed mode structure used in CKA-EUTERPE does not experience this broadening.

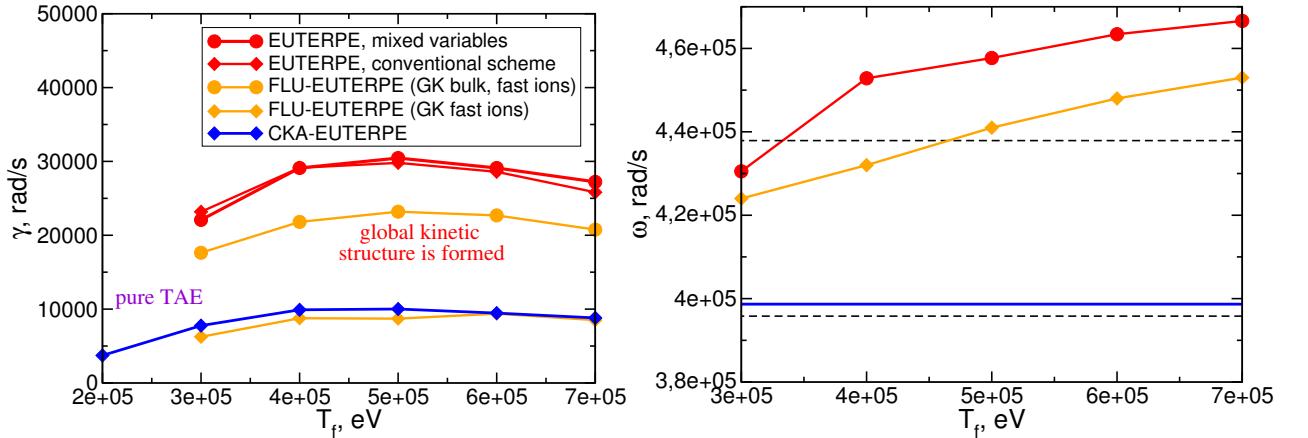


Figure 4.10: Comparison of the linear growth rate (left) and frequency (right) for the continuum-interaction case [68, 84]. The growth rate increases stepwise as more complete physics is considered, suggesting the important of thermal gyrokinetic and finite  $E_{\parallel}$  effects. In the left-most graph the same colours are used to represent EUTERPE in mixed-variables formulation, FLU-EUTERPE with gyrokinetic bulk ions, and the ideal MHD eigenvalue code CKA.

Finally, a fully gyrokinetic treatment of the thermal plasma yields a yet higher growth rate, despite little change in mode structure. Physically, electron kinetic physics

is added, potentially including electron inverse Landau damping, while the fluid truncations are no longer present such that the complete collisionless  $E_{\parallel}$  physics is included.

Once again, in all cases, it is seen that the growth rate peaks at intermediate fast particle temperature, dropping off at higher temperatures. Once again, FOW and FLR effects are thought to be responsible, as the fast ion orbit widths become comparable to the machine size and the gradient scale lengths.

The mode frequency also varies with fast particle temperature. As in the ITPA TAE benchmark case, the mode frequency tends to increase with the thermal temperature of the fast particle population. In this case, however, the mode frequency begins at a higher level than in the ITPA TAE case seen in figure 4.2. This is due to the higher bulk plasma temperature.

As such, the mode frequency with a low temperature fast particle population begins close to the upper boundary of the toroidicity gap. Referring back to the continuum in figure 4.8, it can be seen that near the upper edge of the  $m = 10, 11$  gap, a mode would be interacting with the continuum through poloidal side-bands with different values of  $m$ . This would explain the mode structure modification behaviour presented in figure 4.9.

Note that the upshift in growth rate over the ideal MHD model, where the bulk plasma temperature is not a parameter, is dependent upon the higher bulk plasma temperature compared to the ITPA TAE case. When the ITPA TAE bulk plasma temperature of 1 keV is taken, there is no observed upshift in growth rate [68].

With the increasing fast particle temperature, the mode frequency actually leaves the  $m = 10, 11$  ideal MHD toroidicity gap. Nonetheless, the mode is sufficiently strongly driven that it remains unstable despite experiencing direct continuum damping. It is perhaps significant that this continuum damping begins at around the same fast particle temperature where FOW effects reverse the increase in growth rate of the mode, so that the two damping mechanisms are not easily distinguishable in this case.

This case illustrates the use to which the hierarchy of fluid models can be put in distinguishing the causative mechanisms of various physical phenomena observed in simulations of global modes. It is particularly significant that the multi-harmonic global structure in the centre panel of figure 4.9 disappears when ions are no longer considered as a separate kinetic species [84].

## 4.4 TAE elongation study

In the ITPA benchmark case, a circular geometry is considered. The choice of circular geometry in the ITPA TAE benchmark case is a response to the limitations of some codes. Some codes, for instance, assume circular flux surfaces. More complex geometries are also known to be a source of numerical error when discretised, which can be especially problematic when small numerical errors can be amplified, as in the case of the cancellation problem. It has been observed in the past that fully gyrokinetic simulations are more challenging in terms of the cancellation problem in non-circular geometries.

Modern tokamak experiments, however, typically have significantly elongated ge-

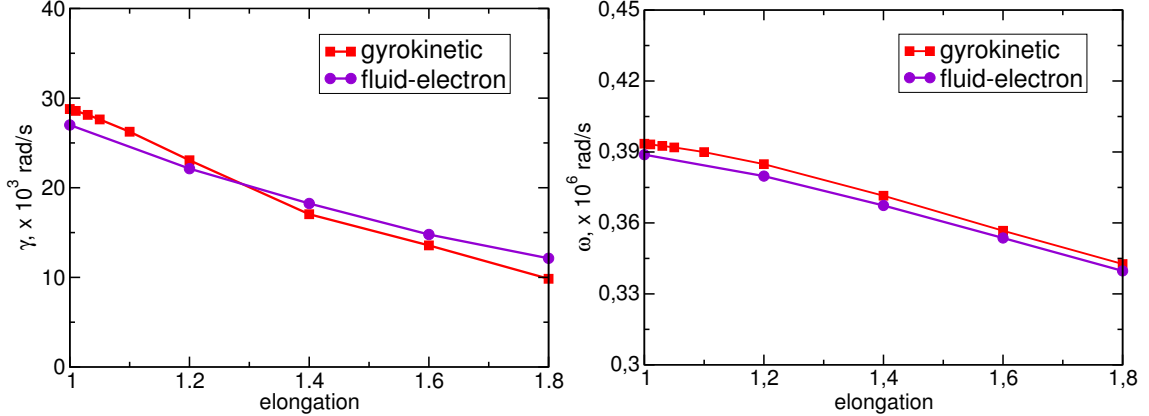


Figure 4.11: Growth rate (left) and frequency (right) for the ITPA TAE benchmark with nominal parameters and  $T_f = 400$  keV, except here the elongation parameter of the magnetic equilibrium is varied. A minor frequency drop and significant reduction in linear growth rate are observed.

ometries, which has beneficial influence on stability. It is therefore of interest both to validate the code in non-circular geometry, and to investigate how a finite elongation affects the physics.

We consider a case with the nominal ITPA parameters and fast particle temperature  $T_f = 400$  keV, but this time instead of circular geometry a 2D shaped cross-section with finite elongation is considered. Elongation is quantified in terms of the elongation parameter  $\kappa$ , which is defined in terms of the minor and major radius as follows,

$$R_c(\theta) = R_0 + a \cos(\theta), \quad Z_c(\theta) = \kappa a \sin(\theta) \quad (4.4)$$

with  $\theta$  being the poloidal angle. Reactor-relevant tokamak plasmas such as JET and ITER have an elongation around  $\kappa \approx 1.8$ . We increase  $\kappa$  stepwise between 1.0 and 1.8 by considering several different VMEC equilibria. These runs are repeated with both the fluid-electron hybrid model and the fully gyrokinetic model.

In figure 4.11, we see that increasing elongation exerts a minor influence on the mode frequency, which is reduced within the gap, while the linear growth rate of the TAE mode is significantly reduced relative to the circular ITPA case, a result predicted also by analytical theory. Almost exact agreement is seen between the fluid-electron and gyrokinetic models.

Note that there is some quantitative disagreement between the growth rates and frequencies in this case at  $\kappa = 0$  and the corresponding circular tokamak ITPA TAE case presented previously. This is due to a somewhat different choice of bulk plasma parameters, which shifts the position of the gap, but does not invalidate the observed qualitative trends.

Since modern large tokamak experiments have a  $\kappa$  of around 1.8, the significant stabilisation effect of elongation is important for quantitative predictions of fast particle transport by Alfvén eigenmodes. This effect should therefore be taken into account in future numerical work aimed at providing experimental predictions of fast particle behaviour.

## 4.5 Internal kink mode

The internal kink mode is a current-driven MHD instability that occurs at a resonant surface, that is where the safety factor,  $q$ , is an integer. Internal kink stability is one limitation to the parameter space in which a toroidal magnetic confinement device can operate. Since the instability of the internal kink mode generally increases with lower rational surface number, it is generally of prime importance to calculate whether or not the  $q = 1$  internal kink is stable. It is also related to many other phenomena that occur even in stable steady state plasmas, such as sawtooth oscillations.

### 4.5.1 In a screw pinch

The screw pinch magnetic geometry is a linear geometry in which a magnetic field is generated by a helical current. It can be seen as a limiting case for the tokamak geometry in which the major radius goes to infinity. By analogy, the concept of a safety factor for the internal screw pinch can be characterised as the inverse ratio of the current in the direction parallel to the axis of the device,  $\vec{e}_z$ , and that around the device, i.e. in direction  $\vec{e}_z \times \vec{e}_r$ , where  $\vec{e}_r$  is the radial direction.

In screw pinch geometry the internal kink mode has been treated with fully gyrokinetic codes, such as GYGLES [67] and LIGKA [108]. The models implemented in these codes are equivalent to those of linear fully gyrokinetic EUTERPE in axisymmetric geometry. These codes can be used to benchmark the reduced models.

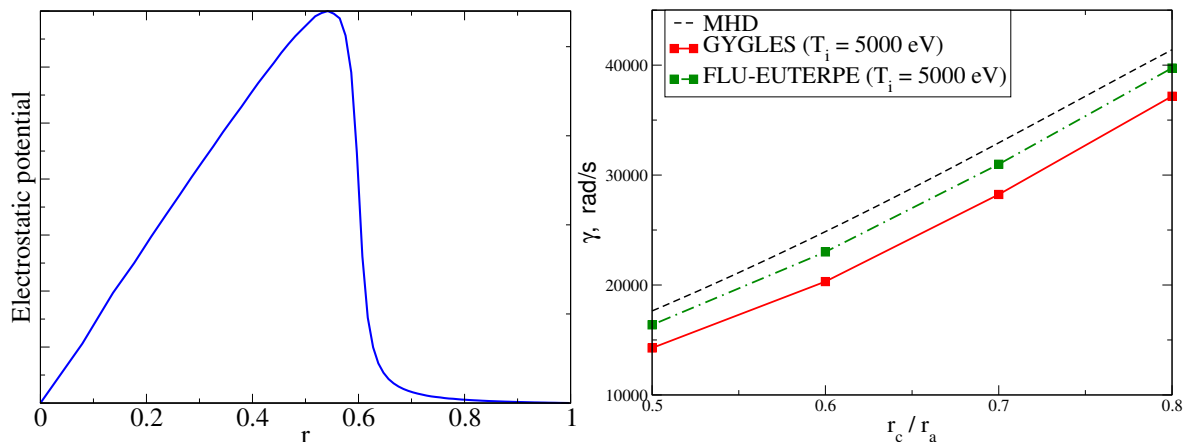


Figure 4.12: The kink mode structure in terms of the perturbed electrostatic potential (left), and the growth rate as it varies with the position of the resonant surface (right) [83].

We choose a screw pinch geometry where the ‘major radius’ of the screw pinch  $R_0 = 5.0$  m (here the major radius merely defines the length of the simulation domain and does not imply curvature), the minor radius  $r_a = 1.0$  m and the magnetic field strength  $B_0 = 2.5$  T. Bulk plasma density and temperature profiles are flat, and the internal kink mode is destabilised by the gradient of the bulk plasma parallel current alone. The plasma density  $n_0 = 2 \times 10^{19} \text{ m}^{-3}$  and the plasma temperature

$T_i = T_e = 5$  keV. The safety factor profile is given by  $q(r) = 0.6 + 0.4(r/r_c)$ , where  $r_c$  is radial position of the resonant surface where  $q = 1.0$ .

In the Fourier filter the single Fourier harmonic with toroidal mode number  $n = 1$  and poloidal mode number  $m = 1$  is isolated, as there are no Fourier couplings in this geometry. As shown in figure 4.12 (left), the expected mode structure is produced, with the perturbed electrostatic potential rising linearly with  $r$  from the magnetic axis before rapidly dropping off at the resonant surface. This result can be compared with that from fully gyrokinetic GYGLES. As predicted by theory and previous simulations, the mode has zero real frequency [67].

It is predicted by analytical theory that the growth rate of the internal kink mode should vary with the position of the  $q = 1$  resonant surface. Quantitatively, the growth rate of the internal kink mode can be compared with the previous results for different values of  $r_c$ , see figure 4.12 (right). The quantitative growth rates predicted by FLU-EUTERPE, the gyrokinetic PIC code GYGLES, and MHD are in close agreement. Both gyrokinetic models, however, show a reduced growth rate at higher bulk plasma temperatures. This effect is stronger in GYGLES than FLU-EUTERPE, suggesting that stabilisation in this case may also relate to finite  $E_{\parallel}$  effects, which are neglected by FLU-EUTERPE.

## 4.5.2 In a tokamak

In a tokamak, the internal kink mode is driven unstable when a large toroidal plasma current is present in the core of the device, reducing the safety factor such that it crosses the the most unstable,  $q = 1$ , rational surface in the core. The internal kink mode is close to a limiting case, requiring a global treatment in the deep MHD limit, and has therefore been difficult to simulate numerically.

Unlike in straight geometry, however, where the instability is purely current-driven, in toroidal geometry the kink mode requires a radial pressure gradient to become unstable [109]. As a result, the kink stability can also impose a limit on the achievable normalised plasma pressure,  $\beta$ . In particular, the destabilisation of an  $m = 1$  kink-like mode is thought to be responsible for the sawtooth cycle, a ubiquitous tokamak phenomenon in which  $m = 1$  unstable modes periodically accompany a collapse in core density, temperature, and conductivity.

Although the  $m = 1$  instability itself is an MHD instability, kinetic effects can become important. There are two key effects. First, the resonant layer can be narrow enough that kinetic effects can be important in determining the physics on the short scales within the layer. Second,  $m = 1$  modes can be both stabilised and destabilised under the influence of fast particles by kinetic effects.

Considering the internal kink mode without fast particles, we first attempt a benchmark between the fluid thermal plasma FLU-EUTERPE model and the reduced ideal MHD eigenvalue code CKA. The set of equations solved by FLU-EUTERPE are here in principle equivalent to the vorticity equation solved by CKA, but the numerical approaches are different. [83]

Our chosen magnetic geometry is a large aspect ratio tokamak with  $R_0 = 2.5$  m,  $a_0 = 0.25$  m and  $B_0 = 4.6$  T. The safety factor profile varies between  $q = 0.85$  at

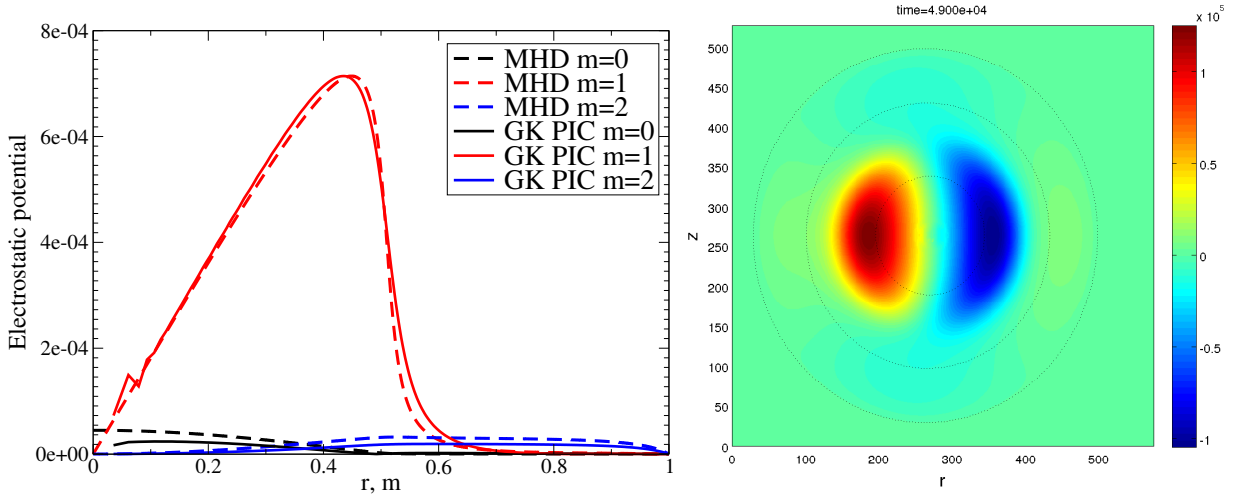


Figure 4.13: The radial mode structure of the kink mode in terms of the perturbed electrostatic potential decomposed into poloidal harmonics compared from FLU-EUTERPE and the reduced ideal MHD eigenvalue code CKA (left), and the mode structure as perturbed electrostatic potential plotted in a cross-section through the tokamak from FLU-EUTERPE (right) [83].

the magnetic axis to  $q = 1.8$  at the edge. The  $q = 1$  rational surface is located at  $r/a_0 = 0.5$ .

The thermal plasma is taken to have a normalised pressure of 0.052 at the flux surface  $s = 0.5$ , and average density  $4.65 \times 10^{19} \text{ m}^{-3}$ . A density gradient is applied with the form,

$$\frac{n'(s)}{n} = -\kappa_n \cosh^{-2} \left[ \frac{s - s_p}{\Delta} \right], \quad (4.5)$$

where  $s$  is the normalised poloidal flux,  $s_p$  is the position of the peak gradient,  $\Delta$  is the characteristic width of the peak, and  $\kappa_n$  characterises temperature gradient. In this case, the parameters chosen are  $\kappa_n = 0.5$ ,  $\Delta = 0.2$  and  $s_p = 0.2$ . The temperature profile is flat.

In FLU-EUTERPE, a filter is applied centred on the toroidal mode number  $n = 0$  and poloidal mode number  $m = 1$ , with poloidal sidebands  $m = 0$  and  $m = 2$  also included. In CKA, a real frequency range is chosen within which to search for eigenfunctions, and the calculated eigenmodes are visually inspected for agreement. Since the internal kink mode has no real frequency, the choice of frequency range is largely arbitrary provided it includes  $\omega = 0$ .

In FLU-EUTERPE, the internal kink mode is the fastest growing mode and therefore appears after a brief transient phase. In CKA, the internal kink mode is one solution found, along with a large number of strongly damped continuum modes. In figure 4.13, the mode structures calculated by the two codes are plotted and compared; very close agreement is seen between the eigenvalue code CKA and the initial value code FLU-EUTERPE. Both codes are also capable of calculating quantitative growth rates, which in this case are also in close agreement,  $\gamma_{FLU} = 1.29 \times 10^6 \text{ s}^{-1}$  and

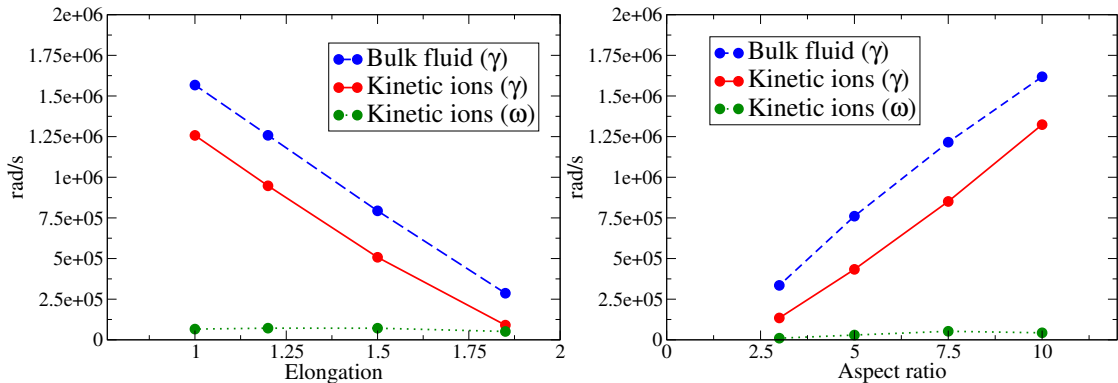


Figure 4.14: Plots of the growth rate of the internal kink mode in tokamak geometries scanned in elongation (left) and aspect ratio (right). Note the small but finite real frequency that accompanies that downshift in the growth rate upon inclusion of thermal ion gyrokinetics. [83]

$$\gamma_{CKA} = 1.27 \times 10^6 \text{ s}^{-1}.$$

The internal kink mode exists in the far MHD limit, where  $k_{\perp}\rho_i$  is very small. It is therefore a case in which the cancellation problem would be particularly prominent in a fully gyrokinetic electromagnetic PIC model.

The initial benchmark is expanded by considering the effect of geometry and gyrokinetic thermal ions. In figure 4.14, the growth rate of the internal kink mode is plotted for varying tokamak aspect ratio and elongation. Both the reduction in aspect ratio and the increase in elongation are shown to improve the stability of the system to the internal kink mode. An aspect ratio in the region of  $R_0/a_0 = 3.0$  and an elongation in the range of  $\epsilon = 1.8$  correspond to the parameters of modern conventional tokamak devices such as JET and ITER.

The results here confirm predictions of analytical theory. Work by Wahlberg, for instance, shows that, in the parameter range relevant to current large tokamak experiments, the internal kink mode is stabilised by decreasing aspect ratio at large  $\beta$  [110]. Later such work demonstrated that, with high  $\beta$  and a safety factor value  $q$  close to unity over a large proportion of the radius, elongation also stabilises the internal kink mode. In the case of a weak pressure gradient and the  $q = 1$  resonant surface being close to the magnetic axis, however, elongation can also be destabilising [111]. Numerically this second case was considered earlier by Bondeson and Bussac [112].

The addition of gyrokinetic thermal ions produces a consistent reduction in the instability of the mode without affecting the qualitative trends. A new source of damping, such as ion Landau damping, has been introduced but does not change the underlying physics of the instability. This observation has been physically justified as the finite radial orbit widths of trapped particles serving to average perturbations radially [113, 62]. Gyrokinetic bulk ions also introduce a small but finite real frequency, consistent with previous simulations using eigenvalue codes [62, 108].

## 4.6 Linear $m=1$ EPM

In this section, we continue to consider the  $m = 1$  mode, but now under the influence of a population of fast particles. An EPM occurs when the fast particle  $\beta$  is comparable to the bulk plasma  $\beta$ , and the mode structure can be significantly modified by the influence of the fast particles.

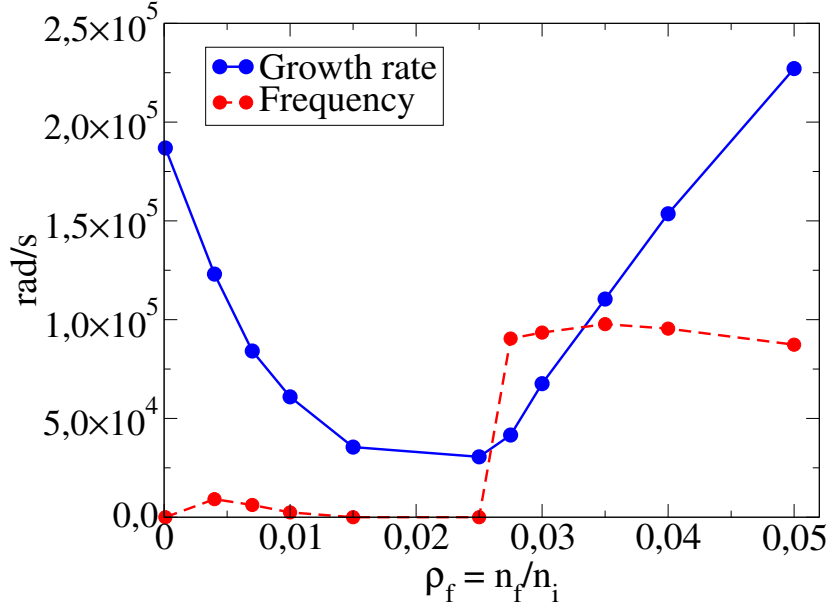


Figure 4.15: Growth rate and frequency of the linear  $m = 1$  mode varying with fast particle density fraction,  $\rho_f$  [83]. Two different modes can be distinguished by their real frequency: the internal kink mode with approximately zero real frequency, and the EPM with an approximately constant, finite real frequency. The transition coincides with a change in the sign of the gradient of the growth rate in  $\rho_f$ .

The same magnetic geometry is used as for the kink mode simulations in the previous section. The bulk plasma temperature is lowered to  $T_i = T_e = 3$  keV, with the same bulk plasma gradients as in the previous simulations. Using the non-perturbative code FLU-EUTERPE, the bulk plasma is treated as a fluid, as the kinetic effects we are interested in come from the energetic particle population driving or damping the mode.

We apply a Maxwellian population of fast deuterium particles with a density gradient again of the form,

$$\frac{n'(s)}{n} = -\kappa_n \cosh^{-2} \left[ \frac{s - s_p}{\Delta} \right], \quad (4.6)$$

where again  $s_p = 0.2$ ,  $\Delta = 0.2$  and  $\kappa_n = 3.0$ . The temperature of this fast particle population is  $T_f = 300$  keV, with a flat fast particle temperature profile. The strength of the energetic particle drive is varied by varying the density, expressed from now on as a fraction of the bulk plasma density,  $\rho_f = n_f/n_0$ .



In figure 4.15, it can be seen that, upon increasing the fast particle fraction  $\rho_f$ , the growth rate of the zero real frequency internal kink mode reduces. As before, it is suggested that this is due to the finite radial displacement of the trapped particle banana orbits averaging the perturbation radially, this time with larger orbit widths leading to greater degree of averaging. The stabilisation of the sawtooth by fast particles has also been seen experimentally [43], but as the fast particle  $\beta$  in existing experiments is small compared to that in reactors, numerical simulations are important in quantifying its significance. Stabilisation of  $m = 1$  modes by fast particles has been predicted numerically in ITER [59].

At  $\rho_f = 0.025$ , a sudden increase in the real frequency is observed and the growth rate begins to increase linearly with  $\rho_f$ , eventually exceeding that of the kink mode in the absence of fast particles. This is the emergence of an EPM, which corresponds to a distinct branch of the dispersion relation. It would be reasonable to propose that this frequency corresponds to the fast particle precession frequency.

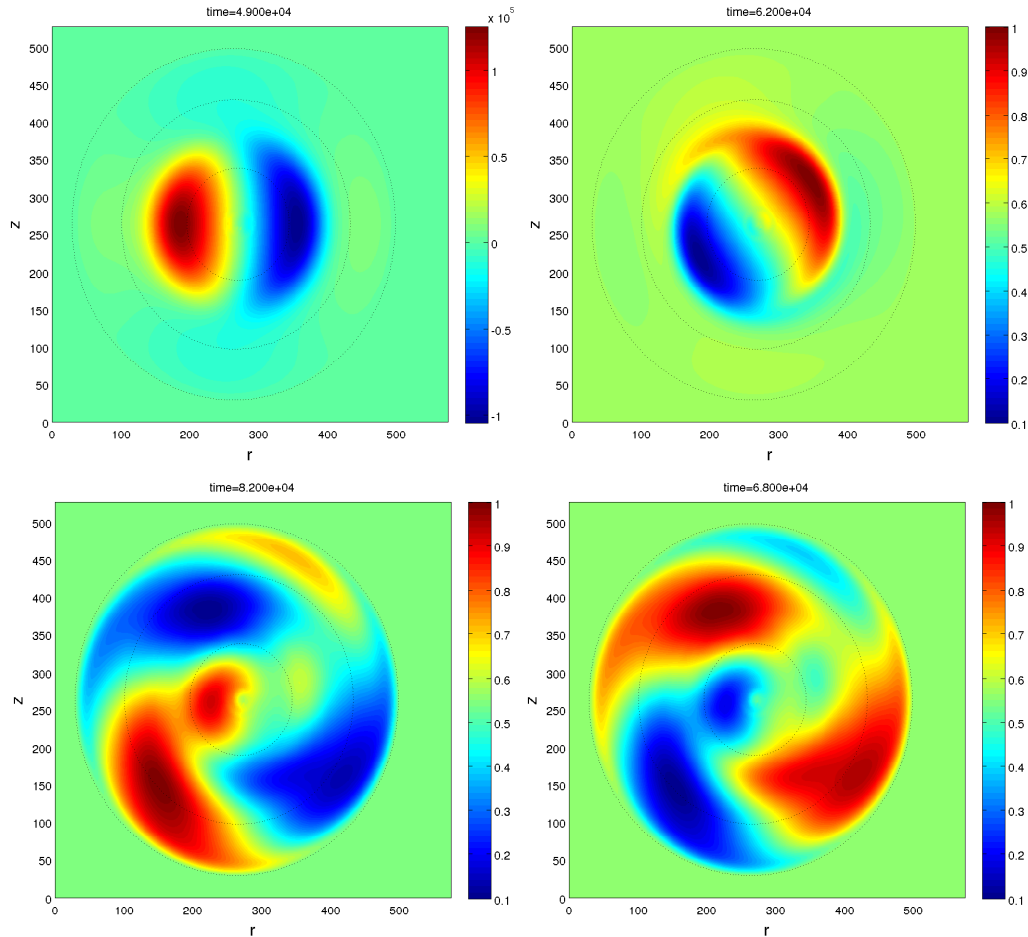


Figure 4.16: Kink and EPM mode structures calculated with FLU-EUTERPE compared, from top to bottom and left to right: the pure MHD kink mode shown previously, the kink mode under the influence of fast particles, the EPM at one stage in its oscillation, and at  $90^\circ$  out of phase [83].

In figure 4.16, the mode structure is plotted for the pure  $m = 1$  kink mode, the kink mode suppressed by fast particles, and finally the EPM, which in addition to an  $m = 1$  component now also has higher poloidal harmonic components. Both the damped internal kink mode and the EPM rotate in the  $r - z$  plane under the influence of fast particles, while the MHD internal kink mode is stationary.

One can see a slight modification of the mode structure coinciding with fast particle stabilisation of the internal kink mode. This effect may therefore be encompassed by a perturbative model, such as CKA-EUTERPE. The EPM, however, has a clearly distinct mode structure, in which an  $m = 2$  poloidal harmonic becomes co-dominant with the  $m = 1$  harmonic.

These simulations demonstrate the ability of the FLU-EUTERPE hybrid models to simulate global mode physics in the deep MHD limit in shaped geometry close to that of real tokamak experiments, where the gyrokinetic models encounter numerical difficulties such as the cancellation problem and perturbative hybrid models exclude important physics. The key physical features of kink stabilisation by fast particles, and the fishbone EPM, have been demonstrated, along with the ability to include thermal ion kinetic effects. Future simulations with parameters corresponding to fusion devices such as JET and ITER can now be envisioned.

## 4.7 Global mode in Wendelstein 7-X

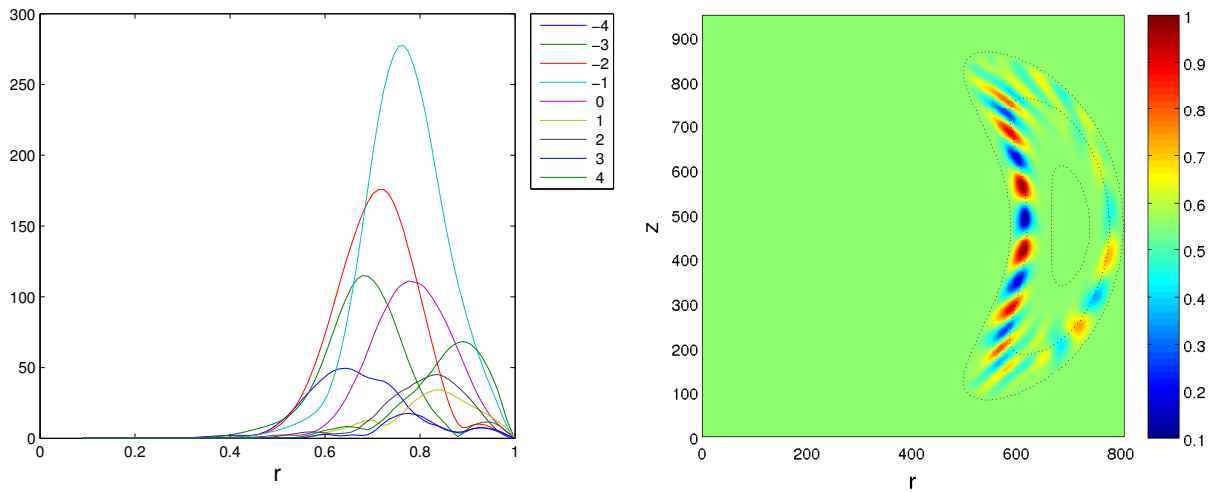


Figure 4.17: The structure of a global mode in W7-X, depicted as the perturbed electrostatic potential decomposed into poloidal modes plotted in radial position (left), and as the total perturbed electrostatic potential plotted in a cross-section through W7-X (right). Note that the poloidal harmonics in the left-hand plot are normalised to the filter, such that plotted  $m = 0$  corresponds to physical  $m = 14$ .

EUTERPE is a code developed to treat general 3D geometries. The primary application of this capability is to investigate physics in stellarators. The optimised stellarator

Wendelstein 7-X will be used to investigate the properties of a quasi-isodynamic geometry. One limitation of the stellarator concept is poor fast particle confinement relative to axisymmetric devices such as tokamaks. Wendelstein 7-X has been designed to approximate as closely as possible a quasi-isodynamic geometry principally in order to mitigate this disadvantage.

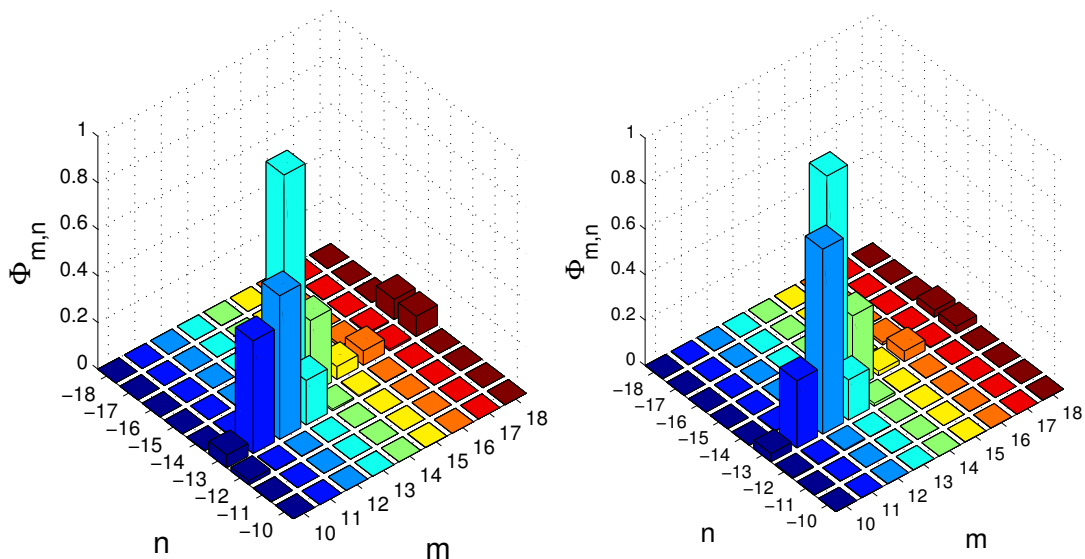


Figure 4.18: The global mode in W7-X depicted as the perturbed electrostatic potential decomposed into toroidal and poloidal components, plotted for the fluid model (left) and fully gyrokinetic model (right). There is some difference in the relative significance of some harmonics, but the structure of the mode found by each model is qualitatively the same.

In the course of this work, the first global fully gyrokinetic simulations of W7-X have been conducted. This case has then been considered with the hybrid models.

We consider the magnetic geometry of the envisioned W7-X ‘high mirror’ case, in which the difference between the peak magnetic field strength and the minimum magnetic field strength is greatest. This VMEC equilibrium corresponds to one of the primary experimental scenarios that will be investigated with the device as it comes in to operation.

We assume flat background plasma profiles with  $T_e = T_i = 3$  keV and  $n_0 = 1 \times 10^{20} \text{ m}^{-3}$ . The equilibrium magnetic field on axis,  $B_0 = 2.6$  T. A Maxwellian fast particle population is applied to drive global modes, with density profile given by the equation,

$$n_f(s_{pol}) = n_{0f} \exp \left[ -\frac{\Delta}{\kappa} \tanh \left( \frac{s_{pol} - s_{nf}}{\Delta} \right) \right] \quad (4.7)$$

with peak density  $n_f = 5 \times 10^{18} \text{ m}^{-3}$  and temperature  $T_f = 1$  MeV.

In an optimised stellarator case a high poloidal and toroidal resolution must be adopted in general, which permits a wider Fourier filter in poloidal and toroidal mode number. As greater coupling between adjacent modes is to be expected, it may be

necessary to resolve this large number of modes. Furthermore, unlike in axisymmetric simulations, physical toroidal coupling particularly is now present in linear simulations.

For this case we therefore choose a filter centred on poloidal mode number  $m = 14$  and toroidal mode number  $n = -14$ , including all modes within the range  $\pm 4$  of these central values. Note that, due to the five-period symmetry of the W7-X stellarator, each step in toroidal mode space corresponds to a change in  $n$  of five.

In figure 4.17, we plot the mode structure in terms of the perturbed electrostatic potential in a cross-section through the stellarator, using the hybrid model. In figure 4.18, the power spectrum is plotted in comparison for the fluid and gyrokinetic models, showing a group of poloidal and toroidal harmonics localised in the filter. Close agreement is seen between the fluid and gyrokinetic results, giving good reason for confidence in the existence of this mode and the validity of both models.

The quantitative linear growth rate, however, is significantly different in the two cases. The fully gyrokinetic model for these parameters shows a linear growth rate of  $\gamma_{GK} = 6.51 \times 10^4 \text{ rad s}^{-1}$ , compared to  $\gamma_{fluid} = 1.42 \times 10^5 \text{ rad s}^{-1}$  for the fluid model. It is proposed that bulk plasma Landau damping is significant in this case, which may be explicable by the high bulk plasma temperature.

#### 4.7.1 Limits to stellarator simulations

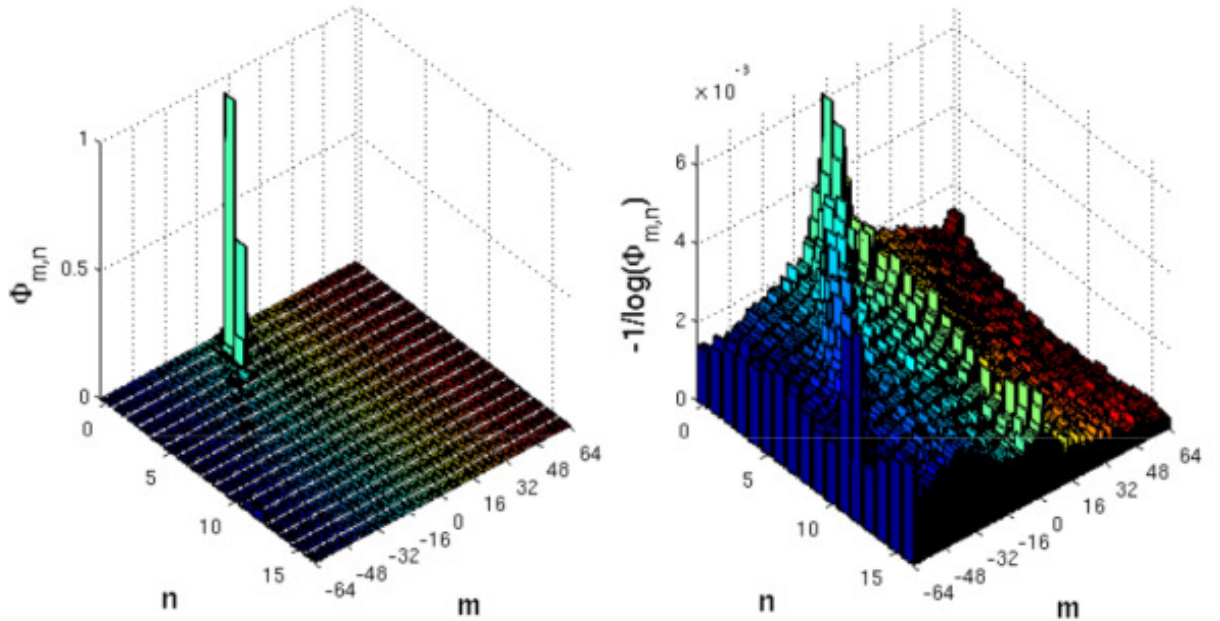


Figure 4.19: Left to right: the global mode with dominant low poloidal and toroidal mode numbers, the extended global mode structure seen with the electrostatic perturbation plotted on a log scale.

In the case presented in the preceding section, the normalised fast particle pressure,  $\beta_f$ , was higher than the expected experimental values in Wendelstein 7-X or even a reactor that may be based on its design. An experimental fast particle density in the

region of  $\rho_f = 0.001$  is to be expected for Wendelstein 7-X, and perhaps  $\rho_f = 0.01$  for a reactor, with comparable fast particle temperatures. With realistic bulk plasma parameters, the experimental ratio of  $\beta_f$  to the thermal  $\beta$  is at least an order of magnitude lower for Wendelstein 7-X and a factor two to five lower for a reactor.

To investigate the behaviour of the gyrokinetic code as fast particle parameters approach more closely the experimental, simulations were performed with progressively lower  $\beta_f$ . The minimum value of  $\beta_f$  that would yield a numerically stable and physically sensible result was observed to depend strongly on the poloidal and toroidal resolution. Both were increased to the limits of the available memory for solving the matrix equations in their present formulation and implementation.

Taking the highest resolution case considered, and including all resolvable poloidal and toroidal mode numbers within a filter centred on  $m = 0$  and  $n = 0$ , we are able to resolve down to a fast particle pressure  $\beta_f$  of  $0.025\beta_0$ . We perform a simulation with these parameters for the fast particles and all others as in the previous sub-section. At large timestep the simulation fails. In figure 4.19, the power spectrum of the perturbed electrostatic potential in terms of poloidal and toroidal mode numbers is depicted. Re-plotting this data on a log scale, however, reveals a more complex extended global structure of coupled modes.

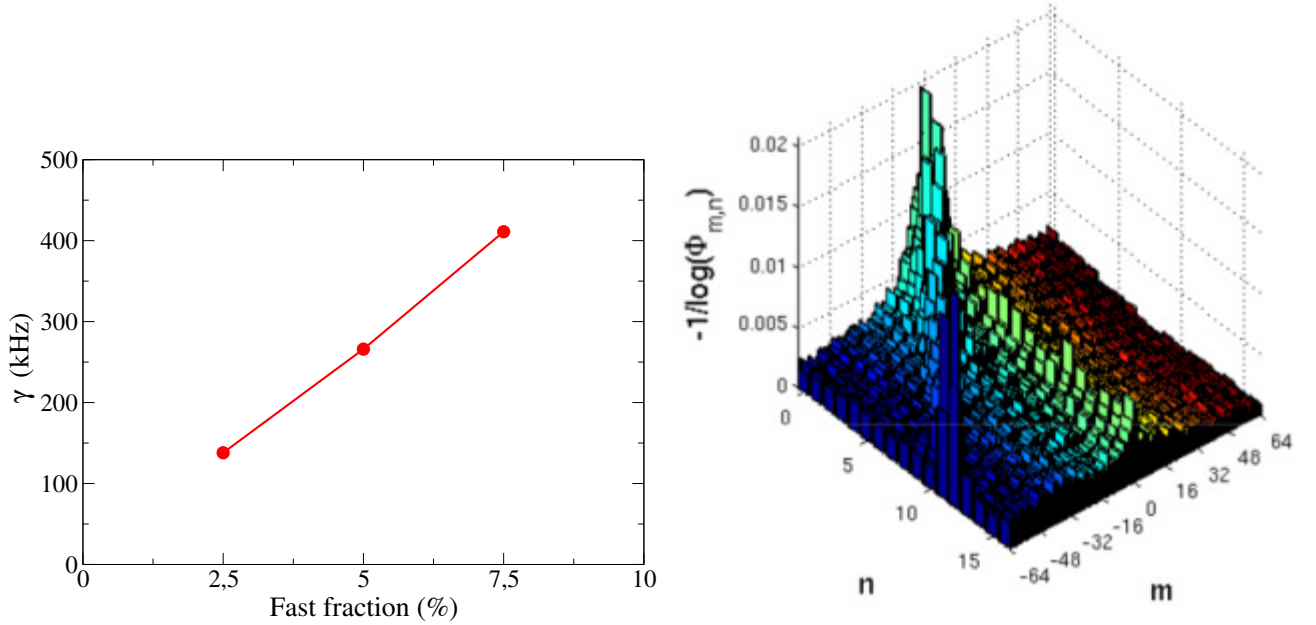


Figure 4.20: Left to right: the growth rate of the global mode with fast particle density fraction, the same global structure as above, now at low fast particle  $\beta$  and large simulation time.

As the fast particle density is reduced, it is observed that this extended coupled mode structure increases in relative strength. In the marginal case where a simulation fails and at large timestep, the power spectrum at high timestep is plotted in figure 4.20, an accumulation of electrostatic potential is observed where this structure meets the edge of the filter. Similar behaviour is observed with both the gyrokinetic and fluid-

electron hybrid schemes. In figure 4.20 (left), the variation of growth rate with fast particle density is depicted; it can be seen that the mode is still far from marginal stability at the lowest practical fast particle beta, and no significant transition occurs at that point.

We observe that global stellarator simulations near to marginal stability with our systems of equations require very high poloidal and toroidal resolution in order to resolve fine scale structures. One possible approach to this problem is to impose damping to eliminate fine scale structures, while retaining the global mode of interest. Using the fluid-electron hybrid model, the resistivity term is capable of doing this, and this approach remains to be investigated.

It is also possible, however, that these fine scale structures are of numerical origin. One common property of both the fluid-electron hybrid, and mixed variables gyrokinetic models is the Ohms law equation, which may be a source of spurious numerical modes which may be of comparable growth rate to the physical modes. In future work, particular attention will be paid to the structure and consistency of the numerical implementation of the equations in order to avoid this.

# Chapter 5

## Non-linear simulations

In this section, the previous work is developed by repeating studies of the same cases but now solving the full first order non-linear gyrokinetic Vlasov equation,

$$\frac{\partial f_1}{\partial t} + \dot{\vec{R}}^{(1)} \cdot \frac{\partial f_1}{\partial \vec{R}} + \dot{v}_{\parallel}^{(1)} \frac{\partial f_1}{\partial v_{\parallel}} = -\dot{\vec{R}}^{(1)} \cdot \frac{\partial F_0}{\partial \vec{R}} - \dot{v}_{\parallel}^{(1)} \frac{\partial F_0}{\partial v_{\parallel}}, \quad (5.1)$$

where  $\dot{\vec{R}}$  and  $\dot{v}_{\parallel}$  indicate the full equations of motion, for at least one gyrokinetic species. Where the non-linear Vlasov equation is solved only for a fast particle species, this means retention of wave-particle non-linear interaction. If the non-linear Vlasov equation is solved for the bulk species, the wave-wave non-linear interaction is considered. As non-linear fluid terms derived in section 2.2 have not been included in the numerical implementation, any species treated by the fluid model will be treated linearly. A linear fluid model of one or more species may however be combined with a non-linear gyrokinetic model of other species, however.

As discussed in section 1.3.3, a qualitatively new behaviour is introduced, the non-linear saturation, whereby linear growth of an instability reaches an amplitude at which it reaches a new stable equilibrium. To obtain experimentally relevant predictions it is almost always necessary to reach a non-linearly saturated state. Successful non-linear simulations are therefore vital for the successful development of a useful tool.

As previously discussed for fast particle-driven modes, it is generally only necessary to consider the non-linear wave-particle interaction in order to obtain a saturation, although wave-wave interaction can be important for accurate quantitative predictions of the saturation level and saturated transport. Modes driven unstable by bulk gradients, such as the  $m = 1$  kink mode, require consideration of non-linear wave-wave interaction.

In this chapter, we will first consider the ITPA TAE benchmark case non-linearly. These results can be compared with those obtained previously by other hybrid codes. The hybrid model can therefore be validated non-linearly. Proceeding further we consider the effects of wave-wave interaction between multiple different modes in this case.

The  $m = 1$  instability work from section 4.6 will then again be considered non-linearly, demonstrating the successful simulation of the fishbone mode. Finally, the proof of principle global mode in stellarator simulations from section 4.7 will be shown to saturate non-linearly.

## 5.1 Toroidal Alfvén Eigenmode

To begin non-linear investigations we first test the fluid-hybrid model against a case that has already been performed non-linearly for other codes, the same ITPA TAE benchmark that was considered previously. This geometry of this case will then be used as a basis for further investigation. The case is particularly appropriate because the important gyrokinetic physics is contained in the fast particle species, and so as an initial test only this species need be treated non-linearly.

### 5.1.1 Non-linear ITPA TAE benchmark case

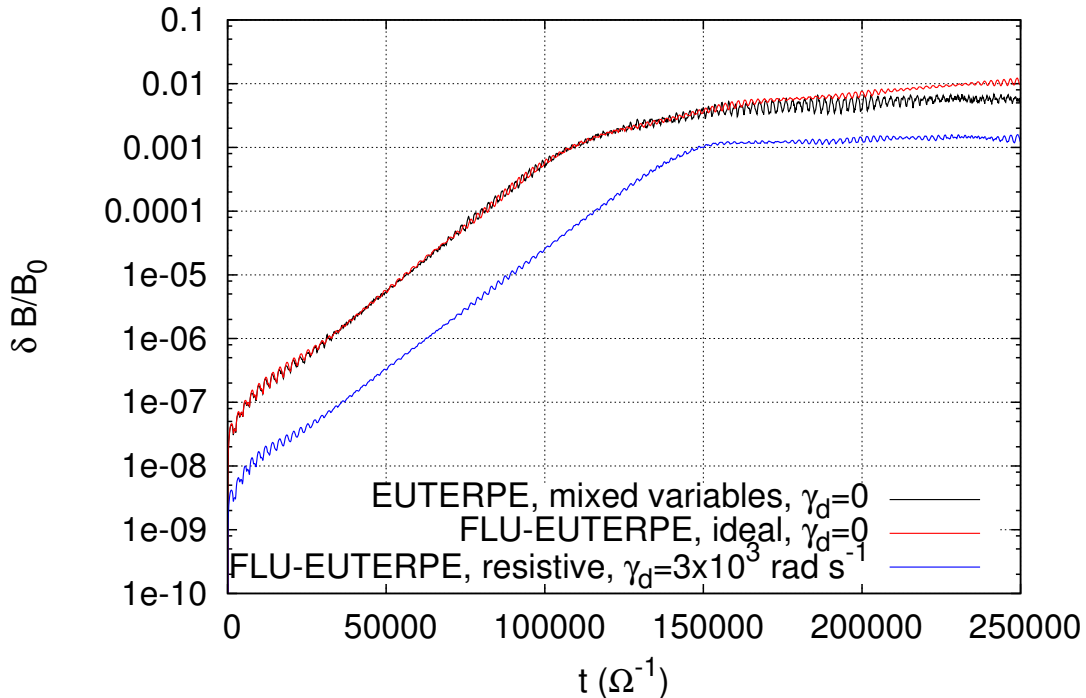


Figure 5.1: The evolution of the ratio  $\delta B/B_0$  depicted for the ITPA TAE benchmark case with wave-particle non-linearity considered, for the fully gyrokinetic model (black) and the fluid-electron hybrid model with (blue) and without (red) damping. The linear growth and non-linear saturated phases can be distinguished.

As an initial benchmark, we consider the ITPA TAE case using the fluid-electron hybrid model with and without resistive damping, and the fully gyrokinetic model without damping. In all cases, non-linear terms are retained only in the Vlasov equation for the fast particle species. As discussed in section 1.3.3, previous work suggests that this is qualitatively sufficient when treating a single mode. All other physical and numerical parameters are the same as in section 4.1, for the case where  $T_f = 400$  keV.

In figure 5.1, we plot the evolution of the perturbed magnetic field,  $\delta B$ , as a ratio of the unperturbed magnetic field,  $B_0$ , using all three models. Each shows a linear phase



in which there is exponential growth of the perturbed magnetic field, followed by a saturated phase during which the growth of the perturbation either halts or proceeds at a slower rate. Without damping, both the fluid-electron hybrid and fully gyrokinetic models show an upward drift in the perturbed magnetic field, which is eliminated by resistive damping in the fluid-electron hybrid model. This drift is substantially slower in the fluid-electron hybrid model than in the fully gyrokinetic model, perhaps due to the presence of ion and electron Landau damping, or increased resistive damping.

Without damping, there is a similar non-linear saturated perturbation amplitude in both cases, with an initial amplitude in the region of  $\delta B/B_0 \sim 10^{-3}$ . The full  $E_{\parallel}$  effects and/or electron kinetic physics therefore do not seem to have a strong influence in this case. This, however, remains to be investigated in detail. Furthermore, cases in which  $E_{\parallel}$  effects and/or electron kinetic effects are known to be important may help distinguish behaviour in the non-linear case. Resistive damping reduces the non-linear perturbed amplitude by a factor of 2 – 3. Since this is the first non-linear result for

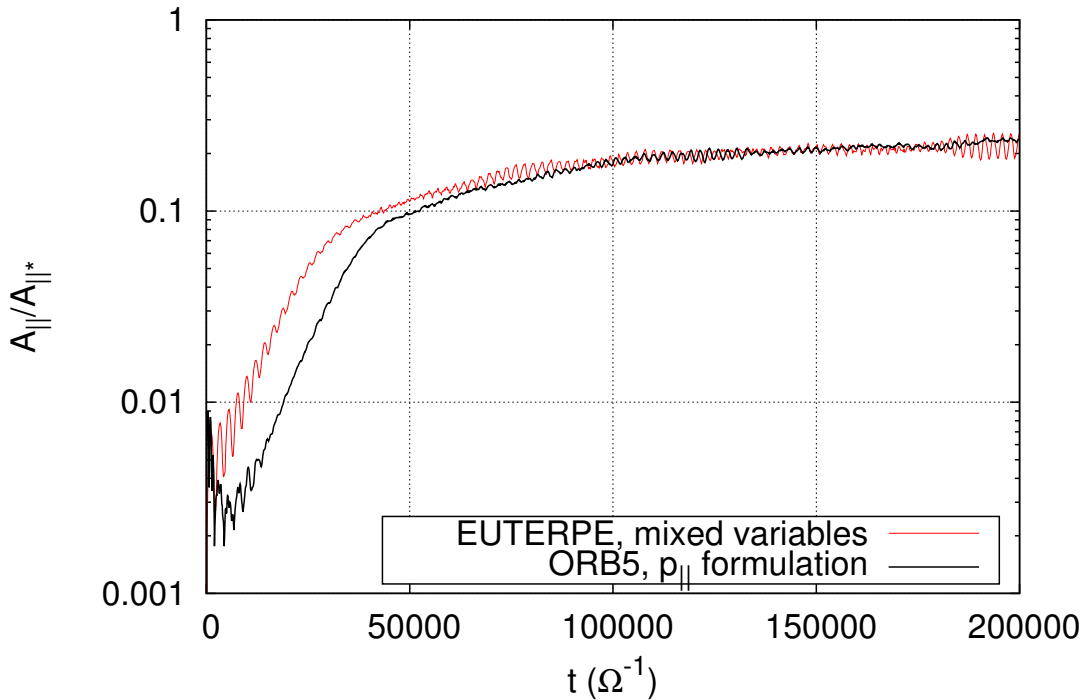


Figure 5.2: The evolution of the ratio  $\delta A_{\parallel}/A_{\parallel}^*$  in the ITPA case depicted for two non-linear gyrokinetic codes: NEMORB [114], which uses the  $p_{\parallel}$  formulation of the gyrokinetic equations of motion, and EUTERPE, which uses the mixed variables formulation of the equations.

this case using a fully gyrokinetic model with self-consistent fields, it is also of interest to benchmark the result with another gyrokinetic code in addition to reduced models. Due to recent improvements in the axisymmetric global electromagnetic gyrokinetic code NEMORB, such a comparison is possible in one case.

The comparison case chosen is the ITPA TAE case with  $T_f = 500$  keV, a reduced

mass ratio  $m_i/m_e = 200$ , and the fast particle concentration adjusted so as to equalise the linear growth rates at  $\gamma_L = 3.5 \times 10^4 \text{ m}^{-3}$ . In NEMORB is this the nominal ITPA density profile, and in EUTERPE it is the nominal ITPA density profile multiplied by a factor of approximately 0.7. We choose to hold constant the linear growth rate instead of the physical parameters because it is believed that the linear growth rate determines the non-linear physics, and for given physical and numerical parameters the linear growth rates differ between codes, as discussed in section 4.1 and depicted in figure 4.5. Although divergences between the linear physics predictions of the two codes are of some interest, they are not essential to benchmarking the capability of each code in the non-linear regime.

In figure 5.2, a comparison is plotted between the evolution of the perturbed parallel vector potential  $A_{\parallel}^*$  in normalised EUTERPE units, which are the same normalised units used in NEMORB. Excellent agreement is seen in the qualitative behaviour and the observed saturated perturbed amplitudes.

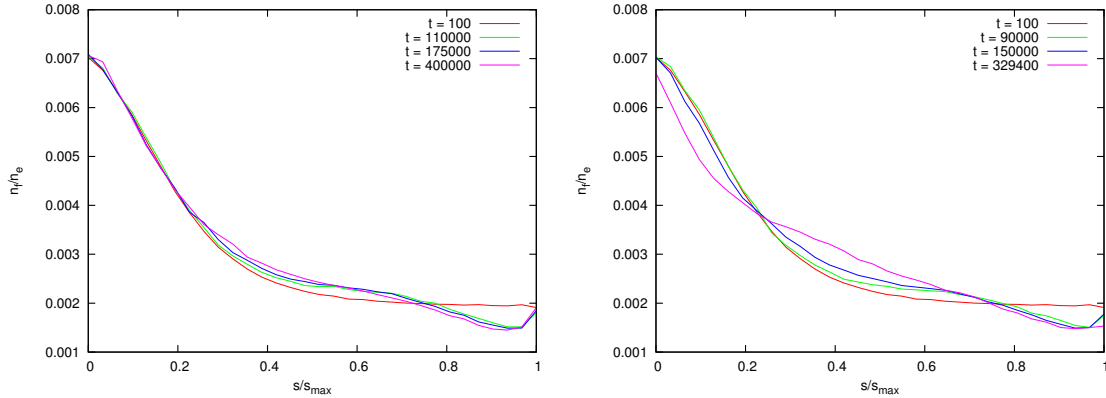


Figure 5.3: The evolution of the profiles of the energetic particle populations in the non-linear simulations using the fluid-electron hybrid model (left) and the fully gyrokinetic model (right). For reference, the time points can be compared to figure 5.1. The location of the mode peak,  $s = 0.25$ , can be seen to coincide with the point of greatest flattening in both cases.

In figure 5.3, the evolution of the fast particle profiles is compared in the undamped case with both the fluid-electron and the gyrokinetic models. One saturation mechanism is the redistribution of fast particles such that the driving fast particle gradient is reduced. In the fluid-electron hybrid model, some flattening is observed. However, in the fully gyrokinetic case this flattening is noticeably greater. A large proportion of the fast particle population is transported from the deep core to the central area of the device in the saturated stage, filling in the central fast particle gradient in the region of the mode peak.

Aside from its role in saturation, this fast particle redistribution is interesting in its own right, as a series of Alfvén eigenmodes at different radial locations can produce a pattern of profile flattening that quickly transports fast particles out of the device. In figure 5.4, the particle flux at each surface is plotted. Although the main transport takes place inside the device, in the gyrokinetic case there is somewhat greater transport

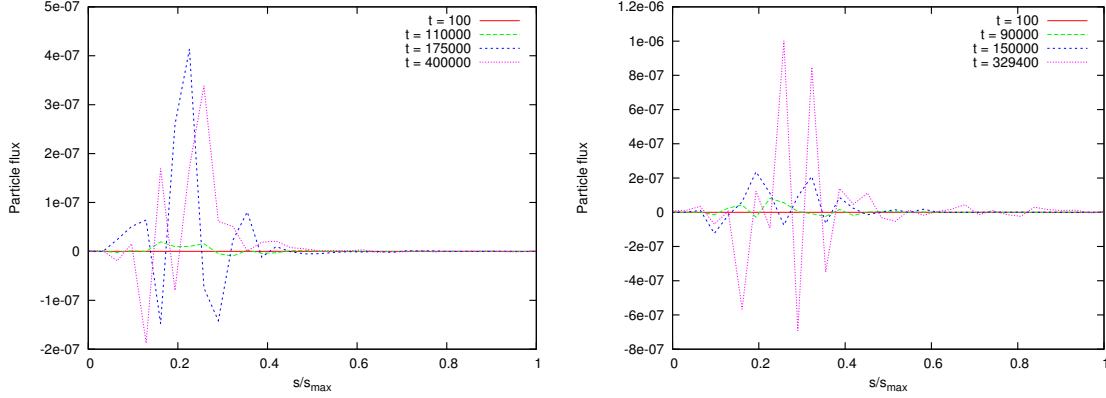


Figure 5.4: Evolution of the flux of energetic particles in nonlinear simulations using the fluid-electron hybrid model (left) and the fully gyrokinetic model (right). Again, time can be compared to figure 5.1. At large  $t$ , the fully gyrokinetic model shows greater particle flux than the hybrid model. This may be compared to the difference in profile flattening shown in figure 5.3.

toward the edge. As only a single mode is included in this simulation, transport across the whole radial extent of the device may be lower than in an experimental case.

In figure 5.5, the mode structures for the ideal and resistive fluid models, and the fully gyrokinetic model, runs depicted in figure 5.1 are plotted and compared. In the linear phase all three are practically identical as expected from section 4.1. In the non-linear phase, all models exhibit a comparable minor mode structure modification. This mode structure modification is of potential interest as it has not been considered by prior perturbative models, in which the mode structure is fixed.

Continuing, we conduct the non-linear ITPA TAE benchmark with other [non-]perturbative hybrid non-linear codes, using both fully gyrokinetic and fluid-electron hybrid models. Analytical theory predicts a quadratic relationship between the linear growth rate and the saturated perturbation amplitude in  $\delta B/B_0$ . By varying the linear growth rate in the ITPA case, we can compare the trends obtained with different codes.

In the fluid-electron hybrid simulations, a resistive damping is applied corresponding to a plasma Lunquist number of order  $10^4$ . This value is chosen such that the linear growth rate and saturated amplitude at one chosen point coincide with those of the other codes in the benchmark and does not necessarily represent experimental conditions.

The codes MEGA, HMG, and CKA-EUTERPE all also use damping to obtain a clean saturated amplitude for the mode. The code VENUS-K does not. As the fully gyrokinetic EUTERPE does not apply a damping, VENUS-K is therefore the most appropriate comparator. For EUTERPE, the non-linear perturbed amplitude is taken just after the end of the exponential growth phase, i.e. corresponding to  $t \sim 150000\Omega_c^{-1}$  in figure 5.1. This introduces some element of uncertainty as the position at which the non-linear perturbation amplitude is to some extent arbitrary. However, in the fully gyrokinetic case the amplitude grows linearly with time and increases by only a factor of 2 in order  $100000\Omega_c^{-1}$ , so it should be possible to obtain a meaningful trend.

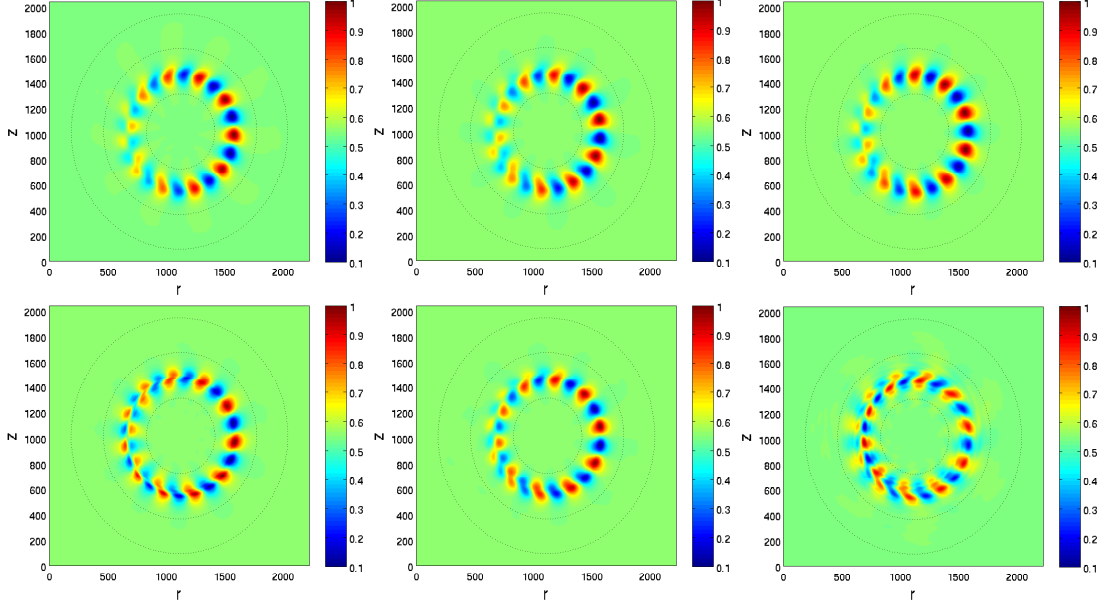


Figure 5.5: Mode structure comparison for the three models depicted in figure 5.1, from left to right: the ideal (undamped) fluid-electron hybrid model, the resistive fluid-electron hybrid model, the fully gyrokinetic model. Linear mode structures depicted above, non-linear below. All models show minor modification in the non-linear phase.

The linear growth rate is varied by varying the fast particle density fraction, between factor 0.5 and 2.0 of the nominal ITPA value. As shown in figure 4.4, the linear growth rate of the TAE in the ITPA case increases linearly with the fast particle density fraction. Theory predicts that the mechanism for altering the linear growth rate should not be important.

In figure 5.6, the results are plotted for the fluid-electron hybrid model FLU-EUTERPE and the fully gyrokinetic model EUTERPE, along with the perturbative hybrid model CKA-EUTERPE, the non-perturbative hybrid codes MEGA and HGMC, and the perturbative hybrid code VENUS-K. For FLU-EUTERPE, we obtain saturated amplitudes over a range of growth rates between  $\gamma = 1 \times 10^4 \text{ s}^{-1}$  and  $\gamma = 1 \times 10^5 \text{ s}^{-1}$ , and for EUTERPE over a narrower range. The difference in range is due to the inclusion of drift kinetic simulations for the FLU-EUTERPE case (ZLR), while all fully gyrokinetic EUTERPE simulations include FLR effects.

First, good agreement is seen between the FLU-EUTERPE results and those from comparable codes. MEGA and HMGC are both, like FLU-EUTERPE, non-perturbative fluid hybrid models of varying complexity, which include resistive damping. CKA-EUTERPE has all of these same features but with a fixed mode structure.

All codes show good agreement with the quadratic scaling for low linear growth rates. The trendline in the log-log plot corresponds to the quadratic trend between the linear growth rate and the non-linear saturation amplitude. In the Berk-Breizman model [22, 23], a quadratic dependence of the saturated amplitude on the linear growth rate is predicted. As the linear growth rate increases, this drops toward a linear rela-

tionship between the linear growth rate and the saturated amplitude.

Some difference is seen in saturated perturbation amplitude between the fluid-electron hybrid simulations with and without FLR effects. Those simulations without FLR effects show a slightly higher saturated level, but the same trend. It is possible that there is a minor modification of the physics by bulk ion FLR effects, as no such discrepancy is observed with the perturbative hybrid model CKA-EUTERPE.

The fully gyrokinetic results, meanwhile, show good agreement with the corresponding undamped perturbative hybrid model VENUS-K. These results are the first in this case obtained with a fully gyrokinetic non-linear global code. They suggest that, at least in this relatively simple case, the additional information provided by a gyrokinetic description of bulk ions and electrons is not that significant in predicting the saturated perturbation level.

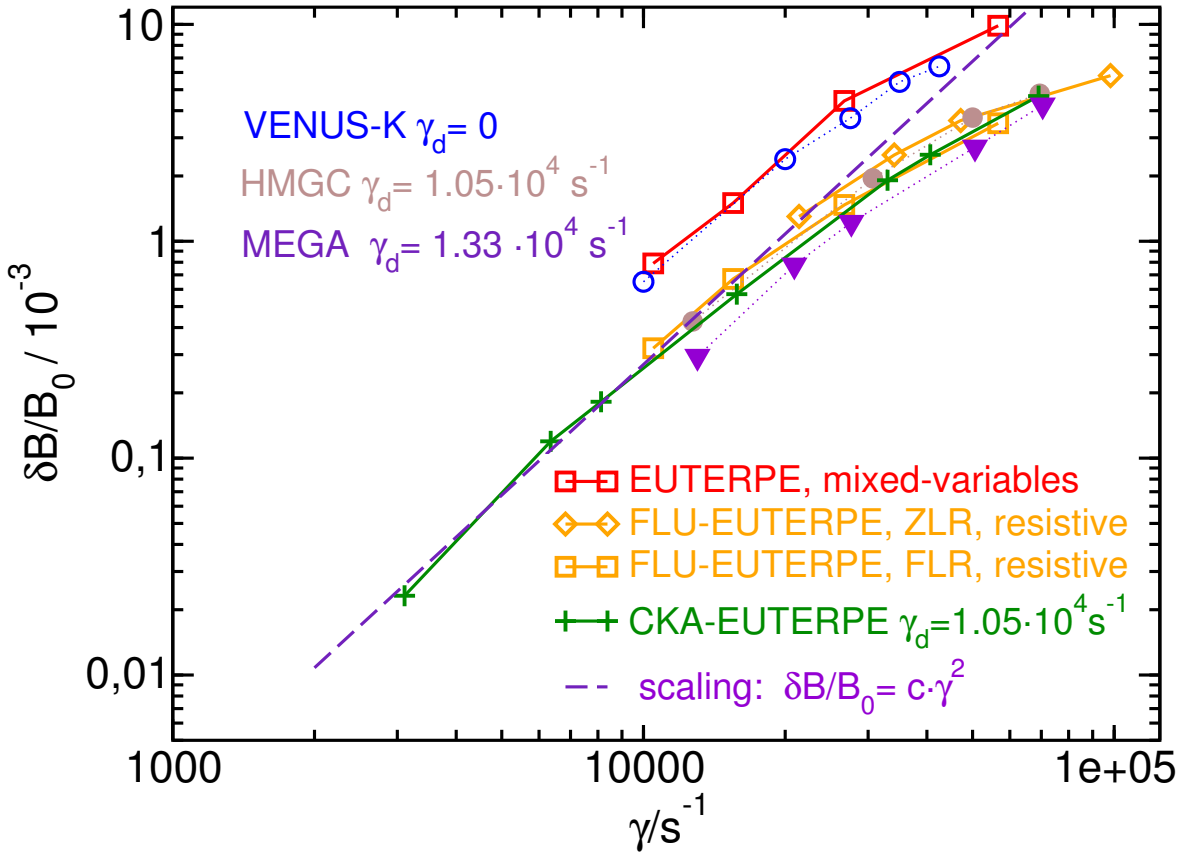


Figure 5.6: The relationship between the linear growth rate and eventual saturated amplitude of the maximum magnetic field perturbation as a ratio of the background field for a number of codes [115, 116, 117, 118]. Note that there is a quadratic relationship,  $\delta B \sim c\gamma_i^2$ , over some range of growth rates. This relationship is predicted by analytical theory [22, 23].

In the higher growth rate cases, mode structure modification is observed in the non-linear phase. In figure 5.7, the linear mode structure is plotted in comparison with the mode structure in the non-linear saturated phase for cases with linear growth rates

above  $4 \times 10^4 \text{ s}^{-1}$ .

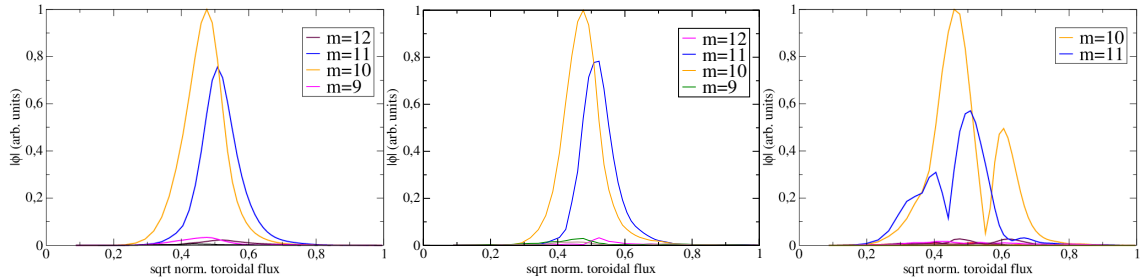


Figure 5.7: A depiction of mode structure modification in the saturated phase for non-linear simulations in terms of decomposed poloidal ( $m$ ) harmonics. From left to right: the mode structure in the linear phase, the mode structure in the saturated phase for linear growth rate  $\gamma = 1.05 \times 10^4 \text{ s}^{-1}$ , and the mode structure in the saturated phase for linear growth rate  $\gamma = 5.67 \times 10^4 \text{ s}^{-1}$ .

This mode structure modification is not captured by perturbative codes, where the perturbed fields are fixed to the linear mode structure. Mode structure modification is caused by, for instance, fast particle profile relaxation, which changes the position of the peak gradients.

In figure 5.8, time series are plotted depicting the range of frequencies occupied by the mode. Note that the axis are in terms of  $\Omega_*$ , the cyclotron frequency. In this case  $\Omega_* = 2.86735 \times 10^8 \text{ rad s}^{-1}$ , and so a mode frequency of  $4 \times 10^5 \text{ rad s}^{-1}$  corresponds to  $0.001395 \Omega_*$ . In the left hand column, frequency spectra are plotted including FLR effects, and in the right hand column, frequency spectra from corresponding simulations considering only drift kinetics. Both columns descend from lowest to highest fast particle density fraction and therefore mode drive. All of these simulations have been performed with the fluid-electron hybrid model with resistive damping and the points with FLR correspond to those plotted in figure 5.6.

The highest driven modes exhibit an upshift in frequency into the continuum. In the simulations without FLR, two exhibit a characteristic pattern with in which the frequency does not maintain a constant set of values. These frequency spectra differ from those obtained with the perturbative code CKA-EUTERPE, in which the mode structure may not evolve. In particular those simulations exhibit a characteristic downward frequency sweep in the non-linear phase. In the perturbative simulations a clear progression in the frequency time series structure is also seen with increasing growth rate. In this case, however, there appears to be a qualitative difference between patterns obtained in the FLR and no-FLR simulations, and the no-FLR simulations do not show steady, discrete evolution with increasing growth rate.

It is therefore plausible that mode structure modification in the non-linear phase observed with the non-perturbative models may be of significance in stabilising the mode frequency around the linear frequency. It is also plausible that, in this case, FLR effects have qualitatively different influence. Of particular note is that bulk plasma FLR effects are excluded in the perturbative model but present here. Note however that the diagnostic used here may also be insufficient to consider evolving modes with evolving structures as it takes data from a single spatial domain.



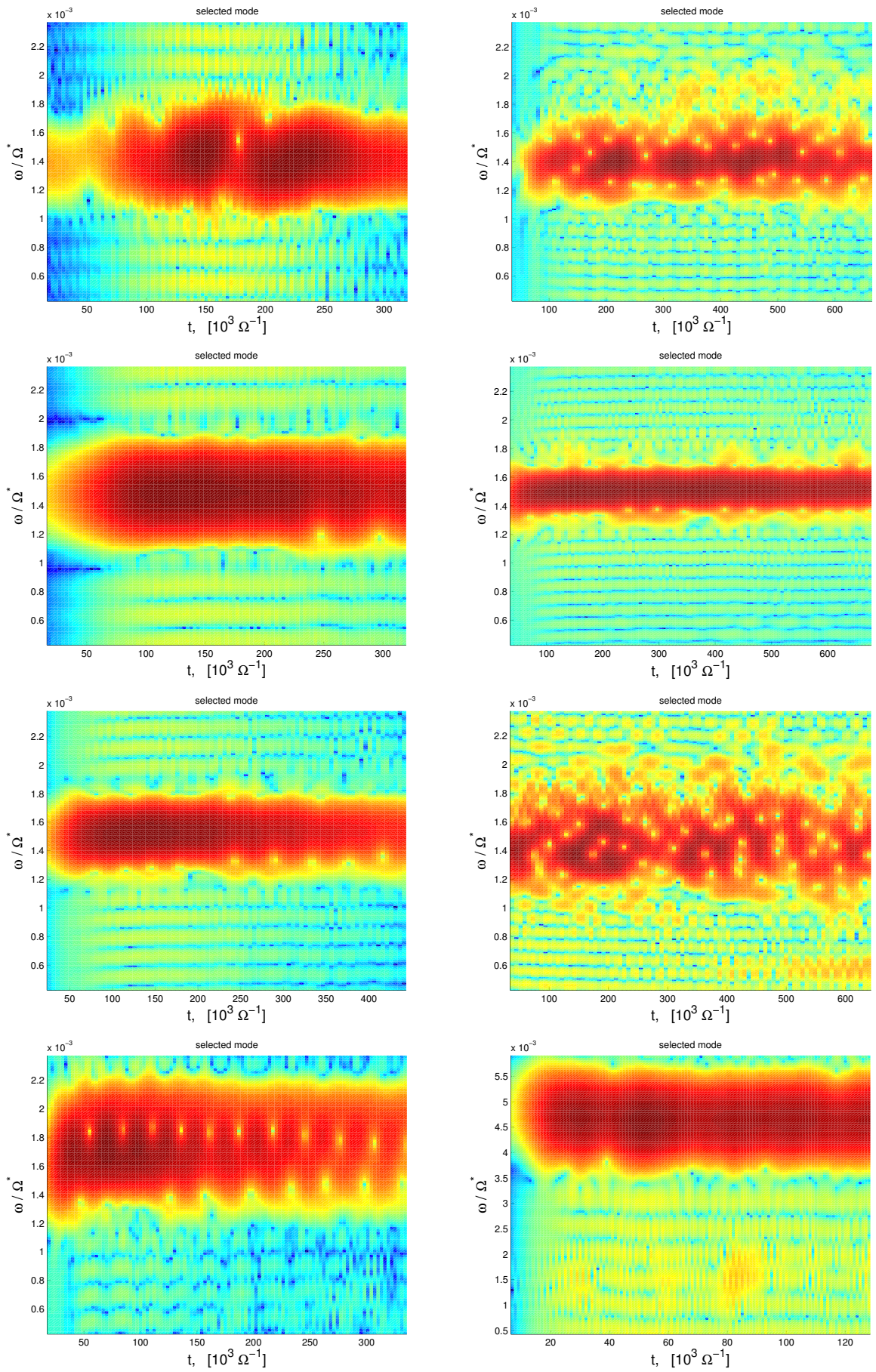


Figure 5.8: Frequency spectra for non-linear fluid-electron hybrid simulations with (left) and without (right) FLR for, from top to bottom,  $\rho_f = 0.5$ ,  $\rho_f = 0.75$ ,  $\rho_f = 1.0$  and  $\rho_f = 2.0$ .

### 5.1.2 Non-linear wave-wave interaction

So far, only a single mode has been considered in the ITPA TAE case, the  $m = 10, 11$ ,  $n = -6$  Toroidal Alfvén Eigenmode. Other TAEs exist in this geometry. Referring again to the condition for the peak of a TAE,

$$q(r) = \frac{m + 0.5}{n}, \quad (5.2)$$

we see that a  $m = 3, 4$ ,  $n = -2$  TAE should also exist at the same  $q$  value, and therefore at the same radial position although at a different frequency, as the TAE mode already considered. This mode in fact has a higher linear growth rate than the  $n = -6$  mode, and therefore in a linear analysis without a restricted filter ought to dominate the system.

In the non-linear regime, however, modes with different poloidal and toroidal mode numbers can interact non-linearly such that the behaviour of the entire system is also affected by the influence of sub-dominant modes. We now use the ITPA TAE case to explore this behaviour.

In order to treat the wave-wave non-linearity, it is necessary to consider non-linear terms in the calculation of the Shear Alfvén Wave mode structure, that is, the collective behaviour of the thermal plasma.

There are different possible approaches to this problem. One is to employ the fully gyrokinetic EUTERPE code to solve the non-linear gyrokinetic equation for all species. This, however, is highly computationally demanding. Another possible approach is to solve non-linear fluid equations for the thermal plasma, which has been pursued by, e.g. HMGC and MEGA [33].

In this section, we consider simulations using the fluid-electron hybrid model in which both fast and thermal ions are treated by solving the non-linear gyrokinetic equation. Bulk plasma non-linearity enters via the bulk ions, while the bulk electrons are treated with a linear fluid description.

We choose the same parameters as in the previous simulations, with fast particle temperature  $T_f = 400$  keV and no resistive damping. The filter is selected to include mode numbers  $3 < m < 14$  and  $-6 < n < -2$ , such that both the  $n = -2$  and  $n = -6$  are retained.

In figure 5.9 (left) we plot the resulting power spectrum in the saturated non-linear phase. It can be seen that from a dominant  $n = -2$  mode in the linear phase, a spectrum of modes emerges following the safety factor profile, including both the  $n = -2$  and  $n = -6$  modes and numerous intermediate mode number modes which exist only in the non-linear phase. Note that non-linear power transfer between the modes results in the  $n = -2$  and  $n = -6$  modes having comparable saturated amplitudes, despite the higher linear growth rate of the  $n = -2$  mode in the linear regime.

A further simulation is performed, this time with the mode numbers  $0 < m < 14$  and  $-6 < n < 0$ , such that the zonal mode  $m = 0$ ,  $n = 0$  is now included. The zonal mode can be particularly important in the non-linear regime. In figure 5.9 (right), we once again plot the power spectrum, this time for a multi-mode simulation including the zonal mode. In this case the zonal mode comes to dominate the power spectrum,



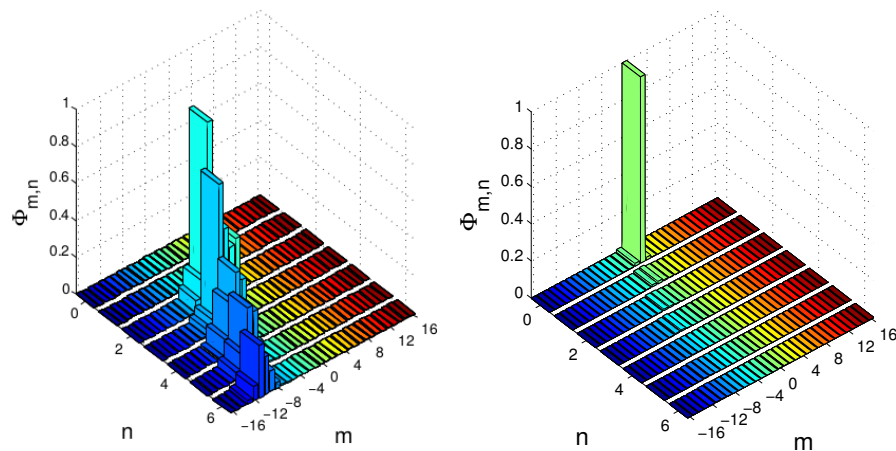


Figure 5.9: The saturated power spectrum for the wave-wave interaction cases without (left) and with (right) consideration of the zonal mode at  $n = 0 = m$ . In the case without zonal coupling, both  $n = -2$  and  $n = -6$  TAEs are visible, along with a line of intermediate modes created by non-linear coupling. In the case with zonal coupling, the zonal mode dominates, but note that the same line of coupled modes is barely visible in this case too.

although the string of coupled modes with alignment determined by the safety factor profile can still barely be seen at a much lower amplitude.

In figure 5.10, poloidal cross-sections are plotted depicting the electrostatic potential perturbations for each of these cases in the linear and non-linear phases respectively. In the linear phase, there is a noticeable difference between the single and multimode simulations, as the harmonic structure is modified by the influence of the small  $n = -6$  contribution. As its linear growth rate is lower than that of the  $n = -2$  TAE, its influence diminishes in the course of the simulation. Both multimode simulations, in the absence of non-linear coupling, appear similar at this stage.

Later, however, there appears a very significant difference between the saturated structure of the perturbed potential in each simulation. While the single mode remains clear and similar in structure to its linear phase, the multimode simulations appear radically different, with individual modes no longer clearly distinct and in the case where the zonal mode is included it dominates all other activity.

In figure 5.11 is plotted the evolution of the ratio of the maximum magnetic field perturbation to the background field strength compared for the lone  $n = -6$  and  $n = -2$  modes, and both multimode simulation setups. The saturation amplitude progressively reduces as greater coupling is included, being highest for the single mode and lowest for the simulation with coupling between multiple modes and the zonal mode. Both coupled mode simulations show a lower saturated perturbation amplitude than either single mode simulation.

It is also noteworthy that the perturbed magnetic field amplitude saturates cleanly in both multimode cases without an applied resistive damping, which is not included in any simulations presented here. In the case where only wave-particle interaction is considered there is once again observed a constant sub-exponential upward drift in the

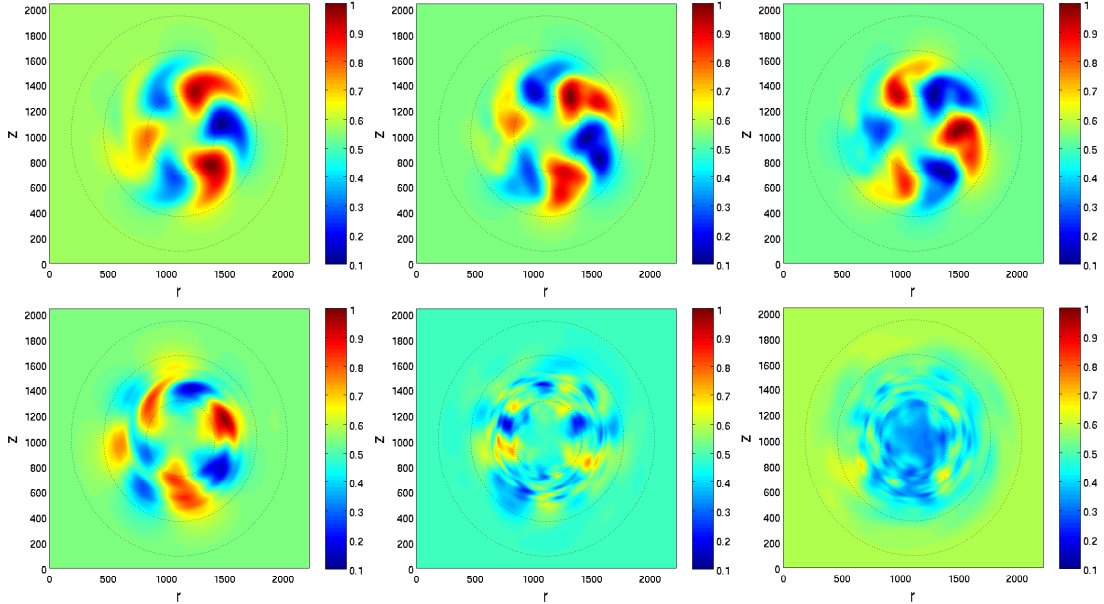


Figure 5.10: Plots of the perturbed electrostatic potential in a poloidal cross-section through the torus in the linear (above) and non-linear (below) phases for, from left to right, the single mode  $n = -2$  simulation, the multimode simulation without zonal mode, and the multimode simulation with zonal mode. Note that the single  $n = -2$  mode saturates at a higher amplitude than the  $n = -6$  mode; both single modes, however, saturate at a higher level than either coupled system.

magnetic field perturbation amplitude. In a realistic multimode simulation, therefore, it should be unnecessary to apply an artificial damping in order to obtain a result. Since artificial damping would also contaminate that result, this behaviour is desirable.

These simulations therefore demonstrate that a single-mode treatment can overstate the extent to which a TAE may perturb the background magnetic field in comparison with a more complete multimode treatment, and therefore the magnitude of transport of particles and energy for which it may be responsible. Multimode simulations including wave-wave interaction will therefore be necessary to produce transport predictions for experimental cases.

So far, detailed multimode non-linear simulations have been performed only with perturbative codes, such as HAGIS [48, 49]. Such codes do not self-consistently consider non-linear effects in the thermal plasma. It is therefore proposed that such simulations be repeated with codes capable of treating self-consistent wave-wave non-linear physics.

Such work is of immediate interest predicting the likely effects of fast particle physics in large reactors such as ITER and DEMO, as well as a prospective stellarator reactor, since these machines will have relatively large fast particle concentrations. Such predictions are necessary both in order to assess the suitability of different possible designs and also to tailor operational scenarios in which the device may be safely operated and with optimal fusion power output.

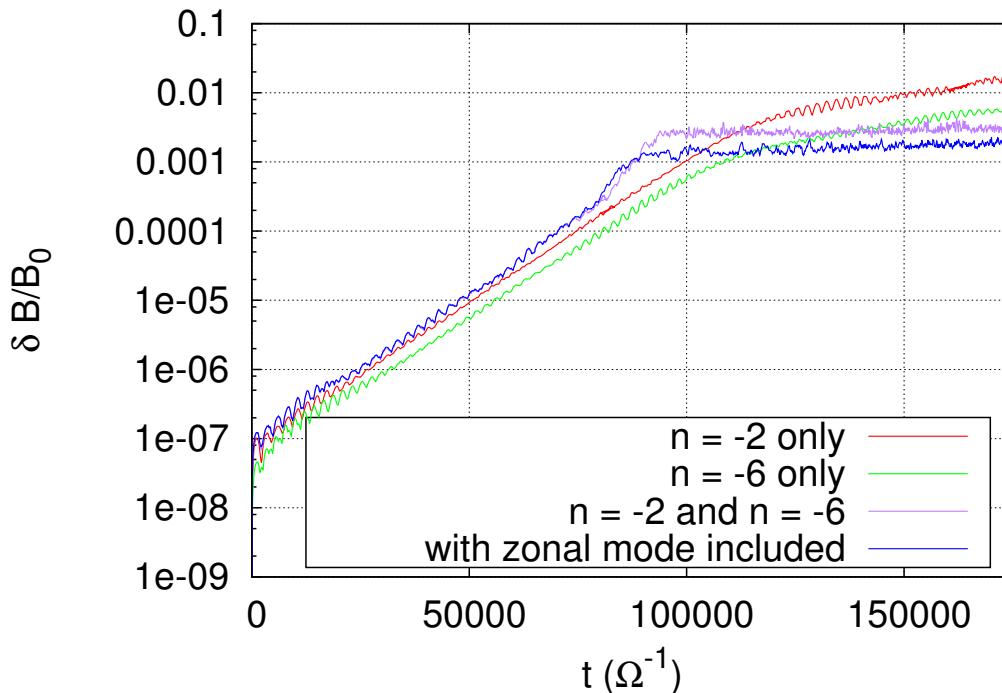


Figure 5.11: The evolution of the magnetic field perturbation. One can compare saturation levels for simulation of a single mode (red),  $2 < n < 6$  (pink), and  $0 < n < 6$  (blue), in the absence of resistive damping. Greater coupling is associated with progressively strong damping of the saturated amplitude. For comparison, the perturbed magnetic field evolution is plotted for the single modes corresponding to  $n = -2$  (red) and  $n = -6$  (green).

## 5.2 Fishbone instability

The fishbone instability is based on the  $m = 1$  EPM. The term ‘fishbone’ refers to characteristic experimental measurements in which strong frequency chirping led to frequency time traces resembling a fishbone. This chirping behaviour is fundamentally non-linear and the fishbone instability is therefore a non-linear phenomenon.

In this work, the full non-linear physics of the fishbone mode cannot yet be treated, as it depends upon both non-linear wave-particle interaction and the non-linear wave-wave interaction of the bulk plasma. In particular, the  $m = 1$  kink mode is an independent fluid instability, which will not reach saturation without considering fluid non-linearities. Absent such a saturation mechanism, it will eventually overcome a saturated  $m = 1$  EPM.

It is, however, possible to consider the non-linear wave-particle interaction alone, and thereby illustrate some key features of the non-linear instability. In this section, such a non-linear extension of the preceding work will be presented.

Taking the same geometry as in section 4.6, we compare the evolution of the perturbed magnetic field as a ratio of the equilibrium magnetic field,  $\delta B/B_0$ . In figure 5.12,

a time trace is plotted for the above cases corresponding to  $\rho_f = 0.04$  and  $\rho_f = 0.01$ , i.e. to the modes we have previously identified as the  $m = 1$  EPM and the internal kink mode respectively.

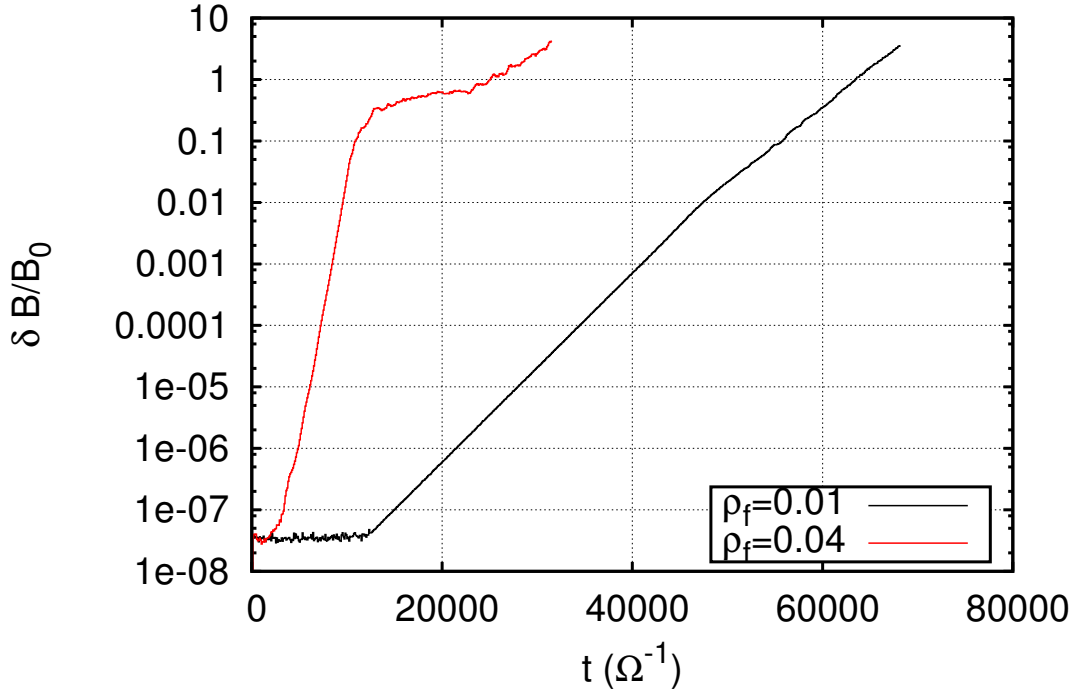


Figure 5.12: Time traces of the evolution of the perturbed magnetic field strength as a ratio of the equilibrium field strength,  $\delta B/B_0$ , for two cases:  $\rho_f = 0.04$  (red) and  $\rho_f = 0.01$  (black), corresponding to the  $m = 1$  EPM and the  $m = 1$  internal kink mode respectively.

The most striking difference is that the  $m = 1$  EPM time trace shows a non-linear saturated stage, during which the magnetic field perturbation ceases to grow exponentially and levels-off at a constant value. The internal kink mode does not demonstrate this behaviour. This is anticipated, as the internal kink mode is driven unstable by the bulk plasma current and pressure, not by the gyrokinetic energetic particle population.

It is also noteworthy, however, that the  $m = 1$  EPM time trace exits the saturated stage at a later time, and resumes exponential growth. Since the internal kink and  $m = 1$  EPMS are fundamentally separate modes, it is anticipated that in the  $m = 1$  EPM cases internal kink modes continue to grow sub-dominantly but are obscured by the faster growing EPMS. Since the saturation mechanisms apply to the EPM but not the internal kink, the saturated EPM eventually gives way to the unsaturated linear internal kink.

These characteristics of the numerical results therefore reinforce the conclusion that there is a true transition from an ideal MHD eigenmode to an energetic particle mode resulting from the inherently kinetic interaction of the fast particle population with

the bulk plasma.

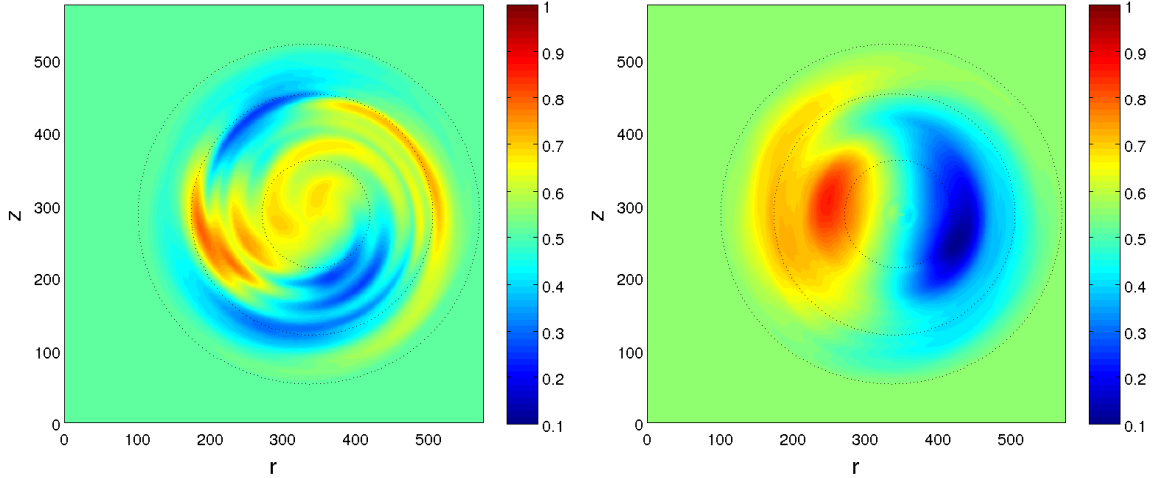


Figure 5.13: Poloidal cross-sections of the perturbed electrostatic potential for the saturated  $m = 1$  EPM case a short time into the saturated phase (left) and deep in the saturated phase (right). Comparing these plots to those of the linear  $m = 1$  modes in figure 4.16, the resemblance to the linear internal kink mode in the latter case is clear.

In figure 5.13, the mode structure in the saturated non-linear phase is plotted. It can be seen that at late simulation time, when exponential growth has resumed, the mode structure resembles that of the damped internal kink case from figure 4.16. This suggests that the low growth rate internal kink mode has in fact re-emerged. At lower time, at the beginning of the saturated phase, we see the modification of the mode structure of the  $m = 1$  EPM itself. Although the basic  $m = 1$  and  $m = 2$  structure remains visible, finer structure emerges radially.

As discussed in section 2.2, it is possible to extend the fluid model of the thermal plasma to include fluid non-linearities. Longer time simulations, and ultimately experimental comparison and prediction, involving the fishbone mode would then become possible. Simulations with the fully gyrokinetic model, or with the fluid-electron hybrid model, can also be pursued which could take account of the fluid non-linearity through the non-linear gyrokinetic equation, which reduces to the fluid equations in the appropriate limits.

### 5.3 Non-linear stellarator

Taking the successful linear W7-X global mode case from section 4.7, we attempt a proof of principle non-linear simulation in the optimised stellarator geometry. Here, only the wave-particle interaction is treated non-linearly and the FLU-EUTERPE model is used, the bulk plasma being treated as a fluid.

In figure 5.14 (left) the evolution of the magnetic field perturbation for the  $\rho_f = 0.05$  case is plotted. A clean linear phase followed by a non-linear saturated phase are visible.

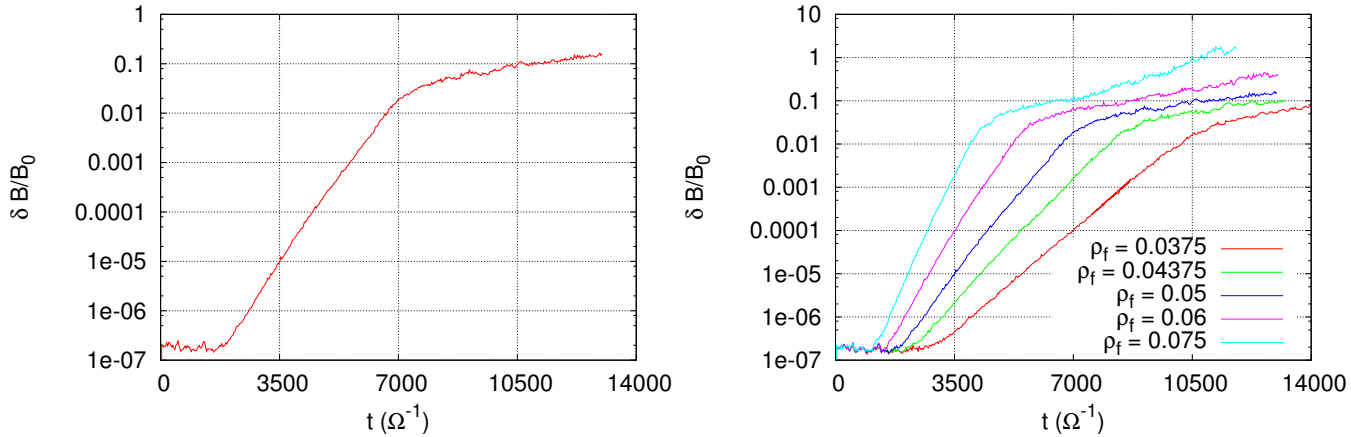


Figure 5.14: Left: the evolution of the ratio of the maximum perturbed magnetic potential to the equilibrium magnetic field for the global mode in Wendelstein 7-X with  $\rho_f = 0.05$ . As in the tokamak case, a clean linear growth phase can be distinguished from a non-linear saturation phase. Right: comparison of the evolution and saturation of the perturbed magnetic field for several values of  $\rho_f$ , between 0.0375 and 0.075.

The saturated perturbed magnetic field amplitude is very high, at order  $\delta B/B_0 \sim 10^{-2}$ , which in a fusion experiment would be deleterious for the plasma performance. In this case, however, it is most likely an artefact of the very high fast particle normalised pressure,  $\beta_f$ , which is much greater than in even a reactor.

In figure 5.15, the linear and non-linear mode structures are plotted in comparison, in terms of the variation of the perturbed electrostatic potential in a cross-section through the device. Note that in this simulation there is a large Fourier filter that does not exclude the zonal mode, which becomes important.

This result shows that the stellarator geometry does not present a fundamental numerical obstacle to the performance of non-linear hybrid simulations. Ultimately, then, it should be possible to produce saturated transport predictions for global modes in stellarators using the hybrid models. In future work, the wave-wave interaction may also be considered in stellarators.

As a first exploitation of this new capability, we consider the relationship between the saturated magnetic field amplitude and the linear growth rate in the above case for a range of fast particle densities. Again we consider only the wave-particle non-linearly here. In figure 5.14 (right), time traces for the evolution of the perturbed magnetic field are presented for a range of linear growth rates. The fast particle density is varied between 3.75% and 7.5% of the thermal electron density.

The qualitative difference in growth rate can be easily inferred from figure 5.14 (right). Those modes with higher fast particle drive and therefore higher growth rate saturate sooner. This corresponds to no significant difference in the level at which each saturates, when compared at the same time into the saturated phase.

The relative constancy of the saturated amplitude may be consistent with the trend

observed in the tokamak case. Referring back to figure 5.6, it can be seen that the saturated perturbation amplitude increases more slowly with linear growth rate as the two increase to higher values. As the amplitudes in this stellarator case are between one and two orders of magnitude larger than the largest in that comparison, it is plausible that the results obtained in this stellarator case are consistent with the continuation of this already observed trend.

A precise quantitative comparison is not possible because the undamped single modes drift in perturbed amplitude after saturation, as already shown in the simple tokamak case in figure 5.1. By including resistive effects, this would be possible. This could be compared with the tokamak results at comparably high growth rates. However, it may be more interesting to consider more realistic parameters. Note that in the highest growth rate case where  $\rho_f = 0.075$ , the time trace drifts up close to  $\delta B/B_0 = 1$ , and the simulation fails as the ordering assumptions of the numerical model have been violated.

This study nonetheless demonstrates the feasibility of the tool for non-linear physics investigations in stellarator geometry, and illustrates that many of the same basic features are present as have already been founded in tokamak studies. Meanwhile, the evidence of substantial mode structure modification in the saturated non-linear phase suggests the importance of a non-perturbative approach.

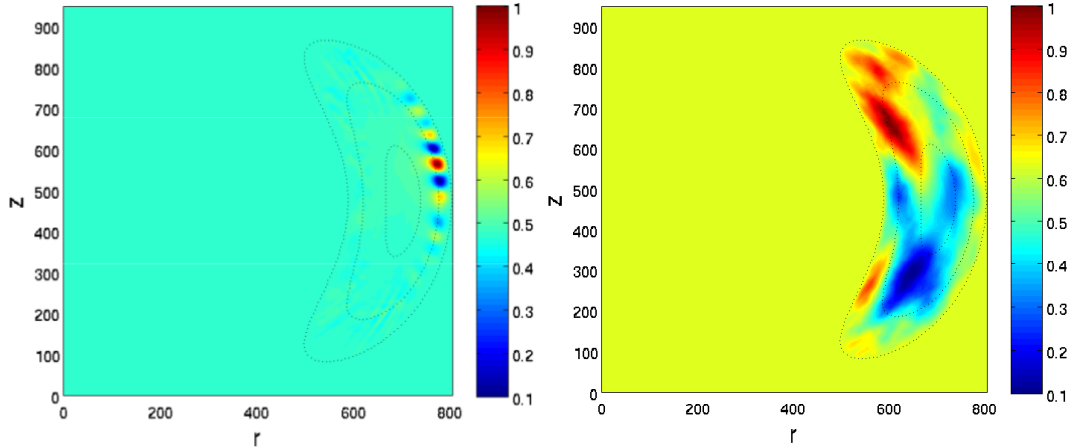


Figure 5.15: The perturbed electrostatic potential plotted in a cross-section through the device for the linear (left) and non-linear (right) phases of evolution of the global mode in W7-X.

# Chapter 6

## Conclusions

### 6.1 Key results

The overarching purpose of this work has been to expand the range of physical parameters for global modelling of magnetically confined fusion plasmas by development and utilisation of the EUTERPE code. Important limitations to such simulations have included the ‘cancellation problem’, which affected simulations in the MHD regime where  $k_{\perp}\rho_i \rightarrow 0$ . A further important limitation was that non-linear simulations had not been attempted in some regimes with the EUTEPRE code and, with some models, at all. In this work, both aspects have been addressed, with a particular but not exclusive emphasis on fast particle interaction with global modes.

The cancellation problem, and other numerical limitations, have been addressed in two ways. First, two simplified self-consistent fluid-kinetic hybrid models have been implemented for the code, both with and without thermal ion gyrokinetic effects. Second, an improved numerical scheme, developed by Mishchenko and co-workers [80, 81], has been explored and exploited.

The fluid models have been extensively benchmarked. It has been shown that:

- Linear growth rates and mode frequencies for a Toroidal Alfvén Eigenmode in a circular tokamak benchmark case agree with those found using a range of other codes, from perturbative hybrid models to self-consistent fully gyrokinetic codes. This case can be generalised to more realistic geometry including elongation, demonstrating reduction in the linear growth rate with increasing elongation.
- Linear growth rates and mode frequencies diverge in a more complicated case where gyrokinetic thermal ion, and finite  $E_{\parallel}$ , effects become important. The self-consistent non-perturbative hybrid models show better agreement with the fully gyrokinetic model than previous simulations performed with a perturbative hybrid model.
- Simulations are possible using both hybrid fluid-electron and fluid bulk plasma models in the deep MHD ( $k_{\perp}\rho_i \rightarrow 0$ ) regime, such as the  $m = 1$  internal kink mode. An EPM branch of this mode - the linear stage of the fishbone instability - has been simulated in the presence of a fast particle population, which cannot



be done with fixed mode structure perturbative codes. Non-linear saturation of the EPM has also been demonstrated using this model.

- In non-axisymmetric stellarator geometry, it has been shown that simulations of linear wave-particle interaction are possible and a scan has been performed in fast particle density for a mode identified in the strongly shaped Wendelstein 7-X stellarator geometry.
- Non-linear simulations resulting in saturated field perturbations are possible in both tokamak and strongly shaped stellarator geometries. In the tokamak case, the saturated levels have been benchmarked successfully against other perturbative and non-perturbative hybrid codes. Mode structure modification in the non-linear phase has been observed with the self-consistent models.
- When non-linear wave-wave interaction is considered in a simple TAE case, qualitatively different behaviour is observed and the quantitative saturated perturbation amplitude is seen to be significantly reduced. Both coupling to other TAE modes and to the zonal mode have been shown to have significance in determining the saturated amplitude. When the wave-wave non-linear interaction between two TAE modes is considered the final saturated perturbation amplitude is found to be lower than that of either of the modes considered separately. Inclusion of the zonal mode results in a further decreased saturated amplitude.

We may therefore apply the hybrid models with good confidence for a wide range of device parameters and geometries, including some regimes where fully gyrokinetic electromagnetic PIC currently performs poorly or is incapable of yielding results. Limitations have been encountered simulating modes in stellarator geometry close to marginal stability. In Wendelstein 7-X these limitations begin while the normalised fast particle pressure  $\beta_f$  is still comparable to the normalised bulk plasma pressure.

Improvements to the electromagnetic gyrokinetic PIC method, which were not developed as part of this thesis, have been utilised in some situations for the first time here. Key results in this respect include:

- All previous linear benchmark cases, such as the linear ITPA TAE case with and without elongation, have been reproduced using the new scheme, yielding good agreement.
- The first nonlinear, global, electromagnetic, fully gyrokinetic simulations of Toroidal Alfvén Eigenmodes, reproducing a trend predicted by analytical theory and confirmed by the hybrid models. The inclusion of electron kinetic effects does not seem to be significant in this case.
- The first linear global, electromagnetic, fully gyrokinetic simulations of fast particle-driven modes in optimised stellarator geometry, such as that of Wendelstein 7-X, have been performed in the same parameter regime as those considered with the hybrid models and substantially verified by comparison with the hybrid models. A significantly lower mode growth rate is observed suggesting that bulk plasma

damping mechanisms such as ion Landau damping may be important in the Wendelstein 7-X operational regime.

Compared to the previous fully gyrokinetic scheme in the standard ITPA TAE reference case the new gyrokinetic scheme was found to be at least two orders of magnitude more computationally efficient. The fluid hybrid models were found to be about an order of magnitude more computationally efficient again. Time step and CPU-hour requirements have been relaxed for instance by eliminating the need to resolve the fast electron motion. A more modest speed-up was observed between the fluid-electron hybrid model and the fluid bulk plasma hybrid model.

The fully gyrokinetic and hybrid models have both been demonstrated to be capable of demonstrating non-linear saturation in both tokamak and stellarator geometry, which in principle permits the calculation of saturated energy and particle transport due to global modes, the ultimate goal of work in this area.

## 6.2 Outlook

Since the ultimate goal of this line of modelling work is to predict the behaviour of energetic particle driven modes in current and future stellarators, necessary improvements to the physical model and numerical treatment will be considered.

One significant omission in the current models is collisionality. Although high temperature plasmas in the core of a fusion device are very nearly collisionless, the collisionality reducing with temperature as  $\nu \sim T^{-3/2}$ , a damping mechanism has been shown to be important in determining the saturated amplitude of a field perturbations due to an unstable mode. EUTERPE contains a pitch angle scattering collision operator, while remains to be benchmarked and exploited for modelling the physics of global modes.

Another interesting area of exploration, which has been touched upon in this thesis, is the self-consistent non-linear interaction of multiple modes. Since many modes will likely coexist in a reactor, and their interaction is important in determining the final net transport, the self-consistent models developed and exploited in this thesis are ideally placed to investigate such effects. It has already been demonstrated in this and other work that consideration of non-linear wave-wave interaction can significantly affect the final saturated perturbed field amplitude. Such investigations should also be repeated and verified using the fully gyrokinetic model.

Since EUTERPE is currently the only electromagnetic gyrokinetic code capable of performing fully global electromagnetic gyrokinetic simulations in stellarator geometry, it would be particularly sensible for the code to be used as a support for Wendelstein 7-X experiments. Code predictions can be benchmarked against the experimental measurements and can then be used to help explain experimental measurements and also to provide fast particle transport predictions for future reactor and stellarator optimisation concepts.

Owing to the complexity of the task, and the fact that Wendelstein 7-X is yet to enter full operation at the time of writing, much of this detailed work remains ahead. It will be particularly important to improve the numerical treatment such that

simulations become possible closer to marginal stability. The groundwork, however, has been laid in this thesis.

One hypothesis of potentially great significance is that, in the absence of the Greenwald density limit in a stellarator, operation may be possible at sufficiently high densities that fast particles are rapidly thermalised to the point that their excitation of Alfvénic modes in a stellarator reactor may be unimportant for fast particle transport.

The careful consideration of realistic distribution functions, combined with simulation near marginal stability will be necessary to approach this question using the tools that have been developed in this work. Confirmation of this hypothesis would reveal a significant advantage of the stellarator design, while falsification would highlight the importance of simulation and experimental work with respect to fast particle physics in order to realise a working stellarator reactor.

The tool that has been developed allows deep future exploitation. In addition to those physical processes so far considered, the model can be extended to include drift wave physics. This will permit the simulation of gradient-driven turbulence, and ultimately the consideration of the interaction between global Alfvénic modes and turbulence. Thus far a full understanding of non-linear mode-mode interaction between Alfvén waves remains elusive.

Further improvements to the diagnostics are also envisioned. For instance, extensive work by Briguglio and co-workers to produce a phase space diagnostic for non-linear simulations will be implemented and used to better understand the fully non-linear results obtained in the course of this work.

# Bibliography

- [1] J.-L. Dufresne *et al.*, *Clim. Dynam.* **40**, 2123 (2013).
- [2] J. Lindl *et al.*, *Phys. Plasmas* **21**, 020501 (2014).
- [3] R. J. Goldston and P. H. Rutherford, *Introduction to Plasma Physics* (Taylor & Francis Group, Abingdon, Oxon, 1995).
- [4] A. Herrmann and O. Gruber, *Fusion Sci. Technology* **44**, 569 (2003).
- [5] A. Gibson and JET-Team, *Phys. Plasmas* **5**, 1839 (1998).
- [6] M. Shimada *et al.*, *Nucl. Fusion* **47**, 099801 (2007).
- [7] G. Federicia *et al.*, *Fusion Engineering and Design* **89**, 882 (2014).
- [8] F. Wagner *et al.*, 19th IAEA FEC, Lyon. (2002).
- [9] O. Motojima *et al.*, *Nucl. Fusion* **43**, 1674 (2003).
- [10] R. O. Wolf *et al.*, *Plasma Fusion Res.* **5**, S1011 (2010).
- [11] C. Beidler *et al.*, *Nucl. Fusion* **41**, 1759 (2001).
- [12] Y. Igitkhanov *et al.*, *Fusion Design and Engineering* **81**, 26952702 (2006).
- [13] H. Alfvén, *Nature* **150**, 3805 (1942).
- [14] W. W. Heidbrink, *Phys. Plasmas* **15**, 055501 (2008).
- [15] B. N. Breizman and S. E. Sharapov, *Plasma Phys. Control. Fusion* **53**, 054001 (2011).
- [16] A. B. Mikhailovskii, *Sov. Phys. JETP* **41**, 890 (1975).
- [17] M. N. Rosenbluth and P. H. Rutherford, *Phys. Rev. Lett.* **34**, 1428 (1975).
- [18] Y. I. Kolesnichenko, V. V. Lutsenko, and Y. V. Yakovenko, *Alfvén Eigenmodes in Helias Configurations, Part 2* (Max-Planck-Institut für Plasmaphysik, Garching bei München, 2002).
- [19] R. R. Mett and S. M. Mahajan, *Phys. Fluids B* **4**, 2885 (1992).

- [20] A. B. Mikhailovskii and I. G. Shukhman, *Sov. Phys. JETP*. **44**, 952 (1976).
- [21] N. N. Gorelenkov and S. E. Sharapov, *Physica Scripta* **45**, 163 (1992).
- [22] H. L. Berk, B. N. Breizman, and H. Ye, *Phys. Rev. Lett.* **68**, 3563 (1992).
- [23] H. L. Berk, B. N. Breizman, and M. Pekker, *Phys. Rev. Lett.* **76**, 1256 (1996).
- [24] K. L. Wong *et al.*, *Phys. Plasmas* **4**, 393 (1997).
- [25] K. L. Wong, *Plasma Phys. Control. Fusion* **41**, R1 (1999).
- [26] R. G. L. Vann *et al.*, *Phys. Plasmas* **10**, 623 (2003).
- [27] H. L. Berk *et al.*, *Phys. Plasmas* **6**, 3102 (1999).
- [28] A. Fasoli *et al.*, *Phys. Rev. Lett.* **81**, 5564 (1998).
- [29] R. F. Heeter, A. F. Fasoli, and S. E. Sharapov, *Phys. Rev. Lett.* **85**, 3177 (2000).
- [30] S. D. Pinches *et al.*, *Plasma Phys. Control. Fusion* **46**, S47 (2004).
- [31] R. G. L. Vann, R. O. Dendy, and M. P. Gryaznevich, *Phys. Plasmas* **12**, 032501 (2005).
- [32] M. P. Gryaznevich and S. E. Sharapov, *Nucl. Fusion* **46**, S942 (2006).
- [33] Y. Todo, M. A. V. Zeeland, A. Bierwage, and W. W. Heidbrink, *Nucl. Fusion* **54**, 4012 (2014).
- [34] K. L. Wong *et al.*, *Phys. Rev. Lett.* **93**, 5002 (2004).
- [35] M. A. V. Zeeland *et al.*, *Plasma Phys. Control. Fusion* **50**, 5009 (2008).
- [36] P. Helander, *Rep. Prog. Phys.* **77**, 087001 (2014).
- [37] R. C. Wolf *et al.*, *Proceedings of the 18th International Toki Conference* (2008).
- [38] K. L. Wong *et al.*, *Phys. Rev. Lett.* **66**, 1874 (1991).
- [39] A. Weller *et al.*, *Phys. Rev. Lett* **72**, 1220 (1994).
- [40] A. Weller *et al.*, *Phys. Plasmas* **8**, 931 (2001).
- [41] K. Toi, S. Ohdachi, S. Yamamoto, and et al., *Nucl. Fusion* **44**, 931 (2001).
- [42] M. Osakabe *et al.*, *Nucl. Fusion* **46**, S911 (2006).
- [43] R. B. White, *The Theory of Toroidally Confined Plasmas* (Imperial College Press, London, SW2H 9HE, UK, 2001).
- [44] R. B. White, P. H. Rutherford, P. Colestock, and M. N. Bussac, *Phys Rev. Lett.* **60**, 2038 (1998).

- [45] K. Ichiguchi *et al.*, Nucl. Fusion **33**, 481 (2005).
- [46] E. M. Bass and R. E. Waltz, Phys. Plasmas **17**, 112319 (2010).
- [47] S. D. Pinches *et al.*, Comput. Phys. Commu. **111**, 133 (1998).
- [48] M. Schneller *et al.*, J. Phys.: Conf. Ser. **401**, 012022 (2012).
- [49] M. Schneller, P. Lauber, and S. Briguglio, Plasma Phys. Control. Fusion **58**, 014019 (2015).
- [50] P. Lauber, S. Günter, A. Könies, and S. D. Pinches, J. Comput. Physics **226**, 447 (2007).
- [51] T. Fehér, *Simulation of the interaction between Alfvén waves and fast particles* (Universität Greifswald, Germany, 2014).
- [52] D. Borba and W. Kerner, J. Comput. Phys. **153**, 101 (1999).
- [53] N. N. Gorelenkov, C. Z. Cheng, and G. Y. Fu, J. Comput. Physics **6**, 2802 (1999).
- [54] A. Könies, A. Mishchenko, and R. Hatzky, Theory of Fusion Plasmas 133 (2008).
- [55] D. Spong, E. D’Azevedo, and Y. Todo, Contr. Plasma Phys. **50**, 708 (2010).
- [56] W. A. Cooper, Plasma Phys. Control. Fusion **53**, 024001 (2011).
- [57] S. Briguglio, G. Vlad, F. Zonca, and C. Kar, Phys. Plasmas **2**, 3711 (1995).
- [58] Y. Todo and T. Sato, Phys. Plasmas **5**, 1321 (1998).
- [59] G. Y. Fu *et al.*, Phys. Plasmas **13**, 2517 (2006).
- [60] Y. Chen and S. Parker, Phys. Plasmas **8**, 441 (2000).
- [61] Z. Lin and L. Chen, Phys. Plasmas **8**, 1447 (2001).
- [62] H. Qin, *Gyrokinetic Theory and Computational Methods for Electromagnetic Perturbations in Tokamaks* (Princeton University, USA, 1998).
- [63] S. Jolliet *et al.*, Comput. Phys. Commun. **117**, 409 (2007).
- [64] A. Bottino *et al.*, IEEE Trans. Plasma Sci. **38**, 2129 (2010).
- [65] A. Bottino *et al.*, Plasma Phys. Control. Fusion **53**, 124027 (2011).
- [66] A. Mishchenko, A. Könies, and R. Hatzky, Phys. Plasmas **16**, 082105 (2009).
- [67] A. Mishchenko and A. Zocco, Phys. Plasmas **19**, 122104 (2012).
- [68] A. Mishchenko, A. Könies, and R. Hatzky, Phys. Plasmas **21**, 052114 (2014).
- [69] G. Jost *et al.*, Phys. Plasmas **8**, 3321 (2001).

- [70] V. Kornilov *et al.*, Phys. Plasmas **11**, 3196 (2004).
- [71] O. Zacharias, R. Kleiber, and R. Hatzky, J. Phys.: Conf. Ser. **401**, 012026 (2015).
- [72] W. A. Hornsby *et al.*, Phys. Plasmas **22**, 022118 (2015).
- [73] W. A. Hornsby *et al.*, Plasma Phys. Control. Fusion **58**, 014028 (2016).
- [74] P. Helander *et al.*, Nucl. Fusion **55**, 053030 (2015).
- [75] K. Kaufmann, *Including Collisions in Gyrokinetic Tokamak and Stellarator Simulations* (Universität Greifswald, Germany, 2012).
- [76] J. M. Garcia-Regana *et al.*, Plasma Phys. Control. Fusion **55**, 074008 (2013).
- [77] M. A. Pedrosa *et al.*, Nucl. Fusion **55**, 052001 (2015).
- [78] O. Zacharias, R. Kleiber, and R. Hatzky, J. Phys.: Conf. Ser. **401**, 012026 (2012).
- [79] O. Zacharias *et al.*, Phys. Plasmas **21**, 062106 (2014).
- [80] A. Mishchenko, M. Cole, R. Kleiber, and A. Könies, Phys. Plasmas **21**, 052113 (2014).
- [81] A. Mishchenko, A. Könies, R. Kleiber, and M. Cole, Phys. Plasmas **21**, 092110 (2014).
- [82] A. Mishchenko *et al.*, Nucl. Fusion **54**, 104003 (2014).
- [83] M. D. J. Cole *et al.*, Phys. Plasmas **21**, 072123 (2014).
- [84] M. D. J. Cole *et al.*, Plasma Phys. Control. Fusion **57**, 054013 (2015).
- [85] M. D. J. Cole, Nucl. Fusion (*In preparation*).
- [86] E. A. Frieman and L. Chen, Phys. Fluids **25**, 502 (1982).
- [87] A. J. Brizard and T. S. Hahm, Rev. Mod. Phys. **79**, 421 (2007).
- [88] H. Flanders, *Differential Forms with Applications to the Physical Sciences* (Dover, New York, 1989).
- [89] S. E. Parker, Y. Chen, and C. C. Kim, Comput. Phys. Commun. **127**, 59 (2000).
- [90] Y. Chen and S. E. Parker, Phys. Plasmas **8**, 441 (2000).
- [91] Z. Lin and L. Chen, Phys. Plasmas Lett. **8**, 1447 (2001).
- [92] G. W. Hammett and F. W. Perkins, Phys. Rev. Lett. **64**, 3019 (1990).
- [93] B. D. Scott, Plasma Phys. Control. Fusion **45**, (2003).
- [94] D. A. Spong, B. A. Carreras, and C. L. Hedrick, Phys. Fluids B **4**, (1992).

- [95] G. Jost, T. M. Tran, W. Cooper, and K. Appert, *Phys. Plasmas* **8**, 3321 (2001).
- [96] V. Kornilov *et al.*, *Phys. Plasmas* **11**, 3196 (2004).
- [97] W. M. Nevins *et al.*, *Phys. Plasmas* **12**, 122305 (2005).
- [98] S. P. Hirschman and J. C. Whitson, *Phys. Fluids* **26**, 3553 (1983).
- [99] S. P. Hirschman, W. I. van Rij, and P. Merkel, *Comp. Phys. Comm.* **43**, 143 (1986).
- [100] R. Hatzky *et al.*, 14th European Fusion Theory Conference (2011).
- [101] R. Hatzky, A. Könies, and A. Mishchenko, Proceedings of the Joint Varenna-Lausanne International Workshop 13 (2004).
- [102] R. Hatzky, A. Könies, and A. Mishchenko, *J. Comp. Phys.* **225**, 568 (2007).
- [103] J. C. Cummings, *Gyrokinetic Simulation of Finite-beta and Self-generated Sheared-flow Effects on Pressure-gradient-driven Instabilities* (Princeton University, United States, 1995).
- [104] R. Kleiber *et al.*, *Phys. Plasmas* **23**, 032501 (2016).
- [105] A. Könies *et al.*, Proceedings of the 24th IAEA Fusion Energy Conference ITR/P1 (2012).
- [106] L. Chen, *Phys. Plasmas* **1**, 1519 (1994).
- [107] E. Sánchez *et al.*, *IEEE T. Plasma* **38**, 2119 (2010).
- [108] P. Lauber, *Linear Gyrokinetic Description of Fast Particle Effects on the MHD Stability in Tokamaks* (Technische Universität München, Germany, 2003).
- [109] M. N. Bussac, R. Pellat, D. Edery, and J. L. Soule, *Phys. Rev. Lett.* **35**, 1638 (1975).
- [110] C. Wahlberg, *Phys. Plasmas* **11**, 2119 (2004).
- [111] C. Wahlberg, *Phys. Plasmas* **14**, 042506 (2007).
- [112] A. Bondeson and M.-N. Bussac, *Nucl. Fusion* **32**, 513 (1992).
- [113] P. Helander and M. Lisak, *J. Plasma Physics* **47**, 281 (1992).
- [114] A. Biancalani, Private communication .
- [115] S. Briguglio, Private communication .
- [116] Y. Todo, Private communication .
- [117] M. Isaev, Private communication .
- [118] A. Könies, Private communication .





# Curriculum Vitae and Publications

**Michael David John Cole**

Date of birth 15th April 1990  
Place of birth Bristol, United Kingdom  
Nationality British  
Email mcole@ipp.mpg.de

## **Education and work experience**

2013-2016 Doktorand in Physics, Max-Planck-Institut für Plasmaphysik,  
Greifswald, Germany  
Supervisor: Prof. Dr. Per Helander  
Advisor: Dr. Alexey Mishchenko

2012 Summer student, Culham Centre for Fusion Energy,  
Oxfordshire, United Kingdom  
Supervisor: Dr. Sarah Newton

2009 Royal Society Summer Science Exhibition  
Exhibitor assistant  
Quantum Photovoltaics Group, Imperial College London

2008-2012 MSci in Physics, Imperial College London  
First-class honours

Thesis topic: *Electromagnetic effects in suppression of ITG turbulence by sheared flow*

Supervisor: Professor Steven Cowley  
Advisor: Dr. Michael Coppins

2006 Intern, Airbus UK  
Filton Low Speed Wind Tunnel Facility

2001-2008 Queen Elizabeth's Hospital, Bristol  
4 A levels at grade A in Mathematics, Physics, Chemistry and Biology

10 GCSEs in Mathematics, Physics, Chemistry, Biology, English Language, EN

### Memberships and certificates

Associate of the Royal College of Science

Member of the Deutsche Physikalische Gesellschaft

telc Deutsch B2, Note ‘Sehr gut’

### Publications in peer-reviewed journals

1. M. D. J. Cole, S. L. Newton, S. C. Cowley, N. F. Loureiro, D. Dickinson, C. Roach and J. W. Connor  
*Electromagnetic effects in the stabilization of turbulence by sheared flow*  
Plasma Physics and Controlled Fusion **56**, 015007 (2013)
2. M. D. J. Cole, A. Mishchenko, A. Könies, R. Kleiber and M. Borchardt  
*Fluid electron, gyrokinetic ion simulations of linear internal kink and energetic particle modes*  
Physics of Plasmas **21**, 072123 (2014)
3. A. Mishchenko, M. Cole, R. Kleiber and A. Könies  
*New variables for gyrokinetic electromagnetic simulations*  
Physics of Plasmas **21**, 052113 (2014)
4. A. Mishchenko, R. Kleiber, A. Könies and M. Cole  
*Pullback transformation in gyrokinetic electromagnetic simulations*  
Physics of Plasmas **21**, 092110 (2014)
5. M. D. J. Cole and A. Mishchenko and A. Könies and R. Hatzky and R. Kleiber  
*A hierarchy of electromagnetic gyrokinetic and fluid hybrid models for the simulation of global modes*  
Plasma Physics and Controlled Fusion **57**, 054013 (2015)
6. A. Mishchenko, M. Borchardt, M. Cole, R. Hatzky, T. Fehér, R. Kleiber, A. Könies and A. Zocco  
*Global linear gyrokinetic particle-in-cell simulations including electromagnetic effects in shaped plasmas*  
Nuclear Fusion **55**, 053006 (2015)
7. M. D. J. Cole, A. Biancalani, M. Borchardt, A. Bottino, R. Kleiber, A. Könies, A. Mishchenko  
*Toroidal Alfvén Eigenmodes with nonlinear gyrokinetic and fluid hybrid models*  
Physics of Plasmas, *submitted*

## Oral and poster presentations

1. M. D. J. Cole, A. Mishchenko and A. Könies  
*Electron fluid simulations of Alfvén eigenmodes (oral)*  
IPP Theory Meeting, Damerow, 2013
2. M. D. J. Cole, A. Mishchenko and A. Könies  
*Simulations of Alfvén eigenmodes in tokamaks and stellarators (oral)*  
12th ITPA Energetic Particle Physics TG Meeting, Madrid, 2014
3. M. D. J. Cole, A. Mishchenko and A. Könies  
*Simulations of Alfvén eigenmodes in tokamaks and stellarators (invited)*  
2014 Joint Varenna-Lausanne International Workshop on the Theory of Fusion Plasmas, Varenna, 2014
4. M. D. J. Cole, A. Mishchenko and A. Könies  
*Simulations of Alfvén eigenmodes in tokamaks and stellarators (oral)*  
IPP Theory Meeting, Ringberg, 2014
5. M. D. J. Cole, A. Mishchenko and A. Könies  
*Hybrid simulations of global modes in magnetic fusion devices (oral)*  
DPG Frühjahrstagung, Bochum, 2015
6. M. D. J. Cole, A. Mishchenko, A. Könies, A. Biancalani, M. Borchardt, R. Hatzky, R. Kleiber and P. Lauber  
*Progress in non-linear gyrokinetic simulations of global modes in tokamaks and stellarators (invited)*  
14th IAEA Technical Meeting on Energetic Particles in Magnetic Confinement Systems, Vienna, 2015
7. M. D. J. Cole, A. Könies, A. Mishchenko, M. Borchardt, R. Hatzky and R. Kleiber  
*Progress in non-linear gyrokinetic simulations of global modes in tokamaks and stellarators (poster)*  
20th International Stellarator-Heliotron Workshop, Greifswald, 2015
8. M. D. J. Cole, A. Könies, A. Mishchenko, M. Borchardt, R. Hatzky and R. Kleiber  
*Progress in non-linear gyrokinetic simulations of global modes in tokamaks and stellarators (oral)*  
IPP Theory Meeting, Plau am See, 2015



# Acknowledgements

Six months before I arrived in the quaint old Baltic city of Greifswald, I never imagined I might move to Germany. Since then I have witnessed the start-up of the worlds first optimised stellarator, learnt a new language, worked on two continents, and found time to write a doctoral thesis. For all that I graciously acknowledge Per Helander, who started it all by a chance encounter. Per has always been enthusiastic to help me with any aspect of physics, and his epieikeic presence never fails to improve any gathering.

My greatest appreciation goes to my direct supervisor, Alexey Mishchenko, who has always made himself available to assist me in my work. Without his attention, patience, and expertise this work would not have been possible. I would also like to thank him for sharing with me his perspective on the world. We see many things very differently, but he has always treated these differences with good grace. I dont know if he has learnt much from me, but I have certainly learnt a lot from him.

It is also a pleasure to thank all the other colleagues at IPP Greifswald who've helped me with my work, foremost among them Ralf Kleiber, Axel Könies, Matthias Borchardt, Henry Leyh, Jutta Gauger, and Andrea Kleiber. I would like to thank Axel Könies especially for the way he has welcomed me to our common endeavour investigating fast particle physics at Greifswald, for his tremendous intellectual honesty, and for sharing his deep knowledge and evident love of the German language with me. I appreciate the patience of everyone in tolerating my own attempts to speak German.

At IPP Garching I would like to thank Philipp Lauber, Alessandro Biancalani, and Xin Wang, and at the Australian National University I would like to thank Matthew Hole, Boyd Blackwell, and George Bowden, for being so welcoming to me and facilitating enjoyable and productive visits.

Of course life is not just work, and I do not have space here to acknowledge all of those who made my time here in Greifswald so enjoyable. They know who they are. Finally, I thank my family for their constant love and support.